3-23-2018

Radar Signal Processing for Interference Mitigation

Zhe Geng
Florida International University, zgeng001@fiu.edu

DOI: 10.25148/etd.FIDC006569

FLORIDA INTERNATIONAL UNIVERSITY

Miami, Florida

RADAR SIGNAL PROCESSING FOR INTERFERENCE MITIGATION

A dissertation submitted in partial fulfillment of

the requirements for the degree of

DOCTOR OF PHILOSOPHY

in

ELECTRICAL ENGINEERING

by

Zhe Geng

2018

To: Dean John L. Volakis
College of Engineering and Computing

This dissertation, written by Zhe Geng, and entitled Radar Signal Processing for Interference Mitigation, having been approved in respect to style and intellectual content, is referred to you for judgment.

We have read this dissertation and recommend that it be approved.

_____
Malek Adjouadi

_____
Jean Andrian

_____
Ismail Guvenc

_____
Deng Pan

_____
Hai Deng, Major Professor

Date of Defense: March 23, 2018

The dissertation of Zhe Geng is approved.

_____
Dean John L. Volakis
College of Engineering and Computing

_____
Andrés G. Gil
Vice President for Research and Economic Development
and Dean of the University Graduate School

Florida International University, 2018

ACKNOWLEDGMENTS

I would like to thank my advisor, Dr. Hai Deng, for his expert advice and guidance for the completion of this dissertation. I would also like to thank my committee members: Dr. Malek Adjouadi, Dr. Jean Andrian, Dr. Ismail Guvenc and Dr. Deng Pan, for their advice and support.

Finally, I gratefully acknowledge the financial support provided by the FIU Presidential Fellowship, the National Science Foundation under Award AST-1443909, and the Air Force Research Laboratory under Contract FA8650-12-D-1376.

ABSTRACT OF THE DISSERTATION

RADAR SIGNAL PROCESSING FOR INTERFERENCE MITIGATION

by

Zhe Geng

Florida International University, 2018

Miami, Florida

Professor Hai Deng, Major Professor

It is necessary for radars to suppress interferences to near the noise level to achieve the best performance in target detection and measurements. In this dissertation work, innovative signal processing approaches are proposed to effectively mitigate two of the most common types of interferences: jammers and clutter. Two types of radar systems are considered for developing new signal processing algorithms: phased-array radar and multiple-input multiple-output (MIMO) radar.

For phased-array radar, an innovative target-clutter feature-based recognition approach termed as Beam-Doppler Image Feature Recognition (BDIFR) is proposed to detect moving targets in inhomogeneous clutter. Moreover, a new ground moving target detection algorithm is proposed for airborne radar. The essence of this algorithm is to compensate for the ground clutter Doppler shift caused by the moving platform and then to cancel the Doppler-compensated clutter using MTI filters that are commonly used in ground-based radar systems. Without the need of clutter estimation, the new algorithms outperform the conventional Space-Time Adaptive Processing (STAP) algorithm in ground moving target detection in inhomogeneous clutter.

For MIMO radar, a time-efficient reduced-dimensional clutter suppression algorithm termed as Reduced-dimension Space-time Adaptive Processing (RSTAP) is proposed to minimize the number of the training samples required for clutter estimation. To deal with highly heterogeneous clutter more effectively, we also proposed a robust deterministic STAP algorithm operating on snapshot-to-snapshot basis. For cancelling jammers in the radar mainlobe direction, an innovative jamming elimination approach is proposed based on coherent MIMO radar adaptive beamforming. When combined with mutual information (MI) based cognitive radar transmit waveform design, this new approach can be used to enable spectrum sharing effectively between radar and wireless communication systems.

The proposed interference mitigation approaches are validated by carrying out simulations for typical radar operation scenarios. The advantages of the proposed interference mitigation methods over the existing signal processing techniques are demonstrated both analytically and empirically.

TABLE OF CONTENTS

LIST OF TABLES

TABLE PAGE

LIST OF FIGURES

FIGURE PAGE

ABBREVIATIONS AND ACRONYMS

1st-RSTAP	First-order Reduced-dimension Space-time Adaptive Processing
2nd-RSTAP	Second-order Reduced-dimension Space-time Adaptive Processing
3GPP	3rd Generation Partnership Project
ARB	Actual Receive Beam
AM	Amplitude Modulation
BDIFR	Beam-Doppler Image Feature Recognition
BS	Base Station
CMT	Covariance Matrix Tapers
CNR	Clutter-to-Noise Ratio
CPI	Coherent Processing Interval
CW	Continuous Wave
DFRC	Dual-Function Radar Communications
DFT	Discrete Fourier Transform
DOA	Direction of Arrival
DOF	Degrees of Freedoms
DARPA	Defense Advanced Research Projects Agency
DPCA	Displaced Phase Center Antenna
D-STAP	Deterministic Space-time Adaptive Processing
ECM	Electronic Counter-Measurements
ESA	Enhanced Simulated Annealing

ESM	Electronic Support Measurement
FA-STAP	Fully Adaptive Space-time Adaptive Processing
GLRT	Generalized Likelihood Ratio Test
ICIC	Inter-Cell Interference Coordination
ICM	Intrinsic Clutter Motion
IF	Improve Factor
IFSTP	Image-feature-based Space-time Processing
IID	Independent and Identically Distributed
INR	Interference-to-Noise Ratio
JNR	Jamming-to-noise Ratio
JRC	Joint Radar-Communication
LOS	Line-of-Sight
LPI	Low Probability of Intercept
LTE	Long-Term Evolution
MDB-RG	Minimum-distance-based Region Growing
MDV	Minimum Detectable Velocity
MLE	Maximum Likelihood Estimate
MI	Mutual Information
MIMO	Multiple-input Multiple-output
MTD	Moving Target Detection
MTI	Moving Target Indication
MV	Minimum Variance

MVDR	Minimum Variance Distortionless Response
OFDM	Orthogonal Frequency Division Multiplexing
PDF	Probability Density Function
PM	Phase Modulation
PRF	Pulse Repetition Frequency
PRI	Pulse Repetition Interval
PSK	Phase-Shift Keying
PST	Power-selected training
R-D-STAP	Robust Deterministic Space-time Adaptive Processing
REM	Radio Environmental Map
RF	Radio Frequency
RG	Region Growing
RSTAP	Reduced-dimension Space-time Adaptive Processing
SCR	Signal to Clutter Ratio
SINR	Signal to Interference plus Noise Ratio
SLB	Sidelobe Blanking
SLC	Sidelobe Canceller
SNR	Signal to Noise Ratio
SSPARC	Shared Spectrum Access for Radar and Communications
S-STAP	Statistic Space-time Adaptive Processing
SMI	Sample Matrix Inverse
STAP	Space-time Adaptive Processing

TACCAR	Time Average Clutter Coherent Airborne Radar
T-D-STAP	Traditional Deterministic Space-time Adaptive Processing
ULA	Uniform Linear Arrays
USDF	Usable Doppler Space Fraction
VAB	Virtual Antenna Beam
WSS	Wide-Sense Stationary

1. INTRODUCTION

In realistic scenarios, radar systems must be capable of dealing with more than receiver noise when detecting targets. In this dissertation, two of the most common types of interferences are considered: clutter (echoes from the natural environment) and jamming (interfering signals directed at the radar system from either intentional or unintentional jammers).

1.1. Background - Interference Suppression in Radar Systems

1.1.1. Introduction to radar systems

Radar systems could be classified into two types: continuous wave radar (CW) and pulse radar, with pulse radar used in most modern radar systems [1]. A pulse radar transmits and receives a train of modulated pulses. Radar processing, which can occur over several consecutive pulses, lies within the coherent processing interval (CPI). The principal subsystems of a pulse radar include the waveform generator, the transmitter, the antennas and the receiver [2]. Among these subsystems, the radar antennas play a very important role in determining the sensitivity and the angular resolution of radar. Specifically, in this dissertation, two types of radar antennas are considered: phased-array antenna and MIMO antenna.

- Radar with Phased-array Antenna

Unlike the reflector antenna that has a single radiator, phased-array antenna have hundreds of individual radiation elements. Since the magnitude and the phase of the voltage fed to each antenna element can be individually controlled, wavefronts with any

desired shape could be generated with basically no delay [3]. It allows the phased-array antenna to greatly outperform the conventional reflector antenna, which needs to take the time to move mechanically. A radar system that employs phased-array antenna is termed as phased-array radar.

- Radar with MIMO Antenna

MIMO radar employs multiple antennas and different signals are transmitted simultaneously from each antenna. There are basically two types of MIMO radar: statistical MIMO radar with widely separated antennas [4-6] and coherent MIMO radar with collocated antennas [7, 8]. For coherent MIMO radar, orthogonal waveforms are transmitted and received from each of its collocated antenna elements, and the signal phase relationship between the received signals are accurately known, which makes it possible for coherent signal processing spatially [8, 9]. Compared to the traditional phased-array radar, the coherent MIMO radar has a great number of advantages, such as improved parameter identifiability and enhanced flexibility for transmit beampattern design [10].

1.1.2. Clutter and jamming interference

In radar the term clutter refers to the unwanted echoes received by the radar receivers from surface scatterers (e.g. the earth's surface) or volume scatterers (e.g. rain) in the natural environment. For an airborne ground surveillance radar trying to detect a moving target (e.g. a vehicle) on the ground, the clutter echoes from the surrounding terrain are the most significant interferences. The received clutter power is determined by the radar antenna gain, radar transmitting power, the reflectivity of each scatterer in the

resolution cell, and the range from the radar to the terrain [11]. The differences between clutter echoes and target echoes in probability density functions (PDFs), temporal/spatial correlation properties and Doppler characteristics are often exploited by researchers to separate clutter and target signals [12, 13]. Since the ground clutter is composed of many scatters per resolution cell, it has to be modeled properly before any radar signal processing could be carried out.

Jamming is another type of interference which threatens successful detection of targets. It refers to radio frequency (RF) signals originating from sources transmitting at the same frequency with the radar system and thereby masking the target of interest. The most basic form of jamming is noise jamming [14, 15]. It is capable of interfering with the operation of a radar by saturating its receiver with noise and could be either intentional (e.g. hostile electronic countermeasurements) or accidental (e.g. interferences from commercial wireless communication system). A more advanced form of jamming is to use waveforms designed to mimic target echoes with a delay to indicate incorrect range [16, 17]. The power of the one-way jamming signals received by a radar system is often much stronger than the two-way radar echo signal, hence it is capable of completely masking the target of interest along the line-of-sight from the jammer to the radar [18].

1.1.3. Current radar interference mitigation technologies

Statistical space-time adaptive processing (STAP) is the most popular technique in eliminating the clutter signals and jamming signals simultaneously for moving target detection with the long-range surveillance airborne radar system [19, 20]. However, statistical STAP requires the second order statistic information, i.e., covariance matrix, of

the clutters be known *a priori* or be accurately estimated from the training data collected from the secondary range bins that are adjacent to the primary range bin, i.e. target detection bin, under the assumption that the clutters in the primary and secondary bins are statistically independent and identically distributed (IID) [21]. The amount of secondary data samples needed for accurate estimation of the clutter covariance matrix is determined by its dimension via the RMB rule, which was described by Reed, Mallett, and Brennan in [22]. Specifically, according to the RMB rule, the expected value of the adaptive SINR loss is approximately 3 dB when the number of IID samples is roughly twice the product of the number antenna elements and the number of pulses per CPI [23]. Since clutter is inhomogeneous in real life, it is often difficult to obtain the necessary amount of IID secondary data, which leads to the mismatch between the actual and the estimated clutter covariance matrix and significant STAP performance degradation.

By far, common techniques coping with inhomogeneous clutter include data-dependent training techniques, minimal sample support STAP (reduced dimension STAP) and covariance matrix tapers (CMT) [24]. Power-selected training (PST) and map-based training selection are two examples of data-dependent training techniques [24]. PST uses adaptive procedures to choose stronger clutter samples for clutter covariance matrix estimation in order to yield deeper clutter nulls [25]. As in the map-based training selection method, mapping information is used to identify optimum training regions [26]. The essence of the minimal sample support STAP (reduced dimension STAP) method is to transform the space-time data into low-dimensional subspace, hence minimizing the required training data [27]. CMT was proposed in [28] and [29] to cope with CNR-induced spectral mismatch. The essence of CMT is to apply a

complex taper to the space time data to tailor the adaptive notch width and create a desirable adaptive filter response for specific clutter characteristics. The essence of techniques above is to provide accurate clutter estimation in inhomogeneous clutter.

Another line of research is to avoid the clutter estimation completely by using non-adaptive clutter suppression approaches. Time Average Clutter Coherent Airborne Radar (TACCAR) is one of the airborne radar systems using a non-adaptive clutter suppression approach to remove ground clutter through direct moving target indication (MTI) cancellation processing by tracking clutter Doppler frequency and then compensating out clutter Doppler frequency [30]. The clutter cancellation performance of TACCAR is limited by the fact that clutter Doppler frequencies are extended in a certain range and cannot be compensated simultaneously through a single Doppler-tracking loop [31, 32]. Another non-adaptive clutter processing approach is using displaced phase center antenna (DPCA) to emulate surface-based MTI radar clutter processing [33]. However, the DPCA method requires the exact relationship between the radar platform velocity and antenna element spacing to be known, which may not be practical in typical radar detection scenarios [34]. The deterministic STAP (D-STAP) approach presented in [35] operates on a snapshot-by-snapshot basis to determine the adaptive weights and can be readily implemented in real time. The major problem with classic D-STAP is that when a mismatch between the nominal and the actual target direction-of-arrival (DOA) exists, the performance of the classic deterministic STAP approach would be compromised.

A lot of spatial signal processing techniques have been proposed to eliminate jamming signals received through the antenna sidelobe, such as Sidelobe Blanking (SLB)

system [36] and Sidelobe Canceller (SLC) system [37]. In an SLB system, the signals entering the sidelobes are distinguished from the signals entering the main beam by using two parallel channels (i.e. the main channel and the auxiliary channel), thereby the former could be suppressed [36]. In an SLC system, the DOA and the powers of the jamming signals are estimated adaptively, so that nulls could be formed in the radar receiving antenna beampattern in the jamming directions [37]. However, both SLB and SLC are not applicable for the cases where the jamming interference enters the radar receiver through the antenna mainlobe.

1.2. Problem Statement

Radar systems must be capable of dealing with interferences other than receiver noise in order to detect the target successfully. For airborne radar trying to detect a ground moving target, the clutter echoes from the surrounding ground are the most significant interferences. However, current clutter suppression technologies either suffer from dramatic performance degradation in inhomogeneous clutter due to a lack of enough IID training samples or have high computational complexity. Jamming is another type of interference that is capable of completely masking the target of interest along the line-of-sight from the jammer to the radar. Unfortunately, current jamming elimination technologies are not applicable for the cases where the jamming interference enters radar receiver through the antenna mainlobe.

Phased-array radar has been used for various radar missions over the past decades. In recent years, many studies have been focused on applying MIMO techniques to radar systems to enhance radar performances. It has been demonstrated in many

literatures that, compared with conventional phased-array radars, coherent MIMO radar provides higher angle/Doppler resolution, lower probability of intercept (LPI) and better interference suppression performance.

In this dissertation, innovative clutter suppression approaches are proposed for both phased-array radar and MIMO radar to minimize the training samples required for accurate clutter estimation, thereby improving the clutter suppression and moving target detection performance for airborne radar in heterogeneous clutter. To cope with jamming in mainlobe direction, an innovative jamming elimination approach is proposed based on coherent MIMO radar adaptive beamforming.

1.3. Contribution of the Dissertation

An image feature-based target-interference recognition approach termed as BDIFR is proposed for phased array radar to cope with inhomogeneous clutter and jamming signals. Since the moving targets and the interferences are well separated in beam-Doppler domain, image processing techniques are used in BDIFR to discriminate target from interference (clutter and jamming). Meanwhile, an innovative moving target detection algorithm based on Doppler compensation and digital beamforming is also proposed. The moving platform effects on the Doppler spectrum are compensated using a Doppler compensation matrix, and then the Doppler-compensated clutter is eliminated using direct cancellation processing in time domain. Since accurate clutter estimation is unnecessary, both of the algorithms outperform the conventional STAP algorithm in ground moving target detection in inhomogeneous clutter.

Moreover, innovative STAP-based clutter suppression approaches are proposed for airborne radar ground moving target detections in inhomogeneous clutter. A time-efficient reduced-dimensional clutter suppression algorithm termed as RSTAP is proposed for MIMO radar to minimize the IID training samples required for accurate clutter estimation. To deal with highly inhomogeneous clutter, a robust deterministic STAP algorithm operating on snapshot-to-snapshot basis is also proposed, which could be applied to both phased-array radar and MIMO radar. The performance of the proposed RSTAP filter and the robust D-STAP filter for phased-array radar and MIMO radar structure is evaluated and compared.

To cope with jamming in mainlobe direction, an innovative jamming elimination approach is proposed based on coherent MIMO radar adaptive beamforming. Since the waveform transmitted from each antenna element of the MIMO antenna array is designed to be orthogonal to each other, a coherent wave transmitted by an antenna element could be identified and extracted from the received echo signal through a matched filter correlated only to that waveform. After that, by applying a space-domain digital filter at the matched filter outputs, interference signals received at both antenna mainlobe and sidelobes from wireless systems will be canceled while target signals will be enhanced.

1.4. Dissertation Organization

In Chapter 2, an innovative ground moving target detection method termed as beam-Doppler image feature recognition (BDIFR) is introduced based on the distinctive moving target and interference (clutter and jamming) features in the beam-Doppler domain. In Section 2.1, the signal models for airborne phased-array radar are presented.

In Section 2.2, the transformation of radar echo data from space-time domain to Beam-Doppler domain using the 2D DFT and the minimum variance (MV) method is discussed. In Section 2.3, the minimum-distance based region growing (MDB-RG) algorithm is developed for radar target and interference feature extraction in beam-Doppler domain. In Section 2.4, the target detection based on the feature metric is introduced. Simulation results are given in Section 2.5 by assuming various airborne radar operation scenarios. In Section 2.6, the performance of the proposed BDIFR approach is evaluated. Finally, a brief summary of the chapter is provided in Section 2.7.

In Chapter 3, an efficient ground moving target detection approach is introduced for airborne radar using clutter Doppler compensation and digital beamforming. In Section 3.1, Doppler compensation for the moving platform effects on the Doppler Spectrum is discussed. In Section 3.2, the pulse canceller is applied to the Doppler-compensated beam-Doppler domain radar data to eliminate the clutter signals. In Section 3.3, the performance of the proposed clutter suppression approach is evaluated based on the MTI Improvement Factor (IF), Minimum Detectable Velocity (MDV) and Usable Doppler Space Fraction (UDSF). In Section 3.4, simulation results are provided. A summary of Chapter 3 is given in Section 3.5.

In Chapter 4, STAP-based clutter suppression approaches are proposed for airborne MIMO radar to deal with heterogeneous clutter. In Section 4.1, signal models for airborne MIMO radar are presented. In Section 4.2, fully adaptive STAP (FA-STAP) is discussed. In Section 4.3 and Section 4.4, the RSTAP filter and D-STAP filter are proposed. Meanwhile, the performance of the proposed RSTAP filter and the robust D-

STAP filter for phased-array radar and MIMO radar structure is evaluated and compared. A brief summary of the chapter is given in Section 4.5.

In Chapter 5, an innovative interference mitigation approach which allows radar systems to effectively eliminate the jamming interference from any direction is proposed. The process of MI-based cognitive radar waveform design is detailed in Section 5.1. The interference mitigation processing method based on MIMO radar beamforming is presented in Section 5.2. The required interference mitigation for radar and wireless system to operate normally in the presence of each other is derived in Section 5.3. Simulations are carried out by assuming a general spectrum sharing scenario between S-band MIMO radar and wireless systems, and the simulation results are given in Section 5.4. Finally, a summary of Chapter 5 is provided in Section 5.5.

In Chapter 6, the main points of the research are summarized, the limitations of the research are discussed, and the direction for future research is implicated.

2. RADAR INTERFERENCE SUPPRESSION WITH BEAM-DOPPLER IMAGE FEATURE RECOGNITION (BDIFR)

Since the clutter is inhomogeneous in real life, it is often difficult to obtain the necessary amount of IID secondary data, which leads to the inaccurate estimation of the clutter covariance matrix and significantly performance degradation of conventional clutter suppression techniques (e.g. STAP). For avoidance of accurate clutter estimation in inhomogeneous clutter, an innovative ground moving target detection method based on the distinctive moving target and interference (clutter and jamming) features in the beam-

Doppler domain is proposed in this chapter. This image-feature based target-interference recognition approach is termed as beam-Doppler image feature recognition (BDIFR).

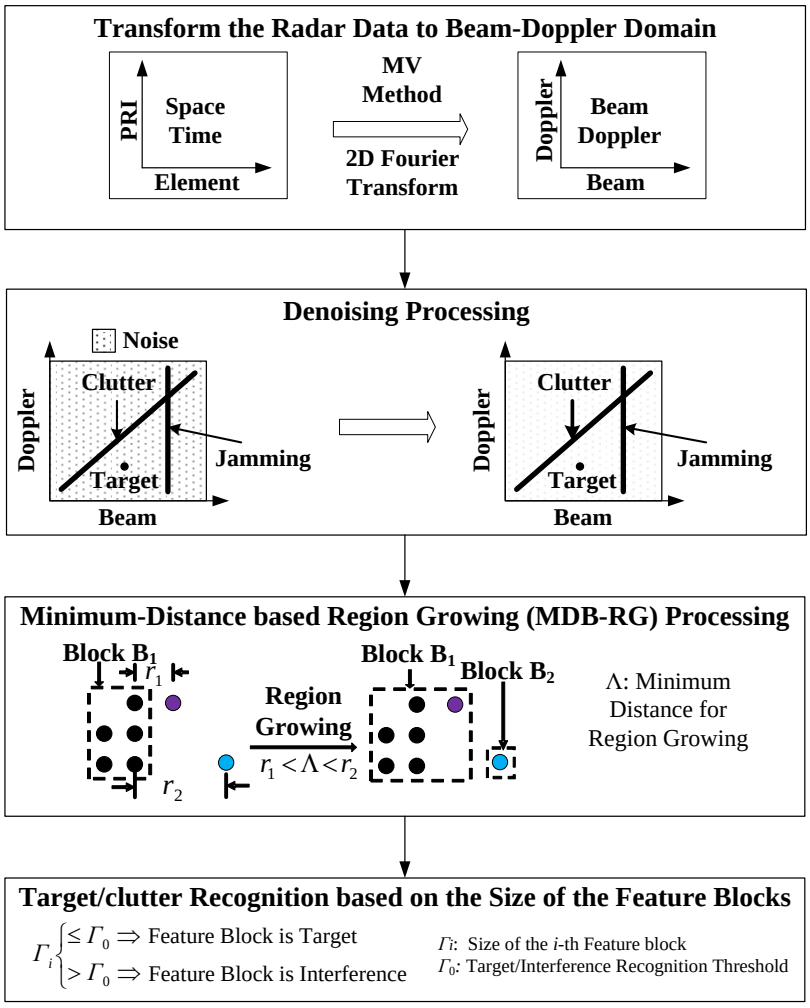

Figure 2.1 Procedures of the BDIFR method

The procedures of the BDIFR method are illustrated in Figure 2.1. Firstly, the received radar echo data in space-time domain are transformed from the space-time domain to the beam-Doppler domain via 2D-DFT or minimum variance (MV) method depending on the number of space-time snapshots available. After that, the noise signals on the beam-Doppler image are removed using denoising processing. Following the denoising processing, the target and interference features become separable, and the

minimum-distance based region growing (MDB-RG) algorithm is used to generate feature blocks from the beam-Doppler image. Since the target feature blocks are in pointed shape while the interference feature blocks are in extended shape, the target detection is then carried out by comparing the size of the feature blocks with the predetermined threshold Γ_0.

The rest of the chapter is organized as following. In Section 2.1, signal models for airborne phased-array radar is presented. In Section 2.2, the transformation of radar echo data from space-time domain to Beam-Doppler domain using the 2D-DFT or MV method is discussed. In Section 2.3, MDB-RG is developed specifically for radar target and clutter feature extraction in beam-Doppler domain. In Section 2.4, the target detection based on the feature metric is introduced. In Section 2.5, simulation results are given by assuming various airborne radar operation scenarios. In Section 2.6, the performance of the proposed BDIFR approach is evaluated. A brief summary of Chapter 2 is given in Section 2.7.

2.1. Signal Models for Airborne Phased-array Radar

An airborne radar with uniform linear antenna array of N antenna elements is considered for clutter mitigation in this chapter. The airborne radar platform is depicted in Figure 2.2, where R_r and R_0 are the range from radar to the r-th clutter ring and the range from radar to the target, respectively; ϕ_0 and θ_0 are the elevation angle and the azimuth angle of the target, respectively; ϕ_r and $\theta_{r,k}$ are the elevation angle and the azimuth angle of the k-th clutter patch on the r-th range ring, respectively. To simplify the problem, it is assumed that the velocity of the airborne radar platform is aligned with

y-axis, i.e. $\mathbf{v}_a = [0\ v_a\ 0]^T$. It is further assumed that there are M coherent pulses in one CPI for the radar operation.

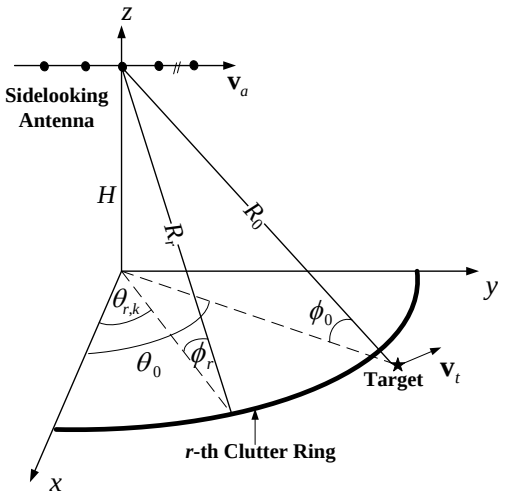

Figure 2.2 Airborne radar platform geometry.

2.1.1. Components of a radar signal

The spatial-temporal samples of radar echoes from the antenna array during a CPI are arranged into the following $NM \times 1$ vector

$$\mathbf{x} = [x(0,0)\ \ x(0,1)\cdots x(0,N)\ \ x(1,0)\cdots x(m,n)\ \cdots\ x(M,N)]^T \tag{2.1}$$

where $x(m,n)$ is the radar echo data sample at element n for pulse m with $0 \le n \le N-1$ and $0 \le m \le M-1$. Furthermore, the component vectors of target, thermal noise, clutter and jamming are represented by $\mathbf{x}_t, \mathbf{x}_n, \mathbf{x}_c$ and $\mathbf{x}_j$, respectively, and are expressed as

$$\mathbf{x}_t = [t(0,0)\ \ t(0,1)\cdots t(0,N)\ \ t(1,0)\cdots t(m,n)\ \cdots\ t(M-1,N-1)]^T \tag{2.2}$$

$$\mathbf{x}_n = [n(0,0)\ \ n(0,1)\cdots n(0,N)\ \ n(1,0)\cdots n(m,n)\ \cdots\ n(M-1,N-1)]^T \tag{2.3}$$

$$\mathbf{x}_c = [c(0,0)\ \ c(0,1)\cdots c(0,N)\ \ c(1,0)\cdots c(m,n)\ \cdots\ c(M-1,N-1)]^T \tag{2.4}$$

$$\mathbf{x}_j = [j(0,0)\ \ j(0,1)\cdots j(0,N)\ \ j(1,0)\cdots j(m,n)\ \cdots\ j(M-1,N-1)]^T \tag{2.5}$$

where $t(m,n), n(m,n), c(m,n)$ and $j(m,n)$ are the *k*-th element of $\mathbf{x}_t, \mathbf{x}_n, \mathbf{x}_c$ and $\mathbf{x}_j$ with $1 \le k \le NM$, respectively. The relationship between (*m*, *n*) and *k* is given by

$$m = \left\lfloor \frac{k-1}{N} \right\rfloor \tag{2.6}$$

$$n = k - mN - 1 \tag{2.7}$$

where $\lfloor \ \rfloor$ denotes the floor function.

The radar echo vector in (2.1) may contain target, noise, clutter and jamming, i.e., H_1 hypothesis; or clutter and noise only, i.e. H_0 hypothesis. It follows that

$$\mathbf{x} = \begin{cases} \mathbf{x}_n + \mathbf{x}_c + \mathbf{x}_j & : H_0 \\ \mathbf{x}_n + \mathbf{x}_c + \mathbf{x}_j + \mathbf{x}_t & : H_1 \end{cases} \tag{2.8}$$

To represent clutter and target signals in the beam-Doppler domain, the priority task is to find the covariance matrix of the received radar signals. The covariance matrix of radar data vector **x** is given by

$$\mathbf{R} = E[\mathbf{x}\mathbf{x}^H] \tag{2.9}$$

where the superscript *H* denotes the conjugate transpose. Assume that $\mathbf{x}_t, \mathbf{x}_n, \mathbf{x}_c$ and $\mathbf{x}_j$ are statistically mutually independent, **R** is further written as

$$\mathbf{R} = \begin{cases} \mathbf{R}_n + \mathbf{R}_c + \mathbf{R}_j & : H_0 \\ \mathbf{R}_n + \mathbf{R}_c + \mathbf{R}_j + \mathbf{R}_t & : H_1 \end{cases} \tag{2.10}$$

where $\mathbf{R}_t$, $\mathbf{R}_n$, $\mathbf{R}_c$ and $\mathbf{R}_j$ are the covariance matrices of the target, noise, clutter, jamming and component vectors $\mathbf{x}_t, \mathbf{x}_n, \mathbf{x}_c$ and $\mathbf{x}_j$, respectively.

2.1.2. Point target model

When far-field point target model is assumed, the covariance matrix of the target signal, $\mathbf{R}_t$, is given by

$$\mathbf{R}_t = E\left\{\mathbf{x}_t \mathbf{x}_t^H\right\} = \sigma^2 \xi_t \mathbf{v}_t(\vartheta_t, \varpi_t)\mathbf{v}_t(\vartheta_t, \varpi_t)^H \tag{2.11}$$

where ξ_t is the single-pulse signal-to-noise ratio (SNR) for a single receiving element of the antenna. $\mathbf{v}_t(\varpi_t, \vartheta_t)$ in (2.11) is the target spatio-temporal steering vector, and is given by

$$\mathbf{v}_t(\vartheta_t, \varpi_t) = \mathbf{b}_t(\varpi_t) \otimes \mathbf{a}_t(\vartheta_t). \tag{2.12}$$

$\mathbf{a}_t(\vartheta_t)$ in (2.12) denotes the target spatial steering vector and is represented as

$$\mathbf{a}_t(\vartheta_t) = \begin{bmatrix} 1 & e^{j2\pi\vartheta_t} & \cdots & e^{j(N-1)2\pi\vartheta_t} \end{bmatrix}^T \tag{2.13}$$

where ϑ_t is the target spatial frequency. ϑ_t could be further written as

$$\vartheta_t = \frac{d_0}{\lambda} \sin\theta_0 \cos\phi_0 \tag{2.14}$$

where d_0 is antenna array element spacing, λ is the radar wavelength , ϕ_0 and θ_0 denote target elevation and azimuth angles, respectively. $\mathbf{b}_t(\varpi_t)$ in (2.12) denotes the target temporal steering vector, and is expressed as

$$\mathbf{b}_t(\varpi_t) = \begin{bmatrix} 1 & e^{j2\pi\varpi_t} & \cdots e^{j(M-1)2\pi\varpi_t} \end{bmatrix}^T \tag{2.15}$$

where ϖ_t is the target normalized Doppler frequency. When target Doppler frequency is f_d , ϖ_t is given by

$$\varpi_t = \frac{f_d}{f_r}. \tag{2.16}$$

2.1.3. Noise

Assume that the noise samples are uncorrelated spatially and temporally, the following relationships are obtained

$$E\left\{x_{n_1,m}x^*_{n_2,m}\right\}=\sigma^2\delta_{n_1-n_2} \tag{2.17}$$

$$E\left\{x_{n,m_1}x^*_{n,m_2}\right\}=\sigma^2\delta_{m_1-m_2} \tag{2.18}$$

where δ_Δ is given by

$$\delta_\Delta=\begin{cases}1\,,\ \Delta=0\\ 0\,,\ \Delta\neq 0\end{cases} \tag{2.19}$$

Hence the noise covariance matrix, $\mathbf{R}_n$, is given by

$$\mathbf{R}_n=E\left\{\mathbf{x}_n\mathbf{x}_n^H\right\}=\sigma^2\mathbf{I}_{NM} \tag{2.20}$$

where σ^2 is the variance of the white noise and $\mathbf{I}_{NM}$ is an $NM\times NM$ identity matrix.

2.1.4. Clutter

The clutter covariance matrix $\mathbf{R}_c$ can be estimated from the following equation

$$\mathbf{R}_c=E\{\mathbf{x}_c\mathbf{x}_c^H\}=\sum_{k=1}^{N_c}E\{|\alpha_k|^2\}\mathbf{v}(\vartheta_k,\varpi_k)\mathbf{v}(\vartheta_k,\varpi_k)^H \tag{2.21}$$

where N_c is the number of independent ground clutter patches that are evenly distributed in azimuth on the range ring, and α_k is the random complex amplitude of the clutter from the *k*-th clutter patch. $\mathbf{v}(\vartheta_k,\varpi_k)$ in (2.21) denotes the spatio-temporal steering vector pointing in the direction of the *k*-th clutter patch and is given by

$$\mathbf{v}(\vartheta_k,\varpi_k)=\mathbf{b}(\varpi_k)\otimes\mathbf{a}(\vartheta_k) \tag{2.22}$$

where $\otimes$ denotes Kronecker product, $\mathbf{a}(\vartheta_k)$ and $\mathbf{b}(\varpi_k)$ are the spatial and temporal steering vectors of *k*-th clutter patch, respectively. $\mathbf{a}(\vartheta_k)$ is given by

$$\mathbf{a}(\vartheta_k) = \left[1 \; e^{j2\pi\vartheta_k} \; \cdots \; e^{j(N-1)2\pi\vartheta_k}\right]^T \tag{2.23}$$

where ϑ_k is the spatial frequency of the clutter patch and is calculated as

$$\vartheta_k = \frac{d_0}{\lambda} \sin\theta_{r,k} \cos\phi_r \,. \tag{2.24}$$

ϕ_r and $\theta_{r,k}$ are the elevation angle and the azimuth angle of the *k*-th clutter patch on the range ring, respectively (refer to Figure 2.2). $\mathbf{b}(\varpi_k)$ in (2.22) is expressed as

$$\mathbf{b}(\varpi_k) = \left[1 \; e^{j2\pi\varpi_k} \cdots e^{j(M-1)2\pi\varpi_k}\right]^T \tag{2.25}$$

where ϖ_k is the normalized Doppler frequency of the clutter patch. Assume that the Doppler frequency of *k*-th clutter patch is $f_{d,k}$ and the pulse repetition frequency (PRF) of the radar waveform is f_r, ϖ_k is then given by

$$\varpi_k = \frac{f_{d,k}}{f_r} \,. \tag{2.26}$$

Assume that the clutter-to-noise-ratio (CNR) per element per pulse of the *k*-th clutter patch is ξ_k, the clutter covariance matrix $\mathbf{R}_c$ given in (2.21) could be further expressed as

$$\mathbf{R}_c = \sigma^2 \sum_{k=1}^{N_c} \xi_k \left[\mathbf{b}(\varpi_k)\mathbf{b}^H(\varpi_k)\right] \otimes \left[\mathbf{a}(\vartheta_k)\mathbf{a}^H(\vartheta_k)\right]. \tag{2.27}$$

2.1.5. Jamming

Assume that the jammer power spectral density received by one array element from a single jammer located at azimuth angle ϕ_j and elevation angle θ_j is J_0. The received jamming-to-noise ratio (JNR) per element is then given by

$$\xi_j = J_0 / N_0 \tag{2.28}$$

where N_0 is the receiver noise power spectral density. The jamming steering vector is expressed as

$$\mathbf{a}_j(\theta_j, \phi_j) = \left[1 \;\; e^{j2\pi \frac{d_0}{\lambda} \cos\theta_j \cos\phi_j} \;\; \cdots \;\; e^{j(N-1)2\pi \frac{d_0}{\lambda} \cos\theta_j \cos\phi_j} \right]^T . \tag{2.29}$$

And the jammer space-time snapshot is

$$\mathbf{x}_j = \boldsymbol{\alpha}_j \otimes \mathbf{a}_j . \tag{2.30}$$

where $\boldsymbol{\alpha}_j$ is the random vector containing the jammer amplitudes, and is expressed as

$$\boldsymbol{\alpha}_j = \left[\alpha_{j,0} \;\; \alpha_{j,1} \cdots \alpha_{j,M-1} \right]^T . \tag{2.31}$$

Assume that the jammer samples from different pulses are uncorrelated and the jamming signal is stationary over a CPI, the jammer space-time covariance matrix is given by

$$\mathbf{R}_j = \left\{ \mathbf{x}_j \mathbf{x}_j^H \right\} = \mathbf{I}_M \otimes \left(\sigma^2 \xi_j \mathbf{a}_j \mathbf{a}_j^H \right) \tag{2.32}$$

where $\mathbf{I}_M$ is an $M \times M$ identity matrix.

2.2. Radar Data Transformation

The received radar echo data in space-time domain are transformed from the space-time domain to the beam-Doppler domain via 2D-DFT or MV method depending on the number of space-time snapshots available. If only one snapshot is available, the

radar echo data is transformed to the beam-Doppler domain using 2D-DFT. An MTI filter will be added for preprocessing purpose. In contrast, if multiple snapshots are available, the radar echo data is transformed to the beam-Doppler domain using the MV method and the MTI filter is not required.

The rest of this section is organized as follows. Radar data transformation from space-time domain to beam-Doppler domain via 2D-DFT is discussed in Section 2.2.1. The signal-to-clutter power ratio (SCR) improvement provided by the MTI filter is evaluated in Section 2.2.2. Finally, the MV method is presented in Section 2.2.3.

2.2.1. Radar data transformation using the 2D-DFT and the MTI filter

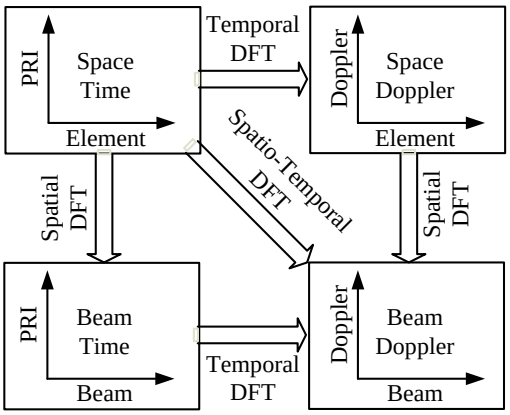

Figure 2.3 Four different interpretations of the received data related by DFT.

By performing DFT on the radar echo data in the space-time domain, three more different representations of the data may be produced, which are summarized in Figure 2.3. It should be noted that, in some literatures, space-time domain is called element space (pre-Doppler), beam-time domain is called beam space (pre-Doppler), space-Doppler domain is called element space (post-Doppler), and beam-Doppler domain is called beam space (post-Doppler). It could be seen from Figure 2.3 that the radar data

representation in beam-Doppler domain is obtained by applying the 2D-DFT (i.e. Spatio-Temporal DFT) to the radar data in the space-time domain. The radar data transformation process is detailed in the following.

Firstly, the radar data is transformed from space-time domain to the beam-space domain using spatial DFT. For convenience, the $NM \times 1$ target vector $\mathbf{x}_t$ is rearranged as an $M \times N$ matrix:

$$\mathbf{X}_t = \sigma^2 \xi_t \begin{bmatrix} 1 & e^{j2\pi\vartheta_t} & \cdots & e^{j2\pi(N-1)\vartheta_t} \\ e^{j2\pi\varpi_t} & e^{j2\pi(\varpi_t+\vartheta_t)} & \cdots & e^{j2\pi[\varpi_t+(N-1)\vartheta_t]} \\ \cdots & \cdots & \cdots & \cdots \\ e^{j2\pi(M-1)\varpi_t} & e^{j2\pi[(M-1)\varpi_t+\vartheta_t]} & \cdots & e^{j2\pi[(M-1)\varpi_t+(N-1)\vartheta_t]} \end{bmatrix}. \tag{2.33}$$

Applying 1-D Fourier Transform to the rows of $\mathbf{X}_t$ (spatial DFT), it follows that

$$F_{1D}(\mathbf{X}_t) = \sigma^2 \xi_t \begin{bmatrix} \sum_{n=0}^{N-1} e^{j2\pi n\vartheta_t} & \cdots & \sum_{n=0}^{N-1} e^{j2\pi n\left(\vartheta_t - \frac{N-1}{N}\right)} \\ e^{j2\pi\varpi_t} \sum_{n=0}^{N-1} e^{j2\pi n\vartheta_t} & \cdots & e^{j2\pi\varpi_t} \sum_{n=0}^{N-1} e^{j2\pi n\left(\vartheta_t - \frac{N-1}{N}\right)} \\ \cdots & \cdots & \cdots \\ e^{j2\pi(M-1)\varpi_t} \sum_{n=0}^{N-1} e^{j2\pi n\vartheta_t} & \cdots & e^{j2\pi(M-1)\varpi_t} \sum_{n=0}^{N-1} e^{j2\pi n\left(\vartheta_t - \frac{N-1}{N}\right)} \end{bmatrix}. \tag{2.34}$$

Assume that the clutter amplitudes α_k (k = 1, 2, …N_c) satisfy

$$E\left\{\left|\alpha_k\right|^2\right\} = \xi_k \sigma^2 = \frac{\sigma^2 P_t T_p G_t g \lambda^2 \sigma_k}{(4\pi)^3 N_0 L_s R_k^4} \tag{2.35}$$

where P_t is the peak transmit power, T_p is the transmit pulse width, G_t is the full-array transmit power gain, g is the element pattern, N_0 is the receive noise power spectral density, L_s is the system loss, and σ_k is the effective RCS of the k-th clutter patch.

Similarly, the $NM \times 1$ clutter vector $\mathbf{x}_c$ could also be organized as an $M \times N$ matrix:

$$\mathbf{X}_c = \begin{bmatrix} \sum_{k=1}^{Nc} \alpha_k & \sum_{k=1}^{Nc} \alpha_k e^{j2\pi\vartheta_k} & \cdots & \sum_{k=1}^{Nc} \alpha_k e^{j2\pi(N-1)\vartheta_k} \\ \sum_{k=1}^{Nc} \alpha_k e^{j2\pi\varpi_k} & \sum_{k=1}^{Nc} \alpha_k e^{j2\pi(\varpi_k+\vartheta_k)} & \cdots & \sum_{k=1}^{Nc} \alpha_k e^{j2\pi[\varpi_k+(N-1)\vartheta_k]} \\ \vdots & \vdots & \vdots & \vdots \\ \sum_{k=1}^{Nc} \alpha_k e^{j2\pi(M-1)\varpi_k} & \sum_{k=1}^{Nc} \alpha_k e^{j2\pi[(M-1)\varpi_k+\vartheta_k]} & \cdots & \sum_{k=1}^{Nc} \alpha_k e^{j2\pi[(M-1)\varpi_k+(N-1)\vartheta_k]} \end{bmatrix}. \quad (2.36)$$

The normalized Doppler ϖ_k and spatial frequency in ϑ_k are related by

$$\varpi_k = \frac{f_{d,k}}{f_r} = \frac{2v_a}{d_0 f_r}\vartheta_k = \beta\vartheta_k . \quad (2.37)$$

Applying 1-D Fourier Transform to the rows of $\mathbf{X}_c$, it follows that

$$F_{1D}(\mathbf{X}_C) = \begin{bmatrix} \sum_{k=1}^{Nc} \alpha_k \sum_{n=0}^{N-1} e^{j2\pi n\vartheta_k} & \cdots & \sum_{k=1}^{Nc} \alpha_k \sum_{n=0}^{N-1} e^{j2\pi n\left(\vartheta_k - \frac{N-1}{N}\right)} \\ \sum_{k=1}^{Nc} \alpha_k e^{j2\pi\beta\vartheta_i} \sum_{n=1}^{N-1} e^{j2\pi n\vartheta_k} & \cdots & \sum_{k=1}^{Nc} \alpha_k e^{j2\pi\beta\vartheta_k} \sum_{n=0}^{N-1} e^{j2\pi n\left(\vartheta_k - \frac{N-1}{N}\right)} \\ \cdots & \cdots & \cdots \\ \sum_{k=1}^{Nc} \alpha_k e^{j2\pi(M-1)\beta\vartheta_k} \sum_{n=1}^{N-1} e^{j2\pi n\vartheta_k} & \cdots & \sum_{k=1}^{Nc} \alpha_k e^{j2\pi(M-1)\beta\vartheta_k} \sum_{n=0}^{N-1} e^{j2\pi n\left(\vartheta_k - \frac{N-1}{N}\right)} \end{bmatrix}. \quad (2.38)$$

Likewise, the $NM \times 1$ jamming vector $\mathbf{x}_j$ and white Gaussian noise vector $\mathbf{x}_n$ could also be organized as $M \times N$ matrices $\mathbf{X}_j$ and $\mathbf{X}_n$, respectively. Assume that the 1-D spatial DFT of $\mathbf{X}_j$ and $\mathbf{X}_n$ are expressed as $F_{1D}(\mathbf{X}_j)$ and $F_{1D}(\mathbf{X}_n)$, respectively. The 1-D spatial DFT of radar data $\mathbf{X}$ for Hypothesis H_0 and H_1 is then expressed as

$$F_{1D}(\mathbf{X}) = \begin{cases} F_{1D}(\mathbf{X}_c) + F_{1D}(\mathbf{X}_n) + F_{1D}(\mathbf{X}_j) + F_{1D}(\mathbf{X}_t) & H_0 \\ F_{1D}(\mathbf{X}_c) + F_{1D}(\mathbf{X}_n) + F_{1D}(\mathbf{X}_j) & H_1 \end{cases}. \quad (2.39)$$

After the radar data in the space-time domain is transformed to the beam-time domain using spatial DFT, the double delay line canceller is applied to the beam-time image to reduce the clutter levels before further processing. Pulse cancellers are a type of the most popular and the simplest MTI filters. The impulse responses of the single delay line canceller (i.e. two pulse canceller), the double delay line canceller (i.e. three pulse canceller) and the triple delay line canceller (i.e. four pulse canceller) are, respectively, given by

$$h_1(t) = \delta(t) - \delta(t - T) \tag{2.40}$$

$$h_2(t) = \delta(t) - 2\delta(t - T) + \delta(t - 2T) \tag{2.41}$$

$$h_3(t) = \delta(t) - 3\delta(t - T) + 3\delta(t - 2T) - \delta(t - 3T) \tag{2.42}$$

where $\delta(.)$ is the delta function. The responses of different MTI filters that may be applied in the beam-time domain to reduce clutter levels are plotted in Figure 2.4, where the blue line, red line and the green line represent the two pulse canceller, three pulse canceller and the four pulse canceller, respectively.

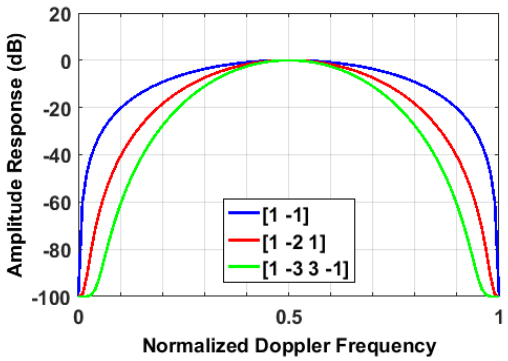

Figure 2.4 Responses of different MTI filters

The selection of the optimum MTI filter depends heavily on the intrinsic clutter motion and the clutter spectrum spread due to platform motion. In most radar

applications, the response of a single delay line canceller is not acceptable since it does not have a wide notch in the stop-band. It could be seen from Figure 2.4 that both the double delay line canceller and the triple delay line canceller have better response than the single delay line canceller in the stop-band and pass-band. However, the improved clutter cancellation performance of the higher-order MTI filters has an associated cost: 1) the detection of low-speed targets becomes more difficult [37]; 2) fewer pules are available for the coherent integration for MTI filters. Taking into consideration of both the advantages and disadvantages of the different MTI filters, a double delay line canceller is applied to the radar data in the beam-time domain. The double delay line canceller output of $F_{1D}(\mathbf{X})$ is given by

$$\tilde{F}_{1D}(\mathbf{X}) = \left[\tilde{F}_{1D,1}(\mathbf{X}) \;\; \tilde{F}_{1D,2}(\mathbf{X}) \cdots \tilde{F}_{1D,M-2}(\mathbf{X})\right]^T \tag{2.43}$$

where $\tilde{F}_{1D,m}(\mathbf{X})$ is the *m*-th row of $\tilde{F}_{1D}(\mathbf{X})$ and is given by

$$\tilde{F}_{1D,m}(\mathbf{X}) = F_{1D,m}(\mathbf{X}) - 2F_{1D,m+1}(\mathbf{X}) + F_{1D,m+2}(\mathbf{X}). \tag{2.44}$$

The MTI filter output in beam-time domain, $\tilde{F}_{1D}(\mathbf{X})$, is then transformed to the beam-Doppler domain using the temporal DFT. Finally, the radar data image in the beam-Doppler domain, $\tilde{F}_{2D}(\mathbf{X})$, for Hypothesis H_0 and H_1 is expressed as

$$\tilde{F}_{2D}(\mathbf{X}) = \begin{cases} \tilde{F}_{2D}(\mathbf{X}_c) + \tilde{F}_{2D}(\mathbf{X}_j) + \tilde{F}_{2D}(\mathbf{X}_n) & : H_0 \\ \tilde{F}_{2D}(\mathbf{X}_c) + \tilde{F}_{2D}(\mathbf{X}_j) + \tilde{F}_{2D}(\mathbf{X}_n) + \tilde{F}_{2D}(\mathbf{X}_t) & : H_1 \end{cases} \tag{2.45}$$

where $\tilde{F}_{2D}(\mathbf{X}_c)$, $\tilde{F}_{2D}(\mathbf{X}_j)$, $\tilde{F}_{2D}(\mathbf{X}_n)$ and $\tilde{F}_{2D}(\mathbf{X}_t)$ represent the clutter component, jamming component, noise component and the target component of the beam-Doppler image,

respectively. It should be noted that the beam-Doppler image obtained in (2.45) via 2D-DFT is of low image resolution, which only consists of a total of *MN* pixels.

2.2.2. SCR improvement provided by MTI filter

In previous section, the double delay line canceller is applied to the radar data image in the beam-time domain to reduce the clutter levels before further data transformation. The improvement of SCR provided by the double delay line canceller is demonstrated in the following. If the radar data is transformed from the beam-time domain to the beam-Doppler domain directly without using the MTI filter, the target component of the beam-Doppler image is given by

$$F_{2D}(\mathbf{X}_t)=\sigma^2\xi_t\begin{bmatrix}\sum_{m=0}^{M-1}\sum_{n=0}^{N-1}e^{j2\pi(m\varpi_t+n\vartheta_t)} & \cdots & \sum_{m=0}^{M-1}\sum_{n=0}^{N-1}e^{j2\pi\left[m\varpi_t+n\left(\vartheta_t-\frac{N-1}{N}\right)\right]}\\ \sum_{m=0}^{M-1}\sum_{n=0}^{N-1}e^{j2\pi\left[m\left(\varpi_t-\frac{1}{M}\right)+n\vartheta_t\right]} & \cdots & \sum_{m=0}^{M-1}\sum_{n=0}^{N-1}e^{j2\pi\left[m\left(\varpi_t-\frac{1}{M}\right)+n\left(\vartheta_t-\frac{N-1}{N}\right)\right]}\\ \cdots & \cdots & \cdots\\ \sum_{m=0}^{M-1}\sum_{n=0}^{N-1}e^{j2\pi\left[m\left(\varpi_t-\frac{M-1}{M}\right)+n\vartheta_t\right]} & \cdots & \sum_{m=0}^{M-1}\sum_{n=0}^{N-1}e^{j2\pi\left[m\left(\varpi_t-\frac{M-1}{M}\right)+n\left(\vartheta_t-\frac{N-1}{N}\right)\right]}\end{bmatrix}. \quad (2.46)$$

Specifically, when $\vartheta_t = 0$,

$$F_{2D}(\mathbf{X}_t)|_{\vartheta_t=0}\approx\sigma^2\xi_t\begin{bmatrix}N\sum_{m=0}^{M-1}e^{j2\pi m\varpi_t} & 0 & \cdots & 0\\ N\sum_{m=0}^{M-1}e^{j2\pi m\left(\varpi_t-\frac{1}{M}\right)} & 0 & \cdots & 0\\ \cdots & \vdots & \cdots & \cdots\\ N\sum_{m=0}^{M-1}e^{j2\pi m\left(\varpi_t-\frac{M-1}{M}\right)} & 0 & \cdots & 0\end{bmatrix}. \quad (2.47)$$

The absolute value of $F_{2D}(\mathbf{X}_t)|_{\vartheta_t=0}$ is given by

$$\left|F_{2D}(\mathbf{X}_t)|_{\vartheta_t=0}\right| = \sigma^2\xi_t \begin{bmatrix} N\left|\dfrac{\sin(M\pi\varpi_t)}{\sin(\pi\varpi_t)}\right| & 0 & \cdots & 0 \\ N\left|\dfrac{\sin\left(M\pi\left(\varpi_t-\dfrac{1}{M}\right)\right)}{\sin\left(\pi\left(\varpi_t-\dfrac{1}{M}\right)\right)}\right| & 0 & \cdots & 0 \\ \vdots & \vdots & \vdots & \vdots \\ N\left|\dfrac{\sin\left(M\pi\left(\varpi_t-\dfrac{M-1}{M}\right)\right)}{\sin\left(\pi\left(\varpi_t-\dfrac{M-1}{M}\right)\right)}\right| & 0 & \cdots & 0 \end{bmatrix}. \tag{2.48}$$

In contrast, if the double delay line canceller is applied to the radar data image in the beam-time domain, for $\vartheta_t = 0$, the target component of the MTI filter output, $\tilde{F}_{1D}(\mathbf{X}_t)|_{\vartheta_t=0}$, is expressed as an $(M\text{-}2)\times N$ matrix

$$\tilde{F}_{1D}(\mathbf{X}_t)|_{\vartheta_t=0} \approx \sigma^2\xi_t \begin{bmatrix} N(1-2e^{j2\pi\varpi_t}+e^{j4\pi\varpi_t}) & 0 & \cdots & 0 \\ Ne^{j2\pi\varpi_t}(1-2e^{j2\pi\varpi_t}+e^{j4\pi\varpi_t}) & 0 & \cdots & 0 \\ \vdots & \vdots & \vdots & \vdots \\ Ne^{j2\pi(M-3)\varpi_t}(1-2e^{j2\pi\varpi_t}+e^{j4\pi\varpi_t}) & 0 & \cdots & 0 \end{bmatrix}. \tag{2.49}$$

And the target component of the beam-Doppler image is given by

$$\tilde{F}_{2D}(\mathbf{X}_t)|_{\vartheta_t=0} \approx \sigma^2\xi_t \begin{bmatrix} N\left(1-e^{j2\pi\varpi_t}\right)\left(1-e^{j2\pi(M-2)\varpi_t}\right) & 0 & \cdots & 0 \\ N\left(1-e^{j2\pi\varpi_t}\right)\left(1-e^{j2\pi(M-2)\varpi_t}\right)\sum_{m=0}^{M-3} e^{j2\pi m\left(\varpi_t-\frac{1}{M}\right)} & 0 & \cdots & 0 \\ \cdots & \vdots & \cdots & \cdots \\ N\left(1-e^{j2\pi\varpi_t}\right)\left(1-e^{j2\pi(M-2)\varpi_t}\right)\sum_{m=0}^{M-3} e^{j2\pi m\left(\varpi_t-\frac{M-3}{M}\right)} & 0 & \cdots & 0 \end{bmatrix}. \tag{2.50}$$

It should be noted that $\left|\left(1-e^{j2\pi\varpi_t}\right)\left(1-e^{j2\pi(M-2)\varpi_t}\right)\right| \geq 1$ for $\varpi_t \geq 0.17$, which means that as long as the normalized target Doppler is greater than 0.17, the SNR is enhanced at the double delay line canceller. Even in the case where the target is slow moving, e.g. $\varpi_t = 0.1$, the SCR is also expected to be increase since the ground is stationary.

The SCR improvement provided by the double delay line canceller could be investigated based on the improvement factor (IF), i.e. the SCR at the output of the double delay line canceller divided by the input SCR. The Fourier Transform of the three pulse canceller impulse response is expressed as

$$H(f) = 1 - 2e^{-j2\pi fT} + e^{-j4\pi fT}. \tag{2.51}$$

The clutter power at the output of an MTI is given by

$$C_o = \int_{-\infty}^{\infty} W(f)\left|H(f)\right|^2 df \ . \tag{2.52}$$

where $W(f)$ is the Gaussian-shaped clutter power spectrum and is expressed as

$$W(f) = \frac{P_c}{\sqrt{2\pi}\sigma_t} e^{-\frac{f^2}{2\sigma_t^2}} \tag{2.53}$$

where P_c and σ_t are the clutter power and the clutter root mean square (rms) frequency, respectively. Assuming $f << f_r$, which is valid since the clutter power is more significant for small *f*, it follows that

$$C_o \approx \frac{16P_c\pi^4}{f_r^4} \int_{-\infty}^{\infty} \frac{1}{\sqrt{2\pi\sigma_t^2}} e^{-\frac{f^2}{2\sigma_t^2}} f^4 df = \frac{4P_c\pi^2\sigma_t^2}{3}. \tag{2.54}$$

The MTI improvement factor using three pulse canceller is then:

$$I_0 = \frac{P_c}{C_o}\left[T\int_{f_r/2}^{f_r/2}\left|H(f)\right|^2 df\right] = \frac{1}{8\left(\pi\sigma_{pm}T\right)^4}. \tag{2.55}$$

2.2.3. Radar data transformation using the MV method

In the MV method, the radar data in the beam-Doppler domain are estimated by filtering the space-time radar data with a bank of two-dimensional narrowband beam-

Doppler bandpass filters. The beam-Doppler bandpass filters are configured to minimize the variance of the outputs of a data-adaptive narrowband filter at each beam and each Doppler frequency of interest in order to reject unwanted signal power in an optimum way [38-42]. To develop the MV algorithm for the beam-Doppler representation of airborne radar data, the power density of radar echo data at beam angle ϑ_s, i.e., spatial frequency, and the normalized Doppler frequency ϖ_s has to be estimated. In order to avoid altering the power of the transformed radar data, the peak response $G(\vartheta_s, \varpi_s)$ of the 2-D bandpass filter in the MV algorithm is constrained to be one, or equivalently

$$G(\vartheta_s, \varpi_s) = \sum_{m=0}^{M-1} \sum_{n=0}^{N-1} g_1(m) g_2(n) e^{-j2\pi(m\varpi_s + n\vartheta_s)} = 1 \tag{2.56}$$

where $g_1(m)$ and $g_2(n)$ are the narrowband beamformer and Doppler filter in the beam and Doppler domains, respectively. The constraint in (2.56) can be further expressed using vector notations as

$$\mathbf{g}^H \mathbf{v}(\vartheta_s, \varpi_s) = \mathbf{v}(\vartheta_s, \varpi_s) \mathbf{g}^H = 1 \tag{2.57}$$

where

$$\mathbf{g} = [g(0,0) \ \cdots g(0, N-1) \ \cdots g(m,n) \cdots g(M-1, N-1)]^T \tag{2.58}$$

$$g(m,n) = g_1(m) g_2(n) \tag{2.59}$$

$$\mathbf{v}(\vartheta_s, \varpi_s) = [1 \, e^{j2\pi\vartheta_s} \cdots e^{j(N-1)2\pi\vartheta_s} \cdots e^{j2\pi[(m-1)\varpi_s + (n-1)\vartheta_s]} \cdots e^{j2\pi[(M-1)\varpi_s + (N-1)\vartheta_s]}]^T . \tag{2.60}$$

The total power, i.e. the variance of the filter bank output y in terms of covariance matrix **R** of the input data is given by [38]

$$E\{|y|^2\} = \mathbf{g}^H \mathbf{R} \mathbf{g} . \tag{2.61}$$

To minimize the variance of the filter output in (2.61) subject to the constraint given in (2.56), one can obtain the coefficients of the optimum filter, which gives the most accurate estimation of the input data in beam-Doppler domain, using the Lagrange multiplier as follows

$$\mathbf{g}_{opt} = \arg\min_{\mathbf{g}} E\{|y|^2\} = \frac{\mathbf{R}^{-1}\mathbf{v}(\vartheta_s, \varpi_s)}{\mathbf{v}^H(\vartheta_s, \varpi_s)\mathbf{R}^{-1}\mathbf{v}(\vartheta_s, \varpi_s)}. \tag{2.62}$$

The minimum value of $E\left\{|y|^2\right\}$ is given by

$$\min E\left\{|y|^2\right\} = \mathbf{g}_{opt}^H \mathbf{R}\mathbf{g}_{opt} = \frac{1}{\mathbf{v}^H(\vartheta_s, \varpi_s)\mathbf{R}^{-1}\mathbf{v}(\vartheta_s, \varpi_s)}. \tag{2.63}$$

Therefore, using the MV method, the power spectral density $\hat{\mathbf{p}}(\vartheta_s, \varpi_s)$ of the radar echo signals in the beam-Doppler domain is obtained as

$$\hat{\mathbf{p}}(\vartheta_s, \varpi_s) = \min E\left\{|y|^2\right\}. \tag{2.64}$$

Further considering (2.63), the airborne radar echo signals with or without target are obtained as the following image in the beam-Doppler domain

$$\mathbf{z}(\vartheta_s, \varpi_s) = \frac{1}{\hat{\mathbf{p}}(\vartheta_s, \varpi_s)} = \begin{cases} \mathbf{v}^H(\vartheta_s, \varpi_s)\mathbf{R}_I^{-1}\mathbf{v}(\vartheta_s, \varpi_s) & : H_0 \\ \mathbf{v}^H(\vartheta_s, \varpi_s)(\mathbf{R}_I + \mathbf{R}_t)^{-1}\mathbf{v}(\vartheta_s, \varpi_s) & : H_1 \end{cases} \tag{2.65}$$

where $\mathbf{R}_I$ is the interference matrix given by

$$\mathbf{R}_I = \mathbf{R}_c + \mathbf{R}_j + \mathbf{R}_n. \tag{2.66}$$

If the target is present in the expected target direction (ϑ_t, ϖ_t), using Woodbury's identity, it follows that

$$
\begin{aligned}
&(\mathbf{R}_I + \mathbf{R}_t)^{-1}\mathbf{v}(\vartheta_t, \varpi_t) \\
&= (\mathbf{R}_I + \sigma^2 \xi_t \mathbf{v}_t(\vartheta_t, \varpi_t)\mathbf{v}_t^H(\vartheta_t, \varpi_t))^{-1}\mathbf{v}_t(\vartheta_t, \varpi_t) \\
&= \left(1 - \frac{\mathbf{v}_t^H(\vartheta_t, \varpi_t)\mathbf{R}_I^{-1}\mathbf{v}_t(\vartheta_t, \varpi_t)}{1/(\sigma^2\xi_t) + \mathbf{v}_t^H(\vartheta_t, \varpi_t)\mathbf{R}_I^{-1}\mathbf{v}_t(\vartheta_t, \varpi_t)}\right)\mathbf{R}_I^{-1}\mathbf{v}_t(\vartheta_t, \varpi_t). \\
&= \frac{\mathbf{R}_I^{-1}\mathbf{v}_t(\vartheta_t, \varpi_t)}{1 + \sigma^2\xi_t \mathbf{v}_t^H(\vartheta_t, \varpi_t)\mathbf{R}_I^{-1}\mathbf{v}_t(\vartheta_t, \varpi_t)}
\end{aligned}
\tag{2.67}
$$

Hence (2.65) is rewritten as

$$
\mathbf{z}(\vartheta_t, \varpi_t) = \frac{1}{\hat{\mathbf{p}}(\vartheta_t, \varpi_t)} = \begin{cases} \mathbf{v}_t^H(\vartheta_t, \varpi_t)\mathbf{R}_I^{-1}\mathbf{v}_t(\vartheta_t, \varpi_t) & : H_0 \\ \dfrac{\mathbf{v}_t^H(\vartheta_t, \varpi_t)\mathbf{R}_I^{-1}\mathbf{v}_t(\vartheta_t, \varpi_t)}{1 + \sigma^2\xi_t \mathbf{v}_t^H(\vartheta_t, \varpi_t)\mathbf{R}_I^{-1}\mathbf{v}_t(\vartheta_t, \varpi_t)} & : H_1 \end{cases}. \tag{2.68}
$$

Or equivalently,

$$
\hat{\mathbf{p}}(\vartheta_t, \varpi_t) = \begin{cases} \dfrac{1}{\mathbf{v}_t^H(\vartheta_t, \varpi_t)\mathbf{R}_I^{-1}\mathbf{v}_t(\vartheta_t, \varpi_t)} & : H_0 \\ \dfrac{1}{\mathbf{v}_t^H(\vartheta_t, \varpi_t)\mathbf{R}_I^{-1}\mathbf{v}_t(\vartheta_t, \varpi_t)} + \sigma^2\xi_t & : H_1 \end{cases}. \tag{2.69}
$$

It should be noted that, since $\mathbf{R}_I$ is unknown, it has to be estimated from the radar data. Assume that U independent measurements are available, $\mathbf{R}_I$ is estimated as

$$
\hat{\mathbf{R}}_I = \frac{1}{U}\sum_{i=1}^{U}\mathbf{x}_i\mathbf{x}_i^H \tag{2.70}
$$

where $\mathbf{x}_i$ is the i-th interference training data vector. Based on experimental results, the radar data could be transformed into beam-Doppler domain without significant information loss as long as U meets the following requirement

$$
U \geq 3\sqrt{MN}\,. \tag{2.71}
$$

2.3. Minimum-distance-based Region Growing (MDB-RG) Algorithm

After the radar data is transformed into the beam-Doppler domain using the 2D-DFT or the MV method, denoising processing is performed to remove noise signals. In denoising processing, if the magnitude of an image pixel is less than a pre-defined threshold, T_0, the pixel is considered to be white noise and its value will be re-set as zero; otherwise, the pixel is considered to be either target or clutter and its value remains unchanged. There is a trade-off between the probabilities of the two types of errors in the threshold selection process, which is detailed in Section 2.6. With the white noise removed from the beam-Doppler image, the remaining non-zero image pixels are either the target or the interference signals. Since the moving target and the interference signals generally have different image features in the beam-Doppler domain, they could be separated from each other using region growing (RG).

RG is a fundamental image segmentation technique, which is essentially a process of pixel classification, wherein the image pixels are segmented into subsets, or regions, that are uniform in some measurable properties such as brightness and color [43]. Although RG has been one of the most popular and intensively studied image-segmentation methods [43-48] and has been used for many different applications [43-45, 47], none of the existing RG algorithms is applicable to the moving target detection problem in this chapter. Therefore, an innovative MDB-RG algorithm is developed in the following to separate the target signal from the interferences for moving target detection.

2.3.1. Basic principles of MDB-RG algorithm

Before the MDB-RG algorithm is developed, some concepts and terminologies need to be defined first.

Definition 1 (*Pixel cluster*): A pixel cluster is defined as a set of non-zero pixels for a data image in the beam-Doppler domain.

Definition 2 (*Pixel distance*): The distance between two nonzero pixels $p(i_d, i_a)$ and $q(j_d, j_a)$, where the subscripts *d* and *a* represent the Doppler index and beam index, respectively, in a beam-Doppler image. Specifically, the distance between two pixels in this chapter is defined as

$$\|p, q\| = \sqrt{\gamma_d R_d^2 (i_d - j_d)^2 + \gamma_a R_a^2 (i_a - j_a)^2} \tag{2.72}$$

where R_d and R_a are the actual image resolutions in Doppler and beam domains, respectively; γ_d and γ_a are the weighting parameters used to adjust the effects of Doppler and beam resolutions, respectively.

Definition 3 (*Pixel connectivity*): Two non-zero pixels P_A and P_B in a beam-Doppler image are defined as connected under the minimum range Λ, if

$$\|P_A, P_B\| \le \Lambda \tag{2.73}$$

or if a series of ordered non-zero pixels $\{P_1, P_2, \cdots, P_U\}$ can be found such that the following conditions are simultaneously satisfied:

$$\|P_A, P_1\| \le \Lambda \tag{2.74}$$

$$\|P_u, P_{u+1}\| \le \Lambda, u = 1, 2, \cdots, U-1,\ U \ge 2 \tag{2.75}$$

$$\|P_U, P_B\| \le \Lambda, U \ge 1 \tag{2.76}$$

Definition 4 (*Connected cluster*): a connected cluster is a pixel cluster in which any two pixels are connected.

Definition 5 (*Feature block*): a feature block is a connected cluster in which any pixel inside is not connected to any pixel outside the cluster.

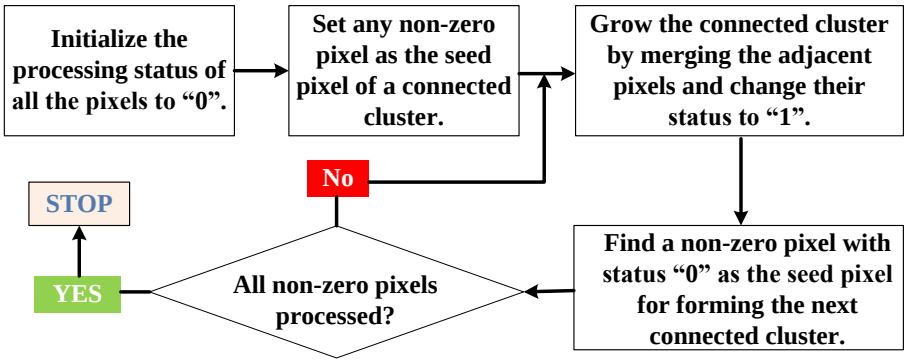

Figure 2.5 Flowchart of the MDB-RG algorithm

The flowchart of the MDB-RG algorithm is shown in Figure 2.5. Prior to the application of the RG algorithm, all non-zero pixels in a radar image are labeled as processing status "0"; but if any of them is merged into a connected cluster, the processing status of the pixel is switched "1". Any non-zero image pixel with a status of "0" can be selected as the "seed" pixel of an initial connected cluster. A connected cluster is "grown" from its boundary pixels only by merging into the cluster all adjacent outside pixels with "0" status within the minimum distance of the boundary. The growing of the connected cluster continues along its new boundary until it reaches the image boundary or there are no status "0" non-zero pixels within the minimum distance; and the final connected cluster becomes a feature block. The same MDB-RG process is repeated until each of the non-zero pixels is in a feature block. The final result of MDB-RG consists of multiple separated features blocks and should be independent of the selection of the

initial “seed” pixels or the order of the region-growing performed on the boundary pixels in generating feature blocks.

2.3.2. Implementation of the MDB-RG algorithm on the radar data image

Assume that the radar data image obtained in beam-Doppler domain are expressed as

$$\mathbf{P} = [\, p(x, y), x = 1, 2, \cdots, X \quad y = 1, 2, \cdots, Y \,] \tag{2.77}$$

where x and y are the image pixel indices in Doppler and beam domains, respectively; X and Y are the image resolution in the beam domain and the Doppler domain, respectively. When the radar data image obtained in beam-Doppler domain is obtained via 2D-DFT, it is easy to obtain $X = M, Y = N$, and the total number of pixels are given by MN. In contrast, when the radar data image in beam-Doppler domain is obtained using the MV method, the image resolution is determined by the step size of the Doppler frequency and the spatial frequency.

After denoising processing, the non-zero radar data become a set of I non-zero pixels, which are given by

$$\boldsymbol{\upsilon} = \{\, p(x_i, y_i) > 0, i = 1, 2, \cdots, I \,\}. \tag{2.78}$$

The pixels in (2.78) represent either target or interference signals and their processing status are set to be “0” prior to the MDB-RB processing, i.e.

$$\mathbf{S} = \{ s(x_i, y_i) = 0, i = 1, 2, \cdots, I \} \tag{2.79}$$

where $s(x_i, y_i)$ represents the processing status of the pixel of index (x_i, y_i).

The specific steps of carrying out the MDB-RG algorithm on the radar data image in (2.78) are detailed as follows.

Step 1: Initialize the MDB-RG for the radar image by setting any non-zero pixel k $(1 \le k \le I)$ in (2.78) as the seed pixel of a connected cluster **C** with the initial region growing result **B** containing no feature blocks, i.e. $\mathbf{B} = \{\varnothing\}$. It follows that

$$\mathbf{C} = \{p(x_k, y_k)\} \tag{2.80}$$

$$s(x_k, y_k) \Leftarrow 1 \tag{2.81}$$

Step 2: Find all boundary pixels of **C** and grow the connected cluster by merging the adjacent pixels within the minimum distance of the boundary pixels. For an arbitrary boundary pixel $p_A = p(x_l, y_l)$, the 8 adjacent outside pixels, which are represented by $\{\, p_B^i = p(x_l^i, y_l^i), i = 1, 2, \cdots, 8 \,\}$, are considered to be merged into the connected cluster **C**. The indices (x_l^i, y_l^i) are related to the index (x_l, y_l) by

$$x_l^i = \begin{cases} x_l - 1 & i = 1, 2, 3 \\ x_l & i = 4, 5 \\ x_l - 1 & i = 6, 7, 8 \end{cases}, \quad y_l^i = \begin{cases} y_l - 1 & i = 1, 4, 6 \\ y_l & i = 2, 7 \\ x_l - 1 & i = 3, 5, 8 \end{cases} \tag{2.82}$$

The pixel $p(x_l^i, y_l^i)$ is merged into **C**, i.e.

$$\mathbf{C} \Leftarrow \mathbf{C} \cup p_B^i, \; s(m_l^i, n_l^i) \Leftarrow 1 \tag{2.83}$$

if and only if the following conditions are met simultaneously:

$$1 \le x_l^i \le X, \; 1 \le y_l^i \le Y \tag{2.84}$$

$$p(x_l^i, y_l^i) > 0, s(x_l^i, y_l^i) = 0 \tag{2.85}$$

$$\left\| p_A, p_B^i \right\| \le \Lambda . \tag{2.86}$$

The above region-growing process is repeated for all the boundary pixels of **C**.

Step 3: Identify the new boundary pixels of the expanded connected cluster **C** and repeat **Step 2** until **C** cannot be grown anymore and it becomes a feature block. The region growing result is updated as:

$$\mathbf{B} \Leftarrow \mathbf{B} \cup \mathbf{C} \tag{2.87}$$

Step 4: Find a non-zero pixel with its processing status equal to "0" as the seed pixel for forming the next feature block and repeat **Steps** 1-3 until all non-zero pixels are processed with the status equal to "1", and the final processing result **B** is the collection of one or multiple feature blocks.

With the above MDB-RG algorithm applied, an airborne radar data image in beam-Doppler domain is segmented into multiple disjointed feature blocks. Because the generated feature blocks represent clutters and target, the segmentation results should be unique and independent of how the MDB-RG is performed, as stated in the following theorem.

Theorem 1: The MDB-RG processing results of radar image data are unique and independent of the initial pixels chosen for region-growing or the orders or directions of the region growing when the MDB-RG is implemented.

Proof: It is assumed that a non-zero radar image pixel p_z belongs to two different feature blocks $\mathbf{B}_1$ and $\mathbf{B}_2$ generated from two separate applications of the MDB-RG algorithm to the same radar image data. Consider two arbitrary pixels p_{z1} and p_{z2} satisfying the following conditions:

$$p_{z1} \in \mathbf{B}_1,\ p_z \neq p_{z1},\ p_{z2} \in \mathbf{B}_2, \text{ and } p_z \neq p_{z2} \tag{2.88}$$

Since all pixels inside a feature block are connected, there is a unique ordered pixel path from p_{z1} to p_z, according the definitions in (2.73)-(2.76). Similarly, there

should be a unique ordered pixel path from p_z to p_{z2} as well. Combining those two paths, one can conclude that there is a unique, ordered pixel path from p_{z1} to p_{z2} satisfying pixel connection condition. Therefore, any pixel in $\mathbf{B}_1$ is connected to any other pixel in $\mathbf{B}_2$. Hence, $\mathbf{B}_1$ and $\mathbf{B}_2$ actually are the same feature block, which contradicts the original assumption that $\mathbf{B}_1$ and $\mathbf{B}_2$ are different feature blocks. By far, it is proved that the MDB-RG processing result of a radar data image in Doppler-beam domain is unique and is indifferent to the region growing procedures.

2.4. Target/Interference Recognition based on the Size of Feature Blocks

With the MDB-RG processing, the beam-Doppler radar data image becomes a collection of *feature blocks* that are either a target or clutters. By comparing the pixel concentration level of each obtained feature block measured by a metric called *block size* with a pre-selected threshold, the identity of *feature blocks* can be recognized as either target or clutters. To further develop a target detection algorithm based on segmented radar image with MDB-RG, the size of a pixel cluster or a feature block for feature-based target detection has to be defined.

Definition 6 (*cluster/block size*): The size of a pixel cluster/feature block containing Ξ pixels $\{p_0, p_1, p_2, \ldots, p_\Xi\}$ is defined as the maximum distance between two pixels in the cluster/feature block:

$$\Gamma = \begin{cases} \max\limits_{j,k} \left\| p_j, p_k \right\|, \ 1 \le j,k \le \Xi, & \text{if } \Xi \ge 2 \\ 0, & \text{if } \Xi = 1 \end{cases}. \tag{2.89}$$

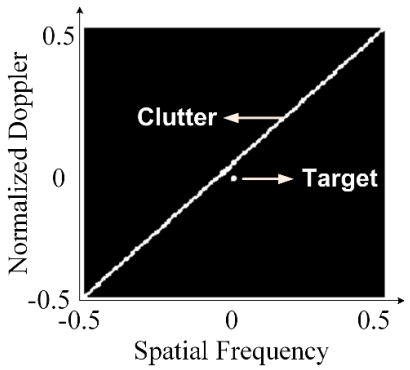

Figure 2.6 Black and white Beam-Doppler image.

In target/interference recognition processing, the following detection criterion is used to determine whether a feature block $\mathbf{B}_i$ with a block size of Γ_i is target or interference:

$$\Gamma_i \begin{cases} \leq \Gamma_0 \Rightarrow \text{Feature Block is Target} \\ > \Gamma_0 \Rightarrow \text{Feature Block is Interference} \end{cases} \tag{2.90}$$

where target/interference recognition threshold Γ_0 is determined by the image resolution, the number of transmitted pulses in a CPI, and the number of data elements. In practice, Γ_0 is set according to the size of generated feature blocks. The detailed steps are as following:

Step 1: Convert the beam-Doppler image to black and white image. An illustration example is provided in Figure 2.6 under the assumption that $M = N = 18$.

Step 2: Count the number of 1s in the whole image matrix, record the number as n_1.

Step 3: Count the number of 1s in the center $1/N$ columns of the image matrix (i.e. mainlobe data), record the number as n_2.

Step 4: Assume that the generated feature blocks are of sizes $\Gamma_1, \Gamma_2, \ldots, \Gamma_W$ and the maximum feature block size is $\Gamma_{\max}$. Γ_0 is then set as $\Gamma_{\max} / \left[\left(n_1 - n_2 / \varepsilon \right) / \left(n_2 / \varepsilon \right) \right]$, where $\varepsilon = 2 \sim 3$ depending on the RCS of the expected target.

2.5. Simulation Results

In this section, simulations are carried out to demonstrate the performance of the proposed BDIFR algorithm. According to [24], clutter heterogeneity could be classified into five types: amplitude heterogeneity, spectral heterogeneity, CNR-induced spectral mismatch, edge effects, and target-like signals in the secondary data (TSD). In this section, two types of clutter heterogeneity are considered: amplitude heterogeneity and spectral heterogeneity.

Amplitude heterogeneity is the most common type of clutter heterogeneity. The possible causes of amplitude heterogeneity, which is the most common type of clutter heterogeneity, include shadowing and obscuration, range-dependent change in clutter reflectivity, and strong stationary discretes. In this section, we consider the inhomogeneous ground clutter where clutter reflectivity varies over range and angle, and it is assumed that the clutter power follows the Gamma probability distribution. It should be noted that the larger the ratio of the mean of the Gamma distribution to the standard deviation (mean/std), the more homogeneous the clutter is. Specifically, according to [39], when mean/std is greater than 1/3, only minor SINR loss is induced with respect to the RMB rule for conventional STAP. Therefore, to demonstrate the performance of the proposed algorithm in inhomogeneous ground clutter, we set mean/std as 1/10.

Spectral heterogeneity of clutter is caused by intrinsic clutter motion (ICM) due to soft scatterers such as trees, ocean waves and weather effects [24]. Since the null width for clutter suppression is set to fit the mean spectral spread, when ICM exists the null width would be too narrow for some range cells and too wide for others, which may lead to either residue clutter that degrades SINR and increases false alarm rate, or target signal cancellation (i.e. over-nulling). In simulations, we assume that the primary data has an rms clutter velocity spread of 0.5 m/s.

2.5.1. Scenario 1: 2D-DFT is used for radar data transformation

Table 2.1 Radar system, interference and target parameters used in Example 1 to Example 4

			Example 1	Example 2	Example 3	Example 4
Radar System Parameters	Number of antenna elements	N	22	32	32	32
	Number of pulses per CPI	M	22	32	32	32
	PRF	f_r	300 Hz	300 Hz	300 Hz	300 Hz
	Wavelength	λ	0.67 m	0.67 m	0.67 m	0.67 m
	Platform height	H	9000 m	9000 m	9000 m	9000 m
	Platform velocity	v_a	50 m/s	50 m/s	90 m/s	50 m/s
Interference Parameters	Clutter range	R_c	13650m	13650m	13650m	13650m
	Clutter velocity spread (rms)	σ_v	0.5 m/s	0.5 m/s	0.5 m/s	0.5 m/s
	Number of clutter patches	N_c	360	360	360	360
	CNR	ξ_c	40 dB	40 dB	40 dB	40 dB
	Azimuth angle of the jammer	θ_j	---	---	---	0.25
	Elevation angle of the jammer	ϕ_j	---	---	---	0
	JNR	ξ_j	---	---	---	30 dB
Target Parameters	Target azimuth angle	ϕ_t	0	0	0	0
	Target elevation angle	θ_t	0.07	0.07	0.07	0.07
	Target spatial frequency	ϑ_t	0	0	0	0
	Target Doppler frequency	f_d	75 Hz	-50 Hz	75 Hz	-50 Hz
	Target normalized Doppler	ϖ_t	0.25	-0.17	0.25	-0.17
	SNR	ξ_t	0 dB	0 dB	0 dB	0 dB

When only one snapshot is available, 2D-DFT is used to transform the space-time domain radar data to the beam-Doppler domain. Since the beam-Doppler image obtained via 2D-DFT is of low image resolution, the MTI filter (e.g. three pulse canceller) is applied to the image to reduce the clutter levels and to prepare the image for further

processing. Four examples are given to demonstrate the performance of the proposed BDIFR algorithm in this scenario, and the radar parameters used in simulation are shown in Table 2.1. The radar mainlobe is assumed to be pointing at the expected target direction. The BDIFR processing results for *Example 1*, *Example 2*, *Example 3*, and *Example 4* are shown in Figure 2.7, Figure 2.8, Figure 2.9, and Figure 2.10, respectively. It could be seen in all these figures that target feature blocks and the interference feature blocks are successfully separated.

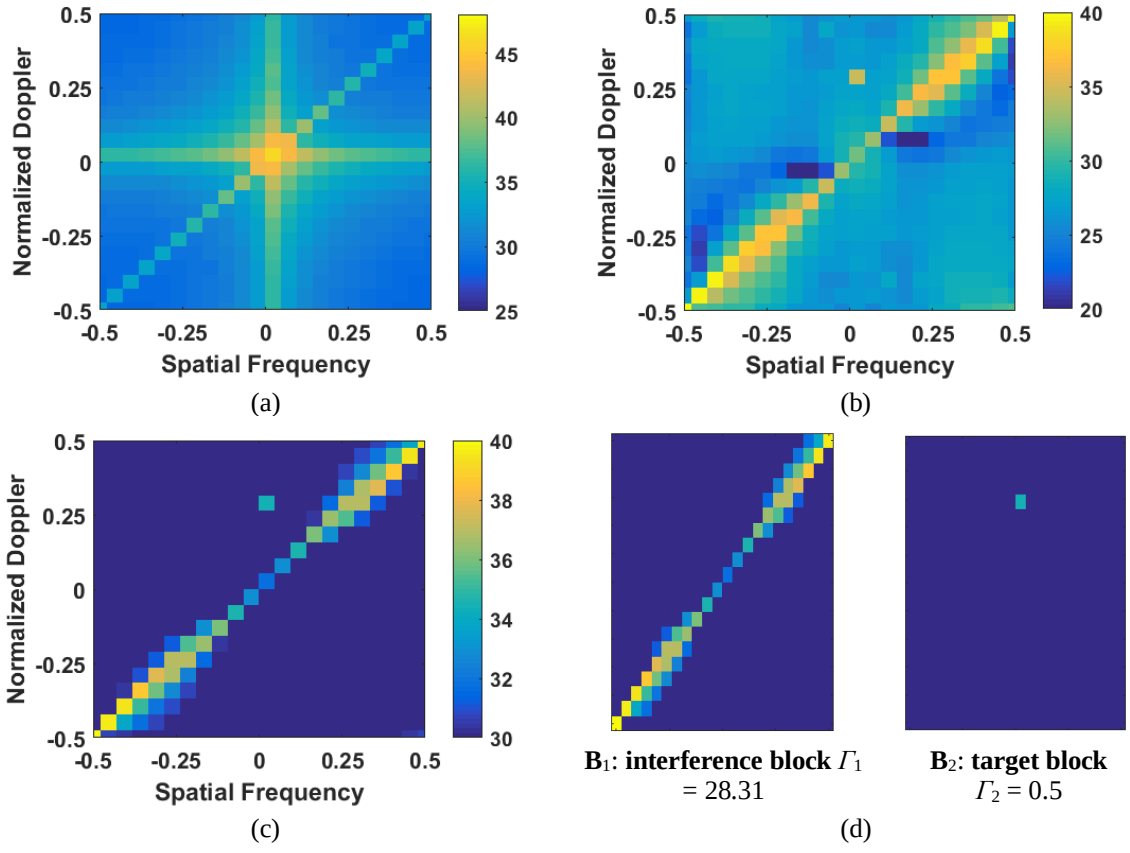

Figure 2.7 BDIFR processing results for Example 1.
(a) Radar data image obtained in beam-Doppler domain via 2D-DFT; (b) MTI filter (three pulse canceller) output; (c) denoised radar data image and (d) feature blocks generated via MBD-RG.

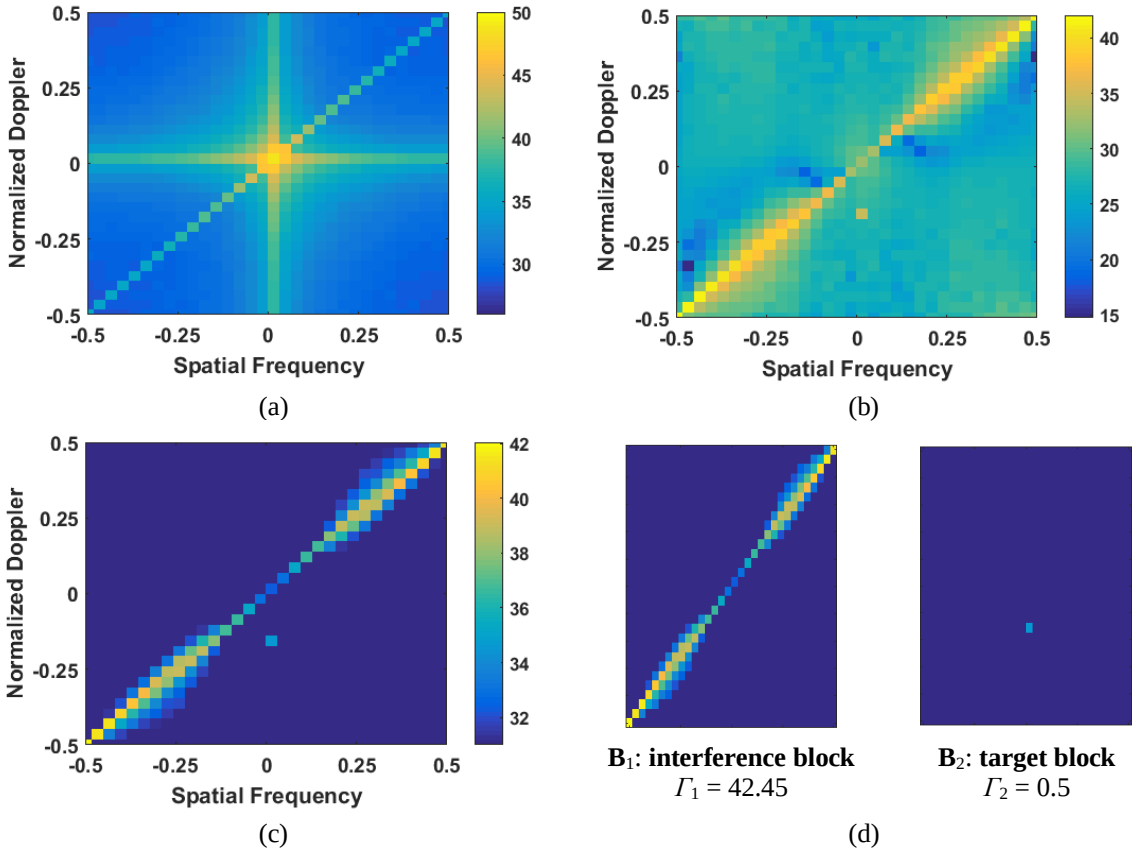

Figure 2.8 BDIFR processing results for Example 2.
(a) Radar data image obtained in beam-Doppler domain via 2D-DFT; (b) MTI filter (three pulse canceller) output; (c) denoised radar data image and (d) feature blocks generated via MBD-RG.

In *Example 1*, *Example 2* and *Example 3*, the interference signal consists of only ground clutters and the jamming signal doesn't exist. In both *Example 1* and *Example 2*, the slope of the clutter ridge is one, i.e. the clutter is unambiguous in Doppler. Comparing the simulation results for *Example 1* and *Example 2*, it could be seen that the resolution of the radar data image in beam-Doppler domain is improved with the increase of M and N. Therefore, the minimum detectable velocity (MDV) and the accuracy of the target Doppler estimation also increase with M and N. Fortunately, the computational complexity doesn't increase much with M and N since only one space-time snapshot is used and the interference covariance matrix estimation is unnecessary. It could also be

seen from Figure 2.7 and Figure 2.8 that the size of the interference feature block also increases with M and N.

In *Example 3*, with the increase of the platform velocity, the clutter becomes Doppler-ambiguous. It could be seen in Figure 2.9 that the slope of the clutter ridge increases to $\beta = 1.8$ and the clutter spectrum folds over into the observable Doppler space. Since in this example the clutter occupies a larger portion of the Doppler space, it is reasonable to expect that the performance of the proposed BDIFR method degrades.

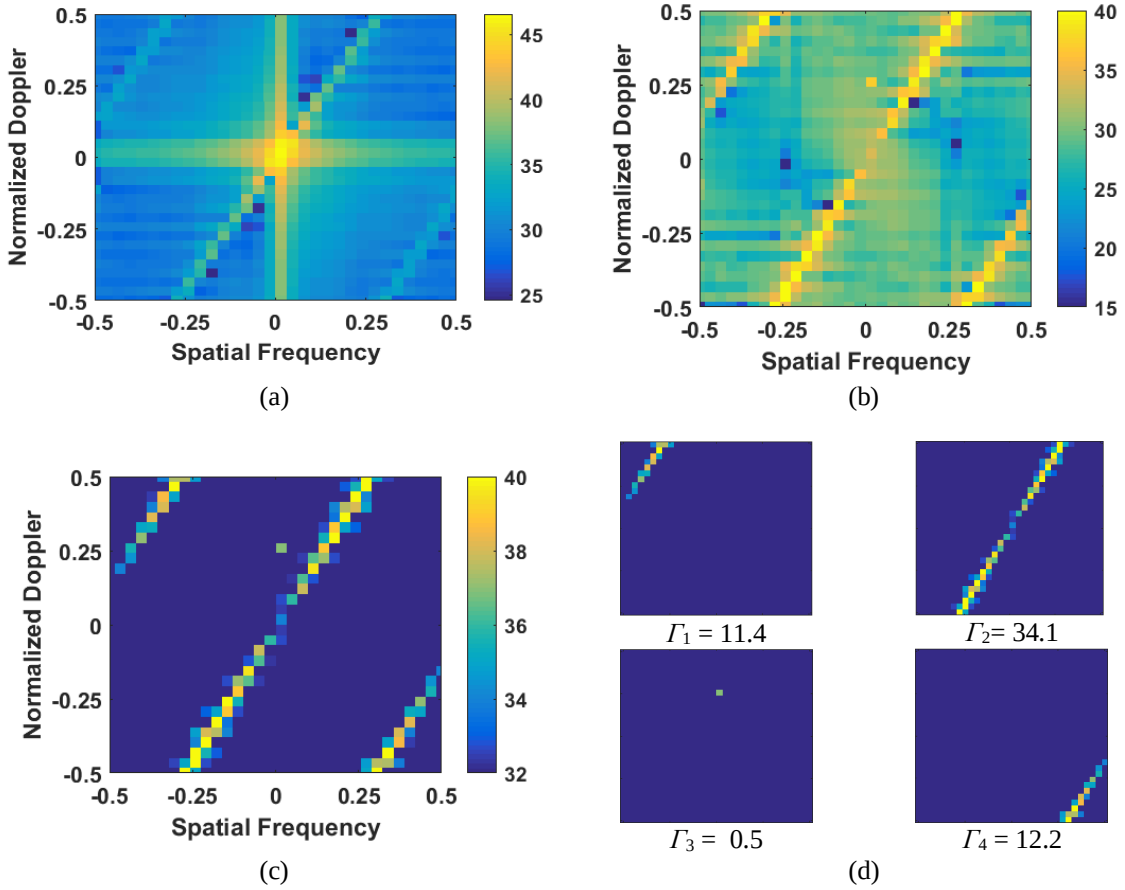

Figure 2.9 BDIFR processing results for Example 3.
(a) Radar data image obtained in beam-Doppler domain via 2D-DFT; (b) MTI filter (three pulse canceller) output; (c) denoised radar data image and (d) feature blocks generated via MBD-RG.

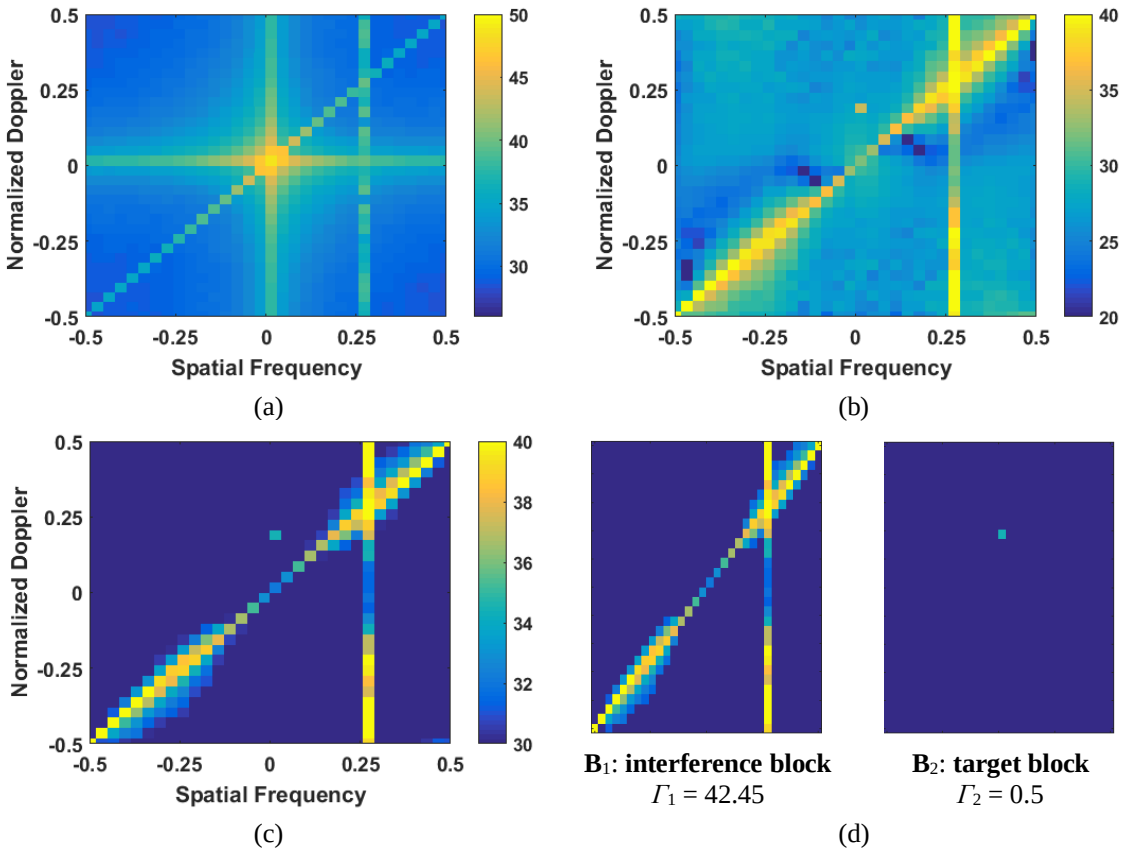

Figure 2.10 BDIFR processing results for Example 4.
(a) Radar data image obtained in beam-Doppler domain via 2D-DFT; (b) MTI filter (three pulse canceller) output; (c) denoised radar data image and (d) feature blocks generated via MBD-RG.

In *Example 4*, a jamming signal with a spatial frequency of 0.25 is taken into consideration in addition to the ground clutter signal. It is interesting to notice that the size of the interference feature block in this example is the same with that of the interference feature block in *Example 2*. The reason is that the block size in the BDIFR algorithm is defined as the maximum distance between two pixels in the feature block instead of the number of pixels in the feature block. Although a vertical line appears at the spatial frequency of 0.25, the maximum distance between the two pixels in the interference feature block is still the distance between the two pixels located at the lower

left corner and the upper right corner. Hence the size of interference feature block in *Example 2* and *Example 4* are the same.

2.5.2. Scenario 2: MV method is used for radar data transformation

Table 2.2 Radar system, interference and target parameters used in Example 5 to Example 8

			Example 5	Example 6	Example 7	Example 8
Radar System Parameters	Number of antenna elements	N	10	16	16	16
	Number of pulses per CPI	M	10	16	16	16
	PRF	f_r	300 Hz	300 Hz	300 Hz	300 Hz
	Wavelength	λ	0.67 m	0.67 m	0.67 m	0.67 m
	Platform height	H	9000 m	9000 m	9000 m	9000 m
	Platform velocity	v_a	50 m/s	50 m/s	100 m/s	50 m/s
Interference Parameters	Clutter range	R_c	13650m	13650m	13650m	13650m
	Clutter velocity spread (rms)	σ_v	0.5 m/s	0.5 m/s	0.5 m/s	0.5 m/s
	Number of clutter patches	N_c	360	360	360	360
	CNR	ξ_c	40 dB	40 dB	40 dB	40 dB
	Azimuth angle of the jammer	θ_j	---	---	---	0.25
	Elevation angle of the jammer	ϕ_j	---	---	---	0
	JNR	ξ_j	---	---	---	30 dB
Target Parameters	Target azimuth angle	ϕ_t	0	0	0	0
	Target elevation angle	θ_t	0.07	0.07	0.07	0.07
	Target spatial frequency	ϑ_t	0	0	0	0
	Target Doppler frequency	f_d	45 Hz	-15 Hz	45 Hz	-15 Hz
	Target normalized Doppler	ϖ_t	0.15	-0.05	0.15	-0.05
	SNR	ξ_t	0 dB	0 dB	0 dB	0 dB

When multiple partially independent measurements are taken, the MV method is used to transform the space-time domain radar data to the beam-Doppler domain. With the assumption that 45 space-time snapshots are available, four examples are given to demonstrate the performance of the proposed BDIFR algorithm in this scenario. The radar system, interference, and target parameters used in these examples are shown in Table 2.2. The BDIFR processing results for *Example 5*, *Example 6*, *Example 7*, and *Example 8* are shown in Figure 2.11, Figure 2.12, Figure 2.13 and Figure 2.14, respectively. Comparing the simulation results for this scenario with those with Scenario 1, it could be seen that when multiple space-time snapshots are available, both the radar

data image resolution and the target detection performance of the proposed BDIFR algorithm increases dramatically. Specifically, point target with a normalized Doppler of -0.05 are successfully detected in both *Example 6* and *Example 8*. In the following, a detailed analyzation of the simulation results for Scenario 2 is presented.

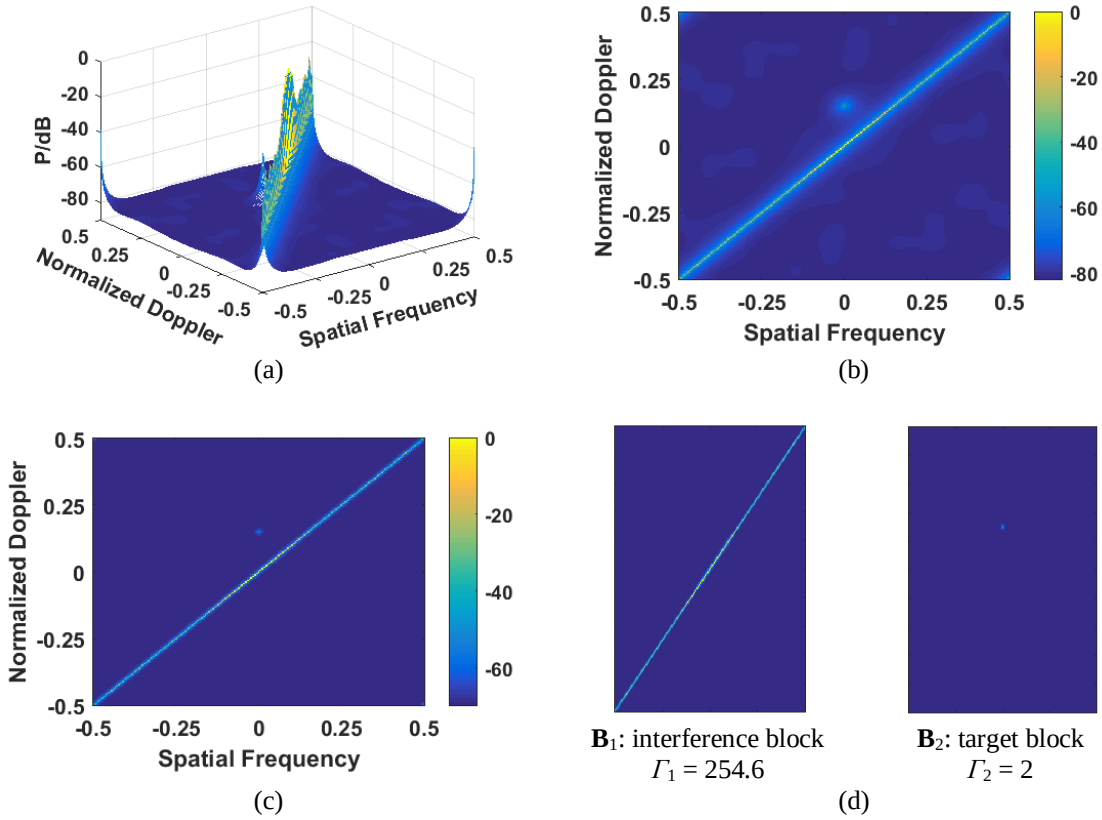

Figure 2.11 BDIFR processing results for Example 5.
(a) 3-D radar data image in beam-Doppler domain; (b) 2-D radar data image in beam-Doppler domain; (c) denoised radar data image and (d) feature blocks generated via MBD-RG.

In *Example 5*, *Example 6* and *Example 7*, the interference signal consists of only ground clutters and the jamming signal doesn't exist. In both *Example 5* and *Example 6*, the slope of the clutter ridge is one, i.e. the clutter is unambiguous in Doppler. Comparing the simulation results for *Example 5* and that for *Example 3*, it could be seen that although only 10 antenna elements and 10 pulses per CPI are used in *Example 5* and 32 antenna elements and 32 pulses per CPI are used in *Example 3*, the image resolution of

the radar data image in *Example 5* is much higher than that in *Example 3*. Comparing the simulation results in Figure 2.11 and Figure 2.12, it could be seen that although the resolution of the radar data image in beam-Doppler domain also increases with M and N, the improvement is less noticeable compared to the improvement in Scenario 1. This is good news: in the MV method, the computational complexity increases linearly with M and N due to the calculation of the covariance matrix.

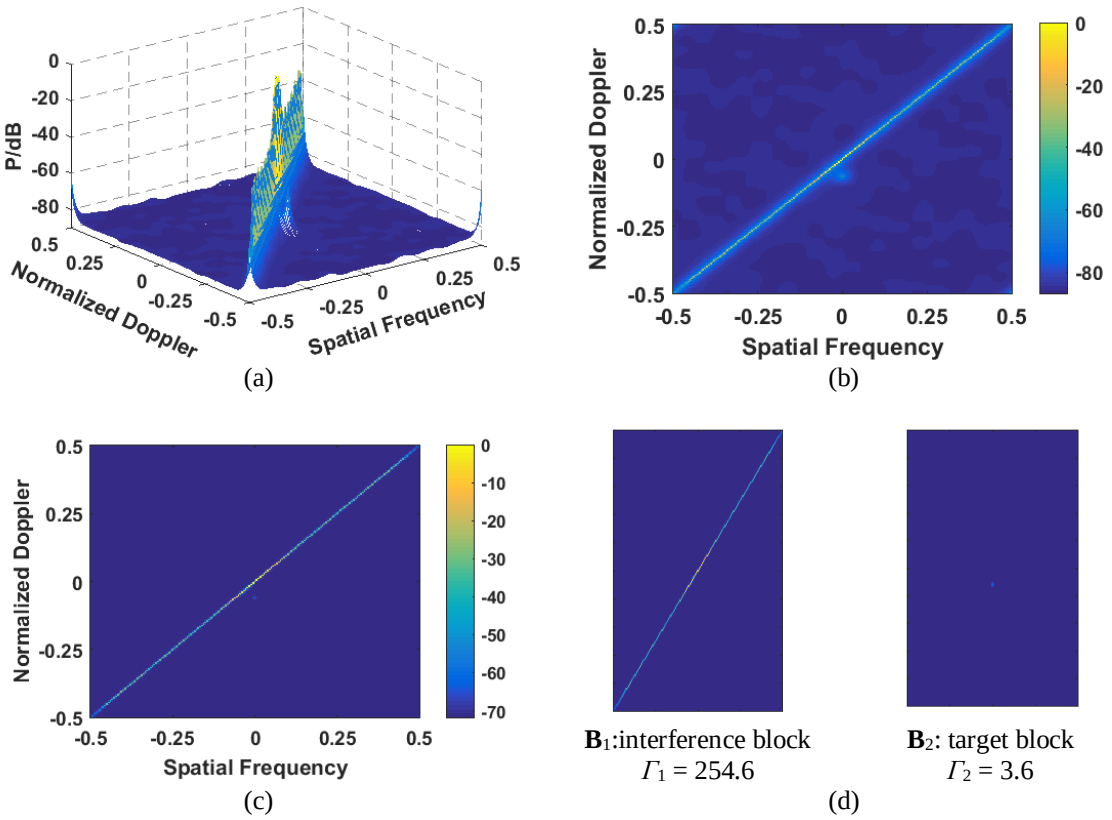

Figure 2.12 BDIFR processing results for Example 6.
(a) 3-D radar data image in beam-Doppler domain; (b) 2-D radar data image in beam-Doppler domain; (c) denoised radar data image and (d) feature blocks generated via MBD-RG.

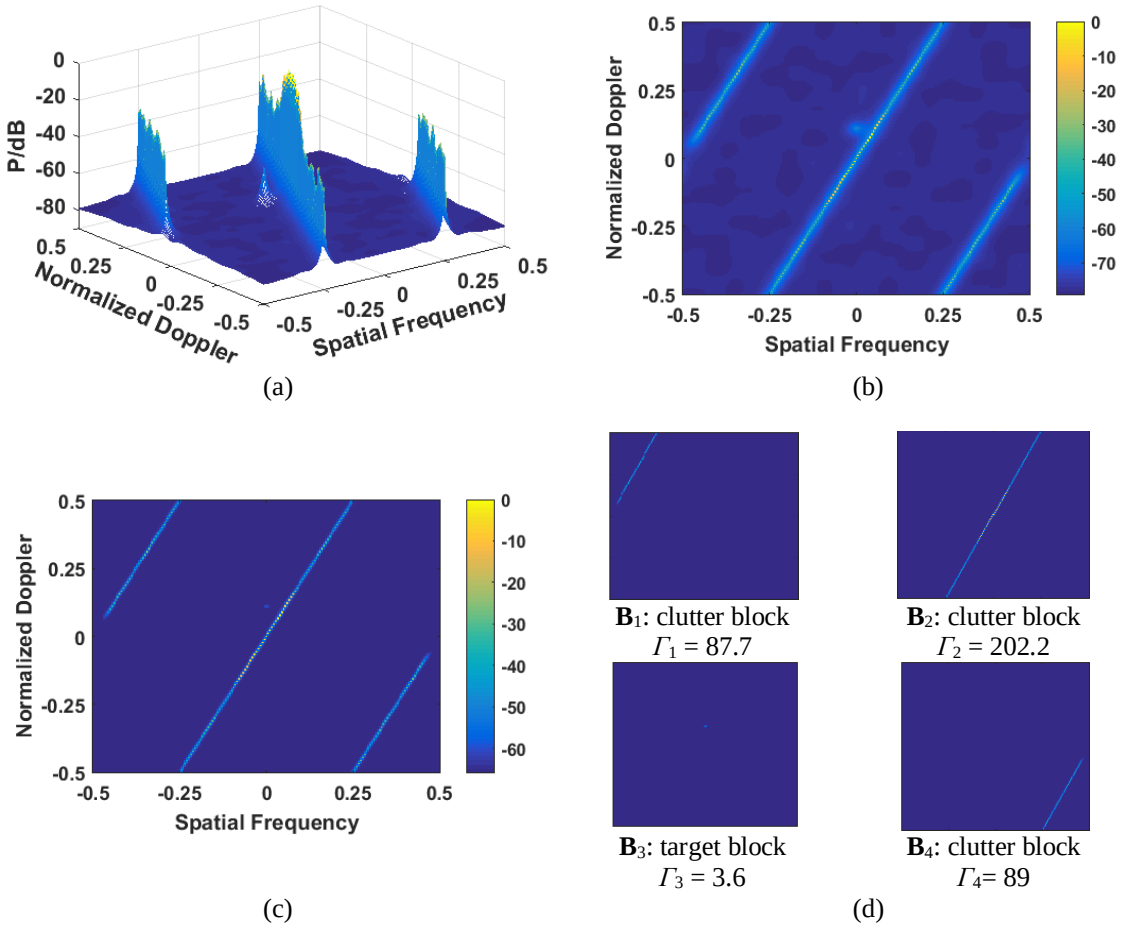

Figure 2.13 BDIFR processing results for Example 7.
(a) 3-D radar data image in beam-Doppler domain; (b) 2-D radar data image in beam-Doppler domain; (c) denoised radar data image and (d) feature blocks generated via MBD-RG.

In *Example 7*, with the increase of the platform velocity, the clutter becomes Doppler-ambiguous. It could be seen in Figure 2.13 that the slope of the clutter ridge increases to $\beta = 2$ and the clutter spectrum also folds over into the observable Doppler space. Although the clutter occupies a larger portion of the Doppler space, the impact of the aliases is less serious than that in Scenario 1 due to the high resolution of the beam-Doppler image. In *Example 8*, a jamming signal with a spatial frequency of 0.25 is taken into consideration in addition to the ground clutter signal. It could be seen from Figure

2.14 that the size of the interference feature block in this example is the same with that of the interference feature block in *Example 6*.

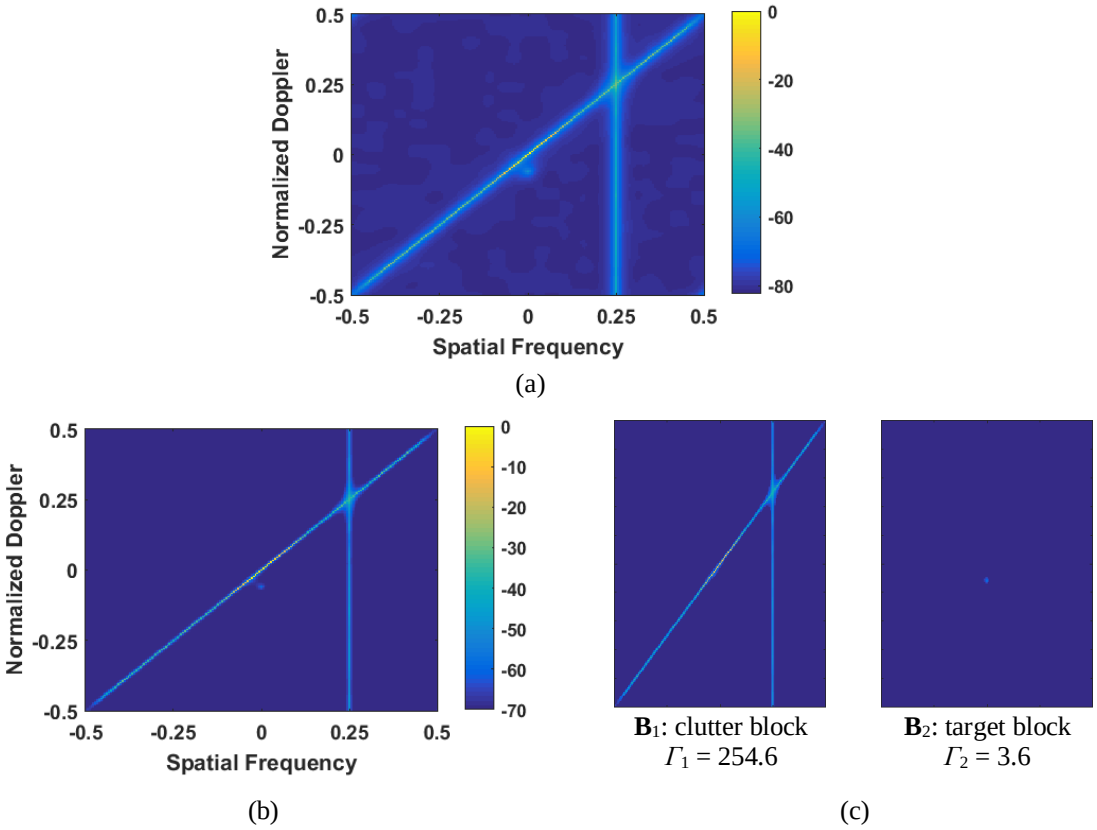

Figure 2.14 BDIFR processing results for Example 8.
(a) 2-D radar data image in beam-Doppler domain; (b) denoised radar data image and (c) feature blocks generated via MBD-RG.

2.6. Performance Evaluation

Since MV method presented in Section 2.5.2 provides high image resolution and better imager feature separation than the 2D-DFT method proposed in Section 2.5.1, the performance of the proposed BDIFR algorithm is evaluated under the assumption that MV method is used for domain transform. The detection probability and false alarm rate in the denoising and MDB-RG processing are investigated separately at first, and then combined together to evaluate the overall performance of BDIFR.

In denoising processing, a false alarm occurs whenever the amplitude of the received noise signal exceeds the denoising threshold T_0 when H_0 is true. Since the envelope of the noise voltage output $\mathcal{N}$ is Rayleigh distributed, the probability density function (PDF) of $\mathcal{N}$ is given by [49-51]

$$f_{\mathcal{N}}(\nu) = \frac{\nu}{\sigma^2} e^{-\frac{\nu^2}{2\sigma^2}} \tag{2.91}$$

where ν is the amplitude of the noise voltage. The false alarm rate, i.e. the probability that $\mathcal{N}$ is greater than the denoising threshold T_0 when H_0 is true, is then obtained as

$$\begin{aligned} P_{fa1} &= \Pr(\mathcal{N} \geq T_0) \\ &= 1 - \int_0^{T_0} \frac{\nu}{\sigma^2} e^{-\frac{\nu^2}{2\sigma^2}} d\nu \\ &= e^{-\frac{T_0^2}{2\sigma^2}} \end{aligned} \tag{2.92}$$

The denoising threshold T_0 is given by

$$T_0 = \sqrt{2\sigma^2 \ln\left(P_{fa1}^{-1}\right)} \tag{2.93}$$

The probability of detection is the probability that the amplitude of a sample of the radar echo signal exceeds the denoising threshold T_0 when H_1 is true. Assume that the SNR per pulse is A_T^2/σ^2, taking into consideration of (2.93), the detection probability for a single radar pulse is given by

$$\begin{aligned} P_{d1} &= \int_{\sqrt{2\sigma^2 \ln\left(P_{fa1}^{-1}\right)}}^{\infty} \frac{r}{\sigma^2} I_0\left(\frac{rA_T}{\sigma^2}\right) e^{-\frac{r^2 + A_T^2}{2\sigma^2}} dr \\ &= Q_M\left[A_T/\sigma, \sqrt{2\sigma^2 \ln(P_{fa1}^{-1})}\right] \end{aligned} \tag{2.94}$$

where I_0 is the zero order Bessel function of first kind and $Q_M(.)$ represents the Marcum's Q-function. Since M pulses are used for coherent processing, the noise power is reduced by a factor of $1/M$, while the desired signal power remains unchanged. When P_{fa1} is small and P_{b1} is large, the detection probability in denoising processing could be approximated by

$$P_{d1} \approx 1 - Q\left(\sqrt{M}\, A_T / \sigma - \sqrt{2\sigma^2 \ln(P_{fa1}^{-1}) / M}\right) \tag{2.95}$$

where $Q(.)$ represents the Q-function given by

$$Q(x) = \int_x^{\infty} \frac{1}{\sqrt{2\pi}} e^{-\frac{\xi^2}{2}} d\xi \tag{2.96}$$

To evaluate the detection probability and false alarm rate in MDB-RG processing, we define the following:

Definition 7 (*Transition area* and *clean area*): If the distance between the target pixel cluster and clutter pixel cluster is less than or equal to Λ, which is a pre-determined threshold for MDB-RG processing, the target falls into a transition area; otherwise, the target lies in clean area.

With the definition above, the target pixel cluster in the transition area will be mischaracterized as part of the clutter pixel cluster, while the target pixel cluster in the clean area will be successfully detected. Thus, the detection performance of BDIFR in MDB-RG processing is determined by the size of the *transition area* and *clean area*. Since moving target signals generally do not overlap with the clutter in the beam-Doppler plane, the detection probability P_{d2} in this process is calculated as:

$$P_{d2} = 1 - \frac{A_{tr}}{A_{cl} + A_{tr}}, \tag{2.97}$$

where A_{tr} and A_{cl} are the size of transition area and clean area, respectively. As shown in the simulation results, the features of the clutter signals in the beam-Doppler plane for the case where the clutter is unambiguous are different from those where the clutter is ambiguous in Doppler. Thus, A_{tr} and A_{cl} are calculated in different ways for the two cases accordingly as:

$$P_{d2} \approx \begin{cases} 1-2\Lambda\sqrt{1+\zeta^2}\Big/\sum_{i=1}^{W}\Gamma_i & 0 \le \zeta \le 1 \\ 1-2\sqrt{2}\Lambda\zeta\Big/\sum_{i=1}^{W}\Gamma_i & \zeta > 1 \end{cases}, \tag{2.98}$$

where W is the total number of feature blocks generated in the MDB-RG process, and ζ is the slope of the clutter ridge and calculated as

$$\zeta = \frac{2v_a}{d_0 f_r}. \tag{2.99}$$

Since the amplitude of the clutter signal is Rayleigh-distributed, some pixels may be clamped in the denoising process. As a result, the clutter pixels which are connected to the clutter ridge form their own feature block. If the formed feature block has a size less than Γ_0, a false alarm happens. But in general, the false alarm rate in region growing processing, i.e. P_{fa2}, is almost zero.

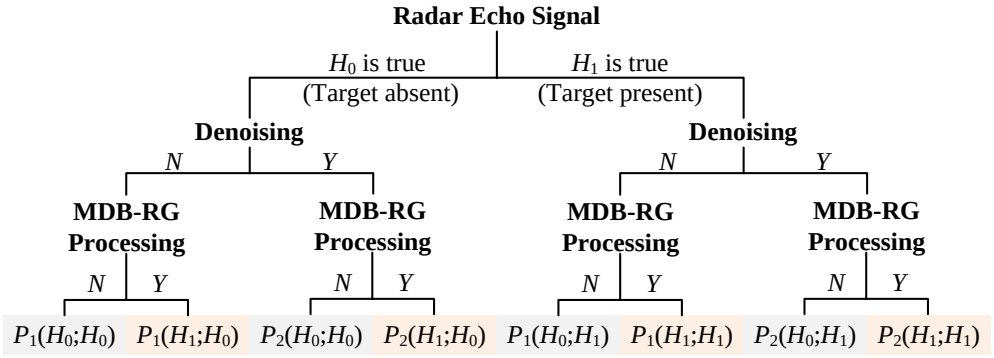

Figure 2.15 Radar target detection tree with denoising and MDB-RG processing.

The possible detection results in the denoising and MDB-RG processing are summarized in Figure 2.15. The notations $P_1(H_i; H_j)$ and $P_2(H_i; H_j)$ represent the probability of declaring H_i when H_j is true in denoising processing and MDB-RG processing, respectively. *Y* and *N* stand for "target detected" and "no target detected", respectively. Since MDB-RG processing follows the denoising process and is assumed to be reliable in the sense that it preserves the pixels which have survived the denoising process and doesn't generate extra new pixels, $P_2(H_1;H_0)$ is approximately equal to P_{fa1} and $P_1(H_1;H_0)$ is approximately 0. According to Figure 2.15, the overall detection probability P_d and false alarm rate P_{fa} are calculated as:

$$P_d = P_1(H_1;H_1) + P_2(H_1;H_1) \approx P_{d1} \times P_{d2}, \tag{2.100}$$

$$P_{fa} = P_1(H_1;H_0) + P_2(H_1;H_0) \approx P_{fa1}. \tag{2.101}$$

Assume that $T_0 = 3.5$ and $\beta = 6$, the false alarm rate vs. detection probability plot is given in Figure 2.16 for *Example 6* and *Example 7* in Section 2.5.2, respectively.

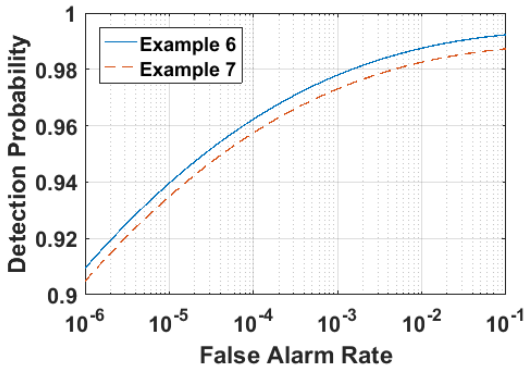

Figure 2.16 Detection probability and false alarm rate of the BDIFR approach for Example 6 and 7.

As expected, the performance of BDIFR is better for the unambiguous clutter scenario, where there is at most one angle where the clutter has the same Doppler as the target. For most cases in airborne radar target detection, the clutter is unambiguous due to

the relatively low velocity of the radar platform. Thus, the detection probability and false alarm rate of the proposed BDIFR algorithm are decent when detecting ground moving targets in inhomogeneous clutter.

For purpose of comparison, the output SINR of the adaptive filter in conventional STAP in homogeneous clutter and inhomogeneous clutter with amplitude heterogeneity and ICM is plotted in Figure 2.17 (a). Radar and clutter parameters for *Example 6* are used for simulations. The clutter is assumed to be the Gamma distributed, and the ratio of the mean of the Gamma distribution to the standard deviation is denoted by mean/std. The rms value for the clutter velocity in the primary unit is selected as σ_v = 0.5 m/s and clutter is assumed to be unambiguous in Doppler. 100 Monte Carlo trials are carried out and the average output SINR is employed. The six cases considered include:

Case 1: Clutter is homogeneous and the covariance matrix is known;

Case 2: mean/std = 2/3, σ_{v2} = 0.4 m/s;

Case 3: mean/std = 1/3, σ_{v2} = 0.3 m/s;

Case 4: mean/std = 1/5, σ_{v2} = 0.2 m/s;

Case 5: mean/std = 1/8, σ_{v2} = 0.1 m/s; and

Case 6: mean/std = 1/10, σ_{v2} = 0.05 m/s.

where σ_{v2} represents the rms velocity of clutter in secondary training data cells. The smaller the difference between σ_v (i.e. 0.5 m/s) and σ_{v2}, the more homogenous the data is; on the other hand, larger mean/std indicates the more homogeneous the clutter amplitudes. For Cases 2- 6, $K = 2MN = 512$ samples are available and used for clutter estimation with the sample matrix inversion (SMI) method.

It is shown in Figure 2.17 (a) that when the normalized target Doppler is -0.05, the output SINR of the adaptive filter is 21.93 dB, 17.43 dB, 15.02 dB, 12.65 dB, 10.68 dB and 9 dB, for the six different cases, respectively. The target detection probabilities versus output SINRs for various false alarm rates are plotted in Figure 2.17 (b). It is found that for a fixed false alarm rate of 10^{-3}, the target detection probabilities are 0.8942 and 0.6554 for Cases 5 and 6, respectively. Therefore, it is proved that the proposed algorithm outperforms conventional STAP in highly inhomogeneous ground clutter environments.

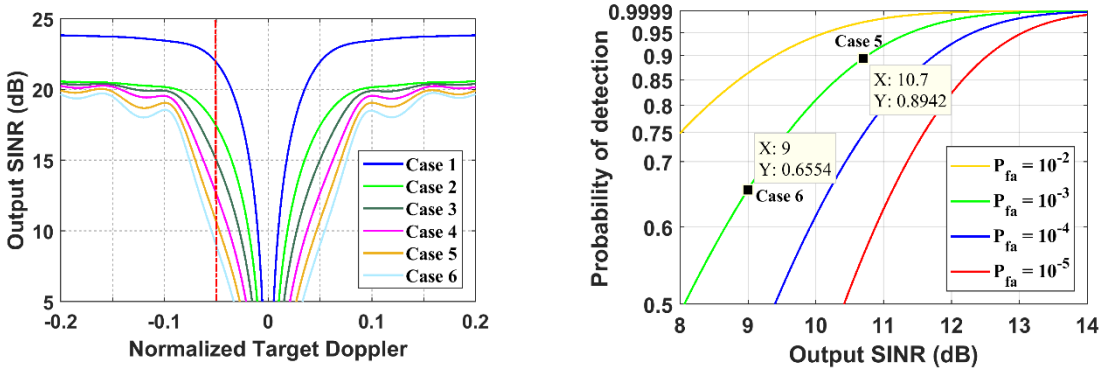

(a) (b)

Figure 2.17 Performance of conventional STAP in inhomogeneous clutter.
(a) Output SINR for different target Doppler. (b) Detection probability vs. false alarm rate.

2.7. Summary of Chapter 2

In this chapter, the BDIFR approach is developed to detect ground moving target in inhomogeneous clutter, where the assumption of independent and identically distributed clutter is not justified and no sufficient secondary data are available for accurate clutter matrix estimation. Through various simulations, it has been demonstrated that BDIFR is effective even in the case where the target and clutter are not widely separated in the beam-Doppler domain. BDIFR is proved to be capable of successfully

detecting target in clutter when the target's velocity is low or Doppler ambiguity appears. The detection probability and false alarm rate of BDIFR in the denoising and MDB-RG processing are investigated in the performance evaluation section. It is shown that the performance of BDIFR is better than that of conventional STAP in inhomogeneous clutter environments.

3. GROUND MOVING TARGET DETECTION FOR AIRBORNE RADAR USING CLUTTER DOPPLER COMPENSATION AND DIGITAL BEAMFORMING

MTI and moving target detection (MTD) have been widely used to detect moving targets in clutter for long-range surface-based surveillance radars [52-55]. However, conventional MTI and MTD processing are not applicable for airborne surveillance radars due to the moving platform effects on the Doppler spectrum [56]. Worse still, airborne radar normally incurs very strong ground clutters: even sidelobe ground clutter that enters radar receiver through antenna sidelobes could be much stronger than the mainlobe target signals, and could lead to a large false alarm rate in target detection if not properly addressed [57]. Moreover, since the Doppler frequency of ground clutters generated from a clutter patch in a range ring is directly proportional to the sinusoidal function of the clutter patch angle measured from the normal direction of the antenna array, the Doppler frequencies of airborne radar clutters are extended to a large frequency range, which makes clutter suppression even more technically challenging [58].

In this chapter, a new approach is introduced to remove ground clutter and to detect ground moving targets by compensating for the non-zero Doppler frequencies of

ground clutter due to the moving platform. The detailed procedures of the proposed ground moving target detection approach are as following.

(a) Transform the radar data from space-time domain to beam-time domain using temporal DFT.

(b) Compensate for the Doppler shift induced in each beam by the moving platform separately based on the real-time known velocity of the aerial platform.

(c) Apply a simple multi-pulse binomial MTI filter to the Doppler-compensated radar data in the beam-time domain.

(d) Transform the radar data from beam-time domain to beam-Doppler domain using temporal DFT and carry out MTD.

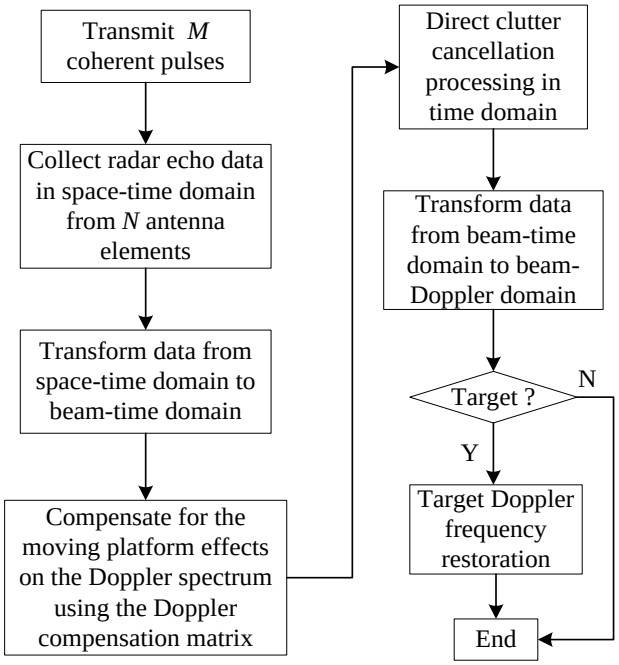

Figure 3.1 Doppler-compensated moving target detection algorithm for airborne radar

The flowchart of the proposed airborne MTI algorithm is shown in Figure 3.1. The advantage of the new airborne radar clutter elimination approach is that since the radar platform velocity is the only information needed for Doppler compensation to

convert airborne clutters to stationary clutters, clutter covariance matrix estimation based on the secondary training data becomes unnecessary.

The rest of this chapter is organized as follows: Doppler compensation in beam-time domain is presented in Section 3.1; clutter cancellation using MTI filter is detailed in Section 3.2; the performance of the proposed approach is evaluated in Section 3.3; the simulation results are provided in Section 3.4; A brief summary of the chapter is given in Section 3.5.

3.1. Doppler Compensation

When the velocity of the platform is zero, the representation of clutter signal in beam-time domain is obtained, by applying 1-D Fourier Transform to the rows of $\mathbf{X}_C$, as

$$F(\mathbf{X}_C)|_{\beta=0}=\begin{bmatrix} \sum_{k=1}^{Nc}\alpha_k\sum_{n=0}^{N-1}e^{j2\pi n\vartheta_k} & \sum_{k=1}^{Nc}\alpha_k\sum_{n=0}^{N-1}e^{j2\pi n\left(\vartheta_k-\frac{1}{N}\right)} & \cdots & \sum_{k=1}^{Nc}\alpha_k\sum_{n=0}^{N-1}e^{j2\pi n\left(\vartheta_k-\frac{N-1}{N}\right)} \\ \sum_{k=1}^{Nc}\alpha_k\sum_{n=1}^{N-1}e^{j2\pi n\vartheta_k} & \sum_{k=1}^{Nc}\alpha_k\sum_{n=0}^{N-1}e^{j2\pi n\left(\vartheta_k-\frac{1}{N}\right)} & \cdots & \sum_{k=1}^{Nc}\alpha_k\sum_{n=0}^{N-1}e^{j2\pi n\left(\vartheta_k-\frac{N-1}{N}\right)} \\ \cdots & \cdots & \cdots & \cdots \\ \sum_{k=1}^{Nc}\alpha_k\sum_{n=1}^{N-1}e^{j2\pi n\vartheta_k} & \sum_{k=1}^{Nc}\alpha_k\sum_{n=0}^{N-1}e^{j2\pi n\left(\vartheta_k-\frac{1}{N}\right)} & \cdots & \sum_{k=1}^{Nc}\alpha_k\sum_{n=0}^{N-1}e^{j2\pi n\left(\vartheta_k-\frac{N-1}{N}\right)} \end{bmatrix} \quad (3.1)$$

Recall that in the case where the platform is moving, the representation of clutter signal in beam-time domain, $F(\mathbf{X}_C)$, is given by (2.38). Therefore, the compensation matrix is given by

$$\mathbf{T}=\frac{F(\mathbf{X}_C)|_{\beta=0}}{F(\mathbf{X}_C)}. \quad (3.2)$$

The (m, n)-th element of $\mathbf{T}$ is given by

$$\mathbf{T}(m,n)=\frac{\sum_{k=1}^{Nc}\alpha_k\dfrac{1-e^{j2\pi N\left(\vartheta_k-\frac{n}{N}\right)}}{1-e^{j2\pi\left(\vartheta_k-\frac{1}{N}\right)}}}{\sum_{k=1}^{Nc}\alpha_k e^{j2\pi m\beta\vartheta_k}\dfrac{1-e^{j2\pi N\left(\vartheta_k-\frac{n}{N}\right)}}{1-e^{j2\pi\left(\vartheta_k-\frac{n}{N}\right)}}}. \tag{3.3}$$

Assume that $d_0=0.5\lambda$ and the elevation angle ϕ_r = 0°, (3.3) could be simplified as

$$\mathbf{T}(m,n)=\frac{\sum_{k=1}^{Nc}\alpha_k e^{j\pi(N-1)\vartheta_k}\dfrac{\sin\left[N\pi\left(\vartheta_k-\frac{n}{N}\right)\right]}{\sin\left[\pi\left(\vartheta_k-\frac{n}{N}\right)\right]}}{\sum_{k=1}^{Nc}\alpha_k e^{j\pi(2m\beta+N-1)\vartheta_k}\dfrac{\sin\left[N\pi\left(\vartheta_k-\frac{n}{N}\right)\right]}{\sin\left[\pi\left(\vartheta_k-\frac{n}{N}\right)\right]}}. \tag{3.4}$$

When the clutter is homogeneous, the compensation matrix in (3.4) could be approximated as

$$\mathbf{T}(m,n)=\frac{\sum_{k=1}^{Nc}G_k g_k e^{j\pi(N-1)\vartheta_k}\dfrac{\sin\left[N\pi\left(\vartheta_k-\frac{n}{N}\right)\right]}{\sin\left[\pi\left(\vartheta_k-\frac{n}{N}\right)\right]}}{\sum_{k=1}^{Nc}G_k g_k e^{j\pi(2m\beta+N-1)\vartheta_k}\dfrac{\sin\left[N\pi\left(\vartheta_k-\frac{n}{N}\right)\right]}{\sin\left[\pi\left(\vartheta_k-\frac{n}{N}\right)\right]}} \tag{3.5}$$

where G_k is expressed as

$$G_k=\left|\frac{\sin\left[N\pi d\left(\sin\theta_0-\sin\theta_{r,k}\right)/\lambda\right]}{\sin\left[\pi d\left(\sin\theta_0-\sin\theta_{r,k}\right)/\lambda\right]}\right|,\qquad -180^\circ\le\theta_{r,k}\le 180^\circ \tag{3.6}$$

and g_k is expressed as

$$g_k = \begin{cases} \left|\cos\theta_{r,k}\right| & \left|\theta_{r,k}\right| \le 90^\circ \\ \left|b_e \cos\theta_{r,k}\right| & 90^\circ \le \left|\theta_{r,k}\right| \le 180^\circ \end{cases} \tag{3.7}$$

where b_e is the backlobe level. By using the Doppler compensation matrix in (3.5), the moving platform effects on the Doppler spectrum would be compensated, so that the traditional MTI processing techniques that are commonly used in surface-based radar could be used subsequently to suppress clutter signals.

3.2. Clutter Cancellation Filtering

With the moving platform effects on the Doppler spectrum successfully compensated, the clutters become near-stationary and are then cancelled via conventional digital MTI radar filter processing. As is mentioned briefly in Section 2.2, higher-order MTI filters have better amplitude responses than lower-order MTI filters. However, as a trade-off, the detection of slow-moving target becomes difficult when higher-order MTI filters are used. Assume that the antenna array transmits a coherent burst of pulses given by

$$\tilde{s}(t) = a_t \sum_{m=0}^{M-1} u_p(t - mT)\cos(2\pi f_0 t) \tag{3.8}$$

where f_0 is the radar operating frequency, T is the pulse repetition interval (PRI), and u_p is the complex envelope of a single pulse defined as

$$u_p(t) = \begin{cases} 1 & 0 \le t < mT \\ 0 & \text{Otherwise} \end{cases}. \tag{3.9}$$

For a target at initial range of R_0 and radial velocity v, the time delay is

$$\tau_R = \frac{2(R_0 - vt)}{c} \tag{3.10}$$

where c is the speed of light. The reflected sinusoid is then

$$\cos\left(2\pi f_0 (t - \tau_R)\right) = \cos\left(2\pi f_0 t + \frac{4\pi f_0 v t}{c} - \frac{4\pi f_0 R_0 t}{c}\right). \tag{3.11}$$

The two pulse canceller amplitude output due to the target is

$$\begin{aligned} &\cos\left[2\pi f_0 (t - \tau_R)\right] - \cos\left[2\pi f_0 (t - \tau_R - T)\right] \\ &= -\sqrt{2}\sin\left[\pi\left(f_0 + \frac{2f_0 v}{c}\right)T\right]\sin\left[2\pi\left(f_0 + \frac{2f_0 v}{c}\right)t - \frac{4\pi f_0 R_0 t}{c} - \pi\left(f_0 + \frac{2f_0 v}{c}\right)T\right]. \end{aligned} \tag{3.12}$$

Since the carrier frequency and PRF are harmonically related, $f_0 T$ is an integer, and the power of the two pulse canceller circuit is

$$E_2 = 2\sin^2\left(\frac{2\pi f_0 v}{c} T\right) = 2\sin^2\left(\pi f_{d,t} T\right). \tag{3.13}$$

Similarly, the power of the three pulse canceller circuit is

$$E_3 = \frac{\sin^4\left(2\pi f_{d,t} T\right)}{6}. \tag{3.14}$$

When $f_{d,t} = 0.1 f_r$, the target gain is -7 dB and -16 dB for two pulse and three pulse canceller, respectively. At the same time, compared with two pulse canceller, fewer pules are available for coherent integration for three pulse canceller. Despite of these disadvantages, in next section, the performance of the proposed method will be evaluated based on the assumption that a double delay line canceller is implemented.

3.3. Performance Evaluation

In this section, the performance of the proposed airborne MTI algorithm is evaluated based on the MTI improvement factor (IF), the minimum detectable velocity (MDV), and the usable Doppler space fraction (UDSF).

3.3.1. The MTI IF of the proposed algorithm

According to [59], The MTI IF is defined as the signal to clutter power ratio at the output of the clutter filter divided by the signal-to-clutter power ratio at the input to the clutter filter, averaged uniformly over all target radial velocities of interest. The overall improvement factor I_{total} of the proposed airborne MTI algorithm is expressed as

$$\frac{1}{I_{total}} = \frac{1}{I_0} + \frac{1}{I_1} + \frac{1}{I_2} \tag{3.15}$$

where I_0 is the ideal MTI IF, I_1 is the reduced MTI IF due to imperfect motion compensation, and I_2 is the reduced MTI IF due to clutter's frequency offset. The process of obtaining I_0, I_1, and I_2 is detailed in the following.

(a) Ideal MTI IF

The three pulse canceller impulse response is given by

$$h(t) = \delta(t) - 2\delta(t-T) + \delta(t-2T) \tag{3.16}$$

where $\delta(.)$ is the delta function. It follows that the Fourier Transform of $h(t)$ is expressed as

$$H(f) = 1 - 2e^{-j2\pi fT} + e^{-j4\pi fT}. \tag{3.17}$$

The clutter power at the output of an MTI is given by

$$C_o = \int_{-\infty}^{\infty} W(f)|H(f)|^2 df \tag{3.18}$$

where $W(f)$ is the Gaussian-shaped clutter power spectrum. According to [53], $W(f)$ could be further expressed as

$$W(f) = \frac{P_c}{\sqrt{2\pi}\sigma_r} e^{-\frac{f^2}{2\sigma_r^2}} . \tag{3.19}$$

P_c and σ_r in (3.19) are the clutter power and the clutter root mean square (rms) frequency, respectively. In this chapter, since the primary focus is on the moving platform effects on the Doppler spectrum, it is assumed that

$$\sigma_r^2 = \sigma_{pm}^2 \tag{3.20}$$

where σ_{pm}^2 is the variance due to the platform motion. By assuming $f << f_r$, which is valid since the clutter power is more significant for small *f*, and plugging (3.17) and (3.19) in to (3.18), it follows that

$$\begin{aligned} C_o &\approx \frac{16P_c\pi^4}{f_r^4} \int_{-\infty}^{\infty} \frac{1}{\sqrt{2\pi\sigma_{pm}^2}} e^{-\frac{f^2}{2\sigma_{pm}^2}} f^4 df \\ &= \frac{4P_c\pi^2\sigma_{pm}^2}{3} \end{aligned} . \tag{3.21}$$

The ideal MTI improvement factor using three pulse canceller is then

$$\begin{aligned} I_0 &= \frac{P_c}{C_o}\left[T\int_{f_r/2}^{f_r/2}|H(f)|^2 df\right] \\ &= \frac{P_c}{C_o}\left[T\int_{f_r/2}^{f_r/2}\left(2\cos(4\pi fT) - 8\cos(2\pi fT) + 6\right)df\right]. \\ &= \frac{1}{8\left(\pi\sigma_{pm}T\right)^4} \end{aligned} \tag{3.22}$$

(b) Reduced MTI IF due to Imperfect Motion Compensation

The mean frequency of the ground clutter patch spectrum due to platform motion is

$$f_{pm} = \frac{2\sigma_{pm}}{\lambda} = \frac{2v_a}{\lambda}\sin\theta_{r,k}\cos\phi_r . \tag{3.23}$$

The motion compensation matrix in (3.5) is not perfect since the adjustment frequency Δf (i.e. the frequency error) depends on the azimuth and depression angle. When $\theta_{r,k} \neq 0^\circ$, the spectral width due to the antenna's azimuth beamwidth, θ_B, is given by

$$\Delta f_{nz} = \frac{2v_a}{\lambda}\cos\phi_r\left[\sin\left(\theta_{r,k} - \frac{\theta_B}{2}\right) - \sin\left(\theta_{r,k} + \frac{\theta_B}{2}\right)\right]. \tag{3.24}$$

Since θ_B is small, (3.24) could be approximated as

$$\Delta f_{nz} \approx \frac{2v_a}{\lambda}\theta_B \sin\theta_{r,k}\cos\phi_r . \tag{3.25}$$

And the spread at $\theta_{r,k} = 0^\circ$ is

$$\Delta f_z = \frac{2v_a}{\lambda}\cos\phi_r\left[1 - \cos\left(\frac{\theta_B}{2}\right)\right] = \frac{v_a\theta_B^2\cos\phi_r}{4\lambda}. \tag{3.26}$$

The two cases for $\theta_{r,k} \neq 0^\circ$ and $\theta_{r,k} = 0^\circ$ are then combined as

$$\Delta f = \Delta f_z + \Delta f_{nz} = \frac{2v_a}{\lambda}\left(\theta_B\cos\phi_r\sin\theta_{r,k} + \frac{\theta_B^2\cos\phi_r\sin\theta_{r,k}}{8}\right). \tag{3.27}$$

Since only the mean frequency of the ground clutter patch spectrum due to platform motion in (3.23) is taken into consideration in the Doppler compensation process and the adjustment frequency in (3.27) is ignored, the imperfect motion compensation matrix in

(3.5) couldn't compensate for the moving platform effects on the Doppler spectrum perfectly, and the MTI IF is limited by

$$I_1 = \frac{\lambda^4}{6.313\left(4\pi v_a \sigma_{pm} \theta_B \sin\theta_{r,k}\right)^4}. \tag{3.28}$$

(c) Reduced IF due to Clutter's Frequency Offset

The MTI IF is also limited by the clutter's frequency offset f_{off} after motion compensation**.** Taking into consideration of the clutter's frequency offset, the input clutter power is given by

$$P_{ci} = \frac{1}{\sqrt{2\pi\sigma_f^2}} \int_0^{f_r} \left(e^A + e^B\right) df \tag{3.29}$$

where *A* and *B* are given by:

$$A = -\frac{\left(f - f_{off}\right)^2}{2\sigma_f^2},\ B = -\frac{\left(f - f_r - f_{off}\right)^2}{2\sigma_f^2}. \tag{3.30}$$

The output power from the MTI canceler is given by:

$$P_{co} = \frac{1}{\sqrt{2\pi\sigma_f^2}} \int_0^{f_r} 2\left(e^A + e^B\right) \sin^4\left(\frac{\pi f}{f_r}\right) df\ . \tag{3.31}$$

The improvement factor due to f_{off} is then:

$$I_2 = \frac{P_{ci}}{P_{co}} \left[T \int_0^{f_r} 2\sin^4\left(\frac{\pi f}{f_r}\right) df \right]. \tag{3.32}$$

The improvement factor as a function of the velocity offset f_{off} for three pulse canceller is shown in Figure 3.2.

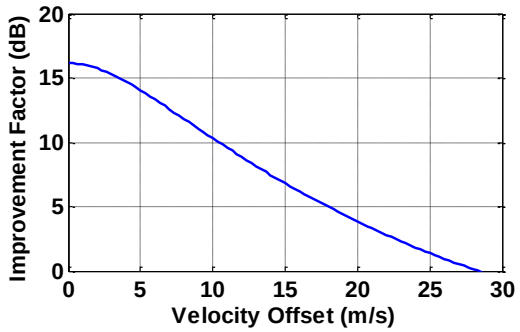

Figure 3.2 Reduced MTI IF due to clutter's frequency offset

3.3.2. The MDV of the proposed algorithm

One of the practical performance metrics for radar systems that are designed to remove clutter is the minimum target velocity that can be detected after clutter cancellation. In fact, targets are subject to removal by the clutter rejection process when their velocity approaches that of the clutter. Thus, the velocity relative to clutter below which the target would be attenuated by the clutter rejection process to an extent that can no longer be detected is called the MDV [60]. In the proposed algorithm, since the output of the three pulse canceller is transformed from beam-time domain into beam-Doppler domain using temporal DFT to carry out MDT, the minimum detectable target Doppler is determined by the resolution of the beam-Doppler image: if the target is placed one pixel off the horizontal rotated clutter ridge in the beam-Doppler plot, it can be detected; otherwise, the target would be eliminated together with the clutter signals. Recall that the target Doppler frequency, f_d, and the target relative velocity to radar, v_r, are related by

$$f_d = \frac{2v_r}{\lambda}. \tag{3.33}$$

It follows that the MDV is given by:

$$v_{\min} = \pm\frac{\lambda}{2} f_{\min} = \pm\frac{\lambda}{2}\frac{f_r}{M-2} \tag{3.34}$$

where $f_{\min}$ is the minimum detectable target Doppler frequency.

3.3.3. The USDF of the proposed algorithm

The percentage of Doppler space that is practically used in terms of targets being detectable is called UDSF. In fact, this fraction depends on the level of tolerable signal to interference plus noise (*SINR*) loss [60]. Thus, UDSF is defined as:

$$UDSF(L) = 1 - P_r(SINR_{Loss} < L) \tag{3.35}$$

where $P_r(SINR_{Loss} < L)$ is the probability that $SINR_{Loss} < L$ and L is commonly assumed to be -5 dB. The usable Doppler frequency in the proposed approach depends not only on the platform velocity, which induces clutter spread, but also on the MTI filter used to remove clutter. Moreover, it is well known that by increasing the number of antenna elements and the number of coherent pulses used in processing, the resolution of the beam-Doppler image would be improved and the performance degradation due to clutter leakage into neighboring Beam Doppler cells would be minimized. Specifically, the UDSF of the proposed algorithm is expressed as

$$UDSF = \left(1 - \frac{2}{M-2}\right) \times 100\% \,. \tag{3.36}$$

3.4. Simulation Results

To validate the proposed airborne MTI algorithm, simulation is carried out by assuming an airborne radar with uniform linear transmit antenna array performing moving target detection using the proposed clutter compensation approach. The

parameters of the airborne radar used in the simulation are listed in Table 3.1. Two different ground moving targets (Targets *A* and *B*) are included in two sets of simulated radar echo data, respectively, to assess the detection performance of the proposed algorithm in two examples. The properties of these targets are provided in Table 3.2. In Example, 1, Target A is injected into the scene in a way that it could easily be detected from clutter because of its high Doppler frequency compared to the clutter. In Example 2, the proposed airborne MTI algorithm is used to detect the slow-moving target B.

Table 3.1 Airborne radar system and clutter parameters

Symbol	Name	Value
f_0	Carrier Frequency	450 MHz
v_a	Platform velocity	50 m/s
H	Platform height	9000 m
f_r	Pulse repetition frequency	300 Hz
T_p	Pulse width	200 μs
P_t	Peak transmit power	200 kW
M	Number of pulses in a CPI	16/32 (Example 1/2)
N	Number of antenna elements	16/32 (Example 1/2)
d	Elements spacing	λ/2
G_t	Transmit gain	22 dB
R_r	Clutter range	130000 m
CNR	Clutter-to-noise ratio	40 dB
N_0	Noise figure	3 dB
L_s	System loss	4 dB

Table 3.2 Targets properties

	Target A	Target B
Target azimuth angle (ϕ_0)	0˚	0˚
Target elevation angle (θ_0)	0˚	0˚
Target Doppler frequency (f_d)	-75 Hz	20 Hz
SNR (per element per pulse)	0 dB	0 dB

3.4.1. Example 1: fast-moving target

The beam-Doppler plot (N = 16, M = 16) for the radar echo data containing clutter, noise and Target A is shown in Figure 3.3, where θ is the azimuth angle. It is obtained by applying 2-D DFT directly to the radar data in space-time domain, with no

clutter suppression or denoising processing applied. The clutter removal result using 3-pulse MTI canceller without Doppler compensation is shown in Figure 3.4. It could be seen clearly that the clutter ridge with slope $\beta = 1$ spans the whole Doppler space, and the target is invisible. Therefore, it is demonstrated that conventional MTI processing techniques are ineffective in dealing with the ground clutter for airborne radar due to the effects of moving platform on the Doppler spectrum.

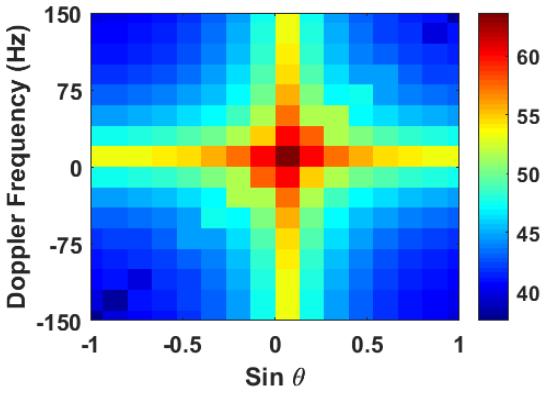

Figure 3.3 Radar echo data in beam-Doppler domain (Example 1)

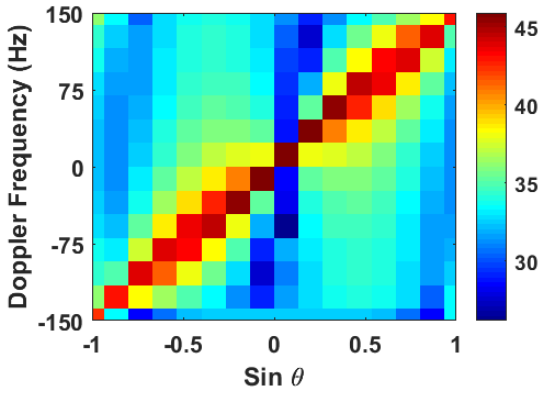

Figure 3.4 Clutter removal result using MTI filter without Doppler compensation (Example 1).

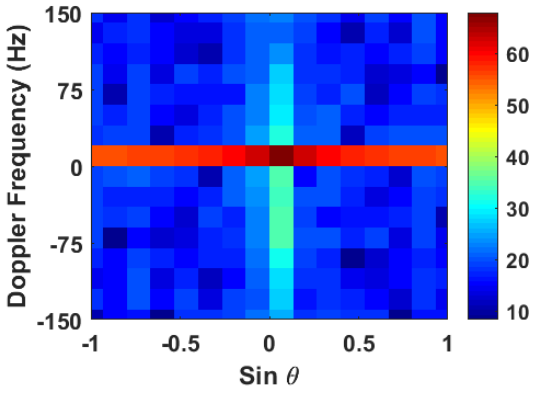

(a)

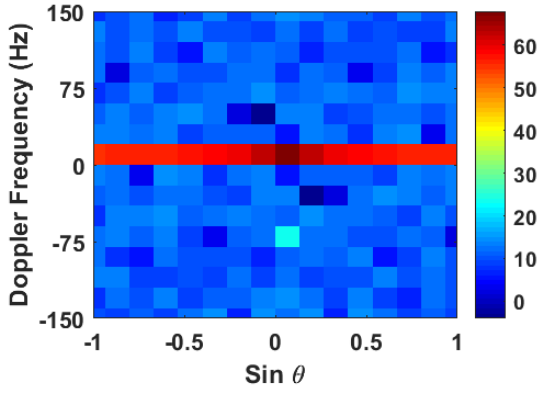

(b)

Figure 3.5 Doppler compensation result for Example 1.
(a) Doppler compenstaion matrix in (3.5) is used; (b) perfect Doppler compensation is assumed.

The Doppler compensation result by using Doppler compensation matrix in (3.5) is plotted in Figure 3.5 (a). For comparison reason, the ideal Doppler compensation result

is plotted in Figure 3.5 (b) by assuming zero platform velocity. It could be seen that although the Doppler compensation matrix given in (3.5) couldn't compensate for the motion effects on the Doppler spectrum in the mainlobe direction perfectly, the Doppler frequencies of the ground clutter in sidelobe directions are shifted to be zero.

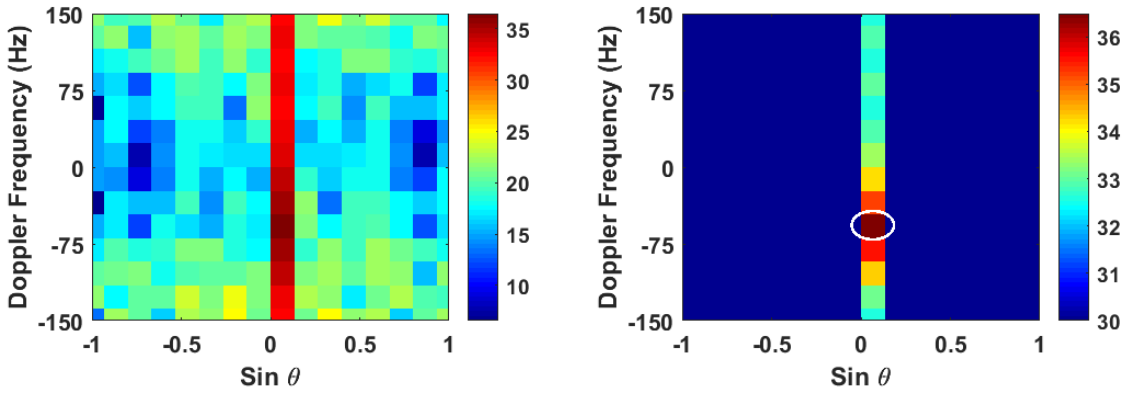

(a) (b)

Figure 3.6 Clutter removal result for Example 1 when the moving platform effects are compensated using the Doppler compensation matrix in (3.5).
(a) Before denoisng processing; (b) after denoising processing.

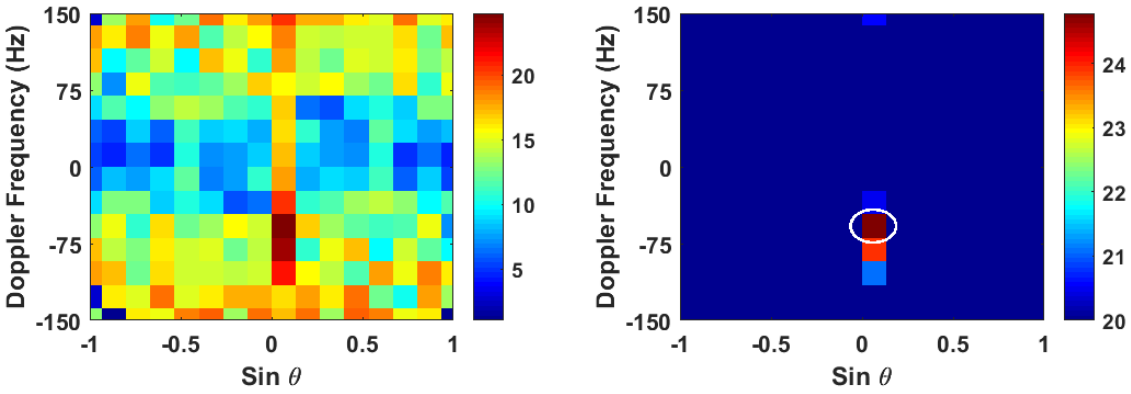

(a) (b)

Figure 3.7 Clutter removal result for Example 1 when moving platform effects are compensated perfectly.
(a) Before denoisng processing; (b) after denoising processing.

The clutter removal results using 3-pulse MTI canceller when the effects of moving platform effects on the Doppler spectrum are partially compensated using the Doppler compensation matrix in (3.5) are plotted in Figure 3.6. It could be seen in Figure 3.6 (b) that after denoising processing, although there are clutter residues remaining in

the mainlobe direction, the target signal becomes clearly visible. The ideal clutter removal results using 3-pulse MTI canceller when the effects of moving platform effects are compensated perfectly are plotted in Figure 3.7. Comparing Figure 3.7 (b) and Figure 3.6 (b), it could be seen although the proposed compensation matrix in (3.5) is not perfect, target azimuth angle and Doppler frequency are indicated correctly by using the proposed airborne MTI algorithm.

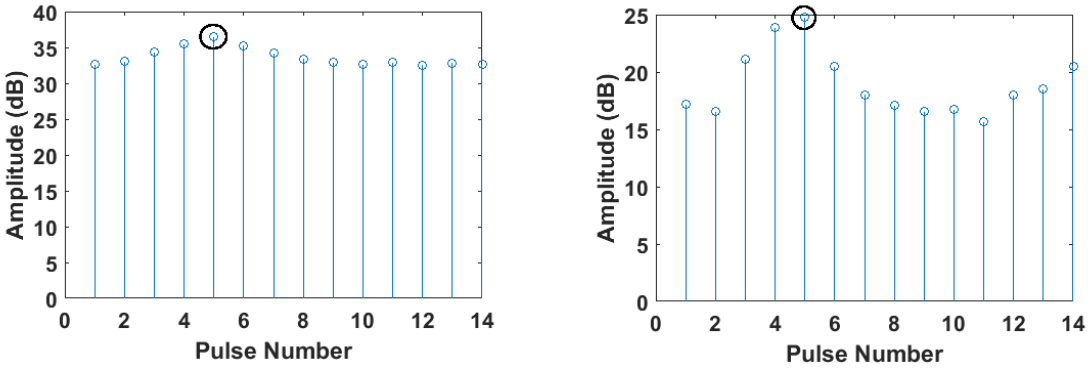

(a) (b)

Figure 3.8 The output signal of the 3-pulse MTI canceller in the mainlobe direction (Example 1). (a) Doppler compenstaion matrix given in (3.5) is used; (b) ideal Doppler compensation is assumed.

The output signal of the 3-pulse MTI canceller in the mainlobe direction is potted in Figure 3.8. Figure 3.8 (a) is obtained by using the Doppler compensation matrix given in (3.5), and Figure 3.8 is obtained by assuming ideal Doppler compensation. The target Doppler is estimated from the pulse number P_N as

$$f_{d,t} \in \left[-\frac{f_r}{2} + (P_N - 1.5) \times (\frac{f_r}{M-2}), -\frac{f_r}{2} + (P_N - 0.5) \times (\frac{f_r}{M-2}) \right] \tag{3.37}$$

Since the maximum value is obtained at the 5th pulse, the target Doppler frequency is estimated as $f_{d,t} \in$ [-75 Hz, -54 Hz]. It could be seen that the resolution of the Doppler estimation in this example is relatively low due to the small M. In next example, it will be

demonstrated that the accuracy of the Doppler estimation will be greatly improved by increasing *M*.

3.4.2. Example 2: slow-moving target

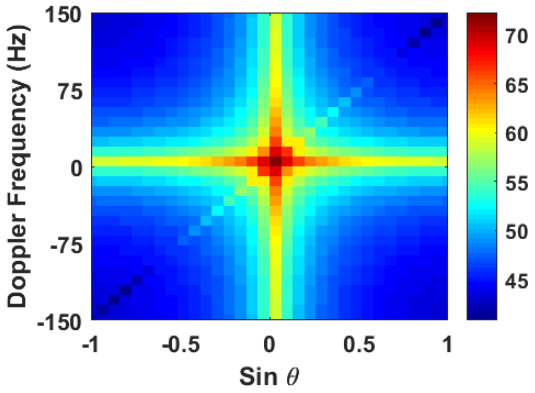

Figure 3.9 Radar echo data in beam-Doppler domain (Example 2).

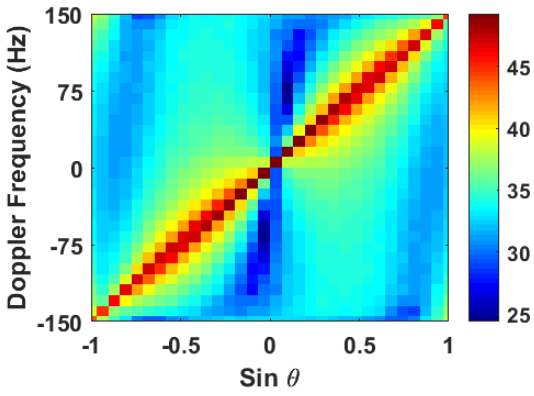

Figure 3.10 Clutter removal result using MTI filter without Doppler compensation (Example 2).

To further validate the proposed ground moving target detection and clutter removal approach, in this example, the proposed airborne MTI algorithm is used to detect a slow-moving target, *Target B*. Since the Doppler frequency of Target B is much lower than A, *M* is increased to 32 to improve the performance. The 2-D DFT result of the radar echo data containing clutter, noise and Target B is shown in Figure 3.9. The clutter removal result using 3-pulse MTI canceller without Doppler compensation is shown in Figure 3.10. It could be seen clearly that although the clutter ridge becomes thinner compared to Figure 3.4 due to the higher image resolution of the beam-Doppler induced by larger *M*, the target is still invisible.

The Doppler compensation results by suing the Doppler compensation matrix given in (3.5) and by assuming perfect Doppler compensation are plotted in Figure 3.11 (a) and (b), respectively. Comparing Figure 3.11 (a) with Figure 3.11 (b), it could be seen that due to the imperfectness of the compensation matrix given in (3.5), the target signal

is “buried” in the Doppler-shifted clutter signals in the mainlobe direction prior to the MTI filter processing.

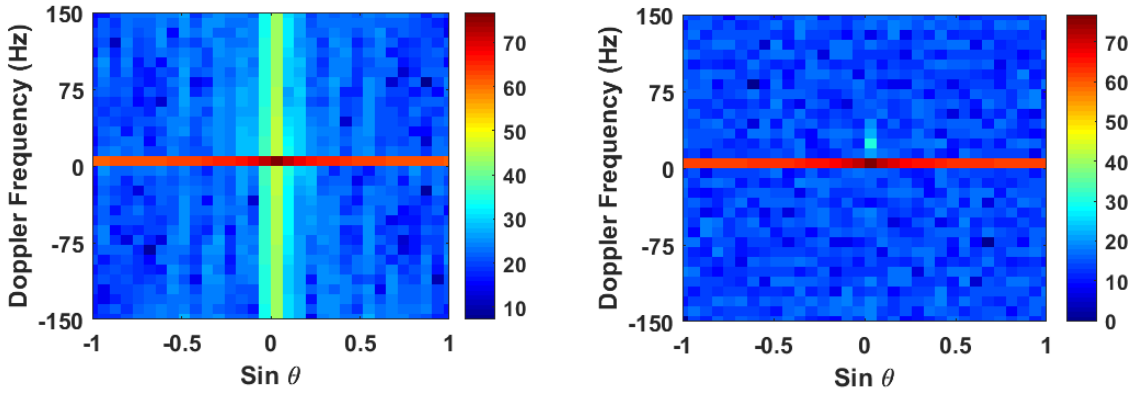

(a) (b)

Figure 3.11 Doppler compensation result for Example 2.
(a) Doppler compensation matrix in (3.5) is used; (b) perfect Doppler compensation is assumed.

The clutter removal results using 3-pulse MTI canceller when the effects of moving platform effects on the Doppler spectrum are compensated using the Doppler compensation matrix in (3.5) with/without denoising processing are plotted in Figure 3.12 (a) and (b), respectively, and the target signal is clearly visible in Figure 3.12 (b). The clutter removal result using 3-pulse MTI canceller under the assumption of perfect motion compensation with/without denoising processing are plotted in Figure 3.13 (a) and (b), respectively. Comparing Figure 3.12 and Figure 3.13, it could be seen that a near-perfect sidelobe clutter elimination performance is achieved using the proposed airborne MTI algorithm, although the mainlobe clutter elimination performance is limited by the imperfectness of the compensation matrix given in (3.5).

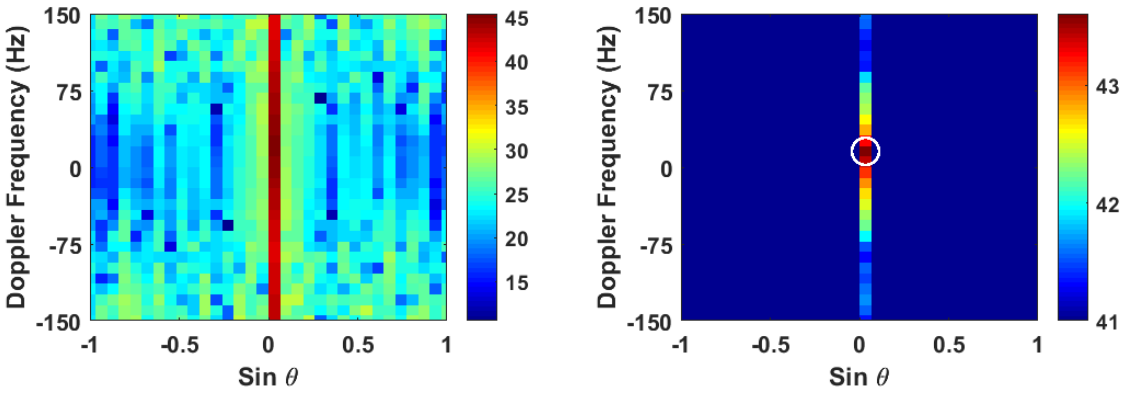

(a) (b)

Figure 3.12 Clutter removal result for Example 2 when the moving platform effects are compensated using the Doppler compensation matrix in (3.5).
(a) Before denoisng processing; (b) after denoising processing.

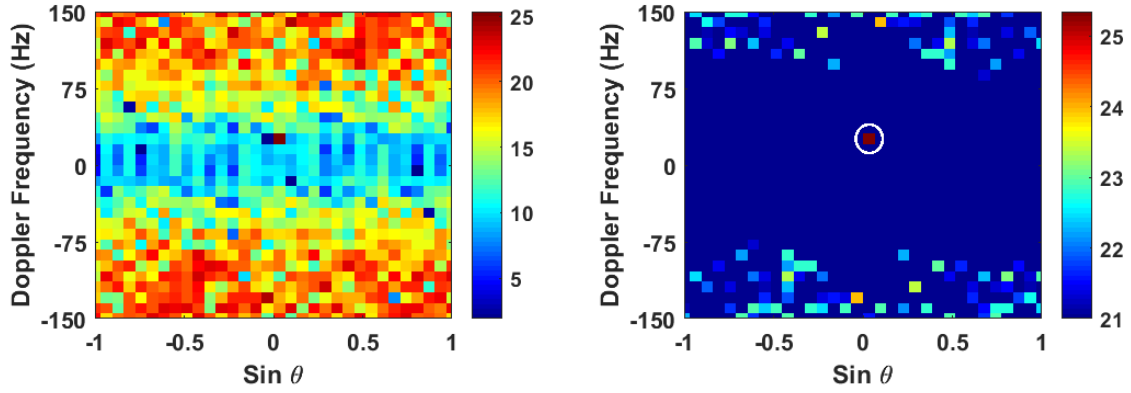

(a) (b)

Figure 3.13 Clutter removal result for Example 2 when moving platform effects are compensated perfectly.
(a) Before denoisng processing; (b) after denoising processing.

Finally, the output signal of the 3-pulse MTI canceller in the mainlobe direction is potted in Figure 3.14 by using the Doppler compensation matrix given in (3.5) and by assuming ideal Doppler compensation, respectively. Since the maximum value is obtained at the 18th pulse, the target Doppler is estimated as $f_{d,t} \in [15 \text{ Hz}, 25 \text{ Hz}]$. Comparing this result with that of Example 1, it could be seen that the target Doppler estimation accuracy has been greatly improved by increasing M.

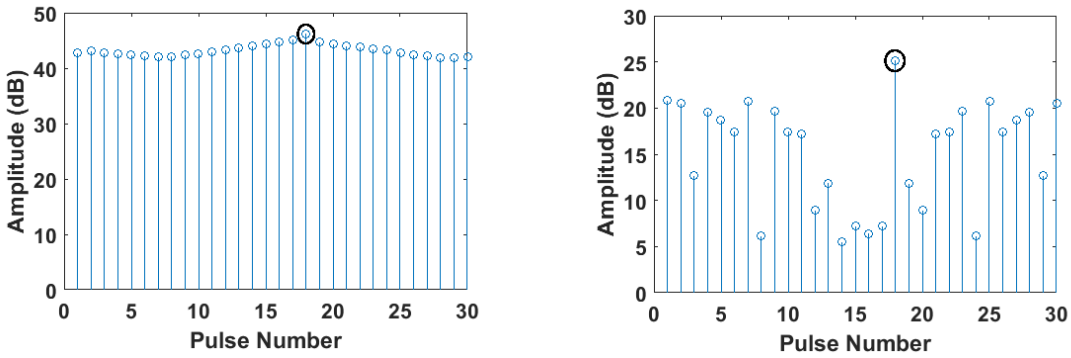

(a) (b)

Figure 3.14 The output signal of the 3-pulse MTI canceller in the mainlobe direction (Example 2). (a) Doppler compenstaion matrix given in (3.5) is used; (b) ideal Doppler compensation is assumed.

3.5. Summary of Chapter 3

An innovative approach to suppressing ground clutter and detecting moving target for airborne radar is presented in this chapter. The essence of the approach is to estimate the fixed clutter Doppler frequency in each beam of the airborne radar and then compensate for it in the beam-time domain using digital beamforming. After Doppler compensation, the ground clutters for airborne radar become near-stationary and can be removed using multi-pulse canceling filters similar to the regular MTI or MTD processing used in ground-based MTI radar systems. This new ground target detection method allows airborne radar to effectively detect ground moving targets in clutter without clutter estimation, as required in conventional STAP. The airborne radar target detection approach can be conveniently implemented with digital beamforming and signal processing at the receiver and the only extra information needed for the clutter compensation is the velocity measurement of the radar platform in real time.

4. SPACE-TIME ADAPTIVE PROCESSING FOR AIRBORNE RADAR TARGET DETECTION IN INHOMOGENEOUS CLUTTER

STAP has been widely used in long-range surveillance airborne radar for moving target detection in ground clutter and other interferences [60]. STAP was first proposed in [21] for phased-array radar. But in recent years, many studies on STAP have been extended to multiple-input multiple-output (MIMO) radar [61-66]. MIMO radar systems are basically classified into two categories: distributed (statistical) MIMO radar with widely separated antennas, and coherent (collocated) MIMO radar with closely spaced antennas. By far, the research on ground clutter suppression with airborne MIMO radar is mainly about distributed MIMO radar, while fewer studies are focused on the coherent MIMO radar [67]. Hence in this chapter, STAP for coherent MIMO radar is considered.

Compared to traditional phased-array radar, coherent MIMO radar has a great number of advantages, such as improved parameter identifiability and enhanced flexibility for transmit beampattern design [68-71]. However, to successfully apply STAP in a MIMO radar system, two problems have to be solved first:

1) The weight vector for a fully adaptive space-time processor is of size MN_TN_R, where N_T, N_R and M are the number of transmit, receive antenna elements and pulses per CPI, respectively. Therefore, when N_T, N_R and M are relatively large, the computational load would be too high for real-time radar operation. For example, when there are 16 transmit/receive antenna elements and 16 pulses per CPI (i.e. $M = 16$, $N_T = 16$ and $N_R = 16$), the interference covariance matrix is 4096×4096, which makes fully-adaptive space-time processing (FA-STAP) impractical.

2) It is well known that the successful implementation of STAP requires accurate clutter estimation. Theoretically, in homogenous interference, under the assumption that the clutters in the primary and secondary bins are IID statistically, the clutter could be estimated accurately from the training data collected from secondary range bins that are adjacent to the primary range bin, i.e. target detection bin [60]. However, in inhomogeneous clutter, STAP could become ineffective and even technically infeasible due to the lack of necessary amount of IID secondary training data.

To reduce the computational complexity, a reduced-dimension clutter suppression method is proposed in [63] for airborne MIMO radar based on STAP. The main idea of [63] is great; however, it should be noted that since the clutter model is not clearly defined in [63], it is difficult to tell the relationship between the severity of the clutter heterogeneity and the performance of the proposed method. Therefore, a time-effective reduced-dimension clutter suppression method, RSTAP, is proposed in this chapter for moving ground target detection in heterogeneous clutter with airborne MIMO radar.

If only one space-time snapshot is available, D-STAP introduced in [35] could be employed. Unlike S-STAP relying on the secondary training data, D-STAP operates on a snapshot-by-snapshot basis to determine the adaptive weights and can be readily implemented in real time [35]. Therefore, D-STAP is expected to outperform S-STAP in inhomogeneous clutter given that the expected (nominal) DOA matches the actual target DOA perfectly. However, when a mismatch between the nominal and the actual target DOA exists, the performance of the classic deterministic STAP approach would be compromised.

The rest of the chapter is organized as following. In Section 4.1, the target and interference models are presented for the airborne MIMO radar system under the assumption of inhomogeneous clutter. In Section 4.2, the performance limitation of conventional FA-STAP is explained. In Section 4.3, the reduced-dimension STAP method termed as RSTAP is proposed for coherent MIMO radar to reduce computational complexity. In Section 4.4, an innovative D-STAP approach termed as R-D-STAP is presented for coherent MIMO radar, which is robust when there is a mismatch between the assumed target DOA and the true target DOA. In Section 4.5, a brief summary of the chapter is given.

4.1. Signal Models for Airborne MIMO Radar in Inhomogeneous Clutter

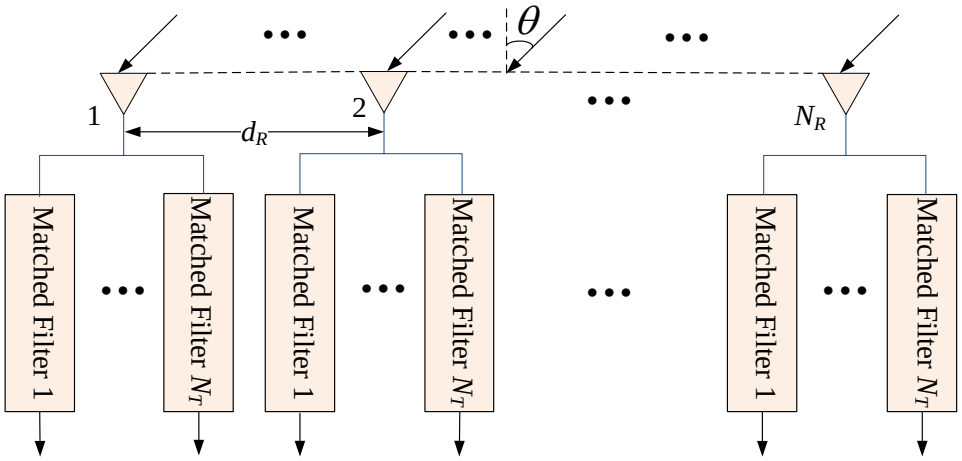

Figure 4.1 MIMO radar matched filtering of received signals.

A coherent MIMO radar with uniform linear transmit antenna array of N_T elements and uniform linear receive antenna array of N_R elements is considered for clutter mitigation beamforming. Without loss of generality, uniform linear arrays (ULA) with the antenna element spacing of d_T and d_R are assumed for transmit and receive antennas, respectively. Since the transmit and receive arrays are assumed to be close to each other

in space, it is assumed that they share the same azimuth angle θ. The MIMO radar receive array is depicted in Figure 4.1.

The orthogonal phase-coded waveform $u_v(t)$ transmitted from antenna element v ($v = 1, 2, \ldots, N_T$) for coherent MIMO radar signal processing is defined as [71]

$$u_v(t) = \begin{cases} e^{j\phi_v^i}, & (i-1)\tau \le t < i\tau, i = 1, 2, \cdots, \Gamma \\ 0 & \text{Otherwise} \end{cases} \tag{4.1}$$

where Γ is the waveform phase-coding length in time domain, τ is the sub-pulse duration, and ϕ_v^i is the phase value of the i-th sub-pulse for element v. Thus the space-time orthogonal waveforms transmitted from the MIMO transmit antenna array are expressed as

$$\mathbf{s}(t) = [e^{j\Phi_1}u_1(t)\ e^{j\Phi_2}u_2(t) \cdots e^{j\Phi_v}u_v(t) \cdots e^{j\Phi_{N_T}}u_{N_T}(t)]^T \tag{4.2}$$

where $\circ$ represents the Hadamard product operator, and Φ_v is the initial phase of element v ($1 \le v \le N_T$). The transmit steering vector $\mathbf{a}_T$ and receive steering vector $\mathbf{a}_R$ in the azimuth broadside direction of θ and elevation direction of ϕ are, respectively,

$$\mathbf{a}_T(\theta, \phi) = \left[1\ e^{-j2\pi\frac{d_T \sin\theta\cos\phi}{\lambda}} \cdots e^{-j2\pi(N_T-1)\frac{d_T \sin\theta\cos\phi}{\lambda}}\right]^T \tag{4.3}$$

$$\mathbf{a}_R(\theta, \phi) = \left[1\ e^{-j2\pi\frac{d_R \sin\theta\cos\phi}{\lambda}} \cdots e^{-j2\pi(N_R-1)\frac{d_R \sin\theta\cos\phi}{\lambda}}\right]^T \tag{4.4}$$

where λ is the radar wavelength. The temporal steering vector is given by

$$\mathbf{a}_D(f_d) = \left[1\ e^{-j2\pi f_d T}\ e^{-j4\pi f_d T} \cdots e^{-j2\pi(M-1)f_d T}\right]^T \tag{4.5}$$

where f_d is the Doppler frequency of target, T is the PRI and M is the number of pulses in a CPI. The combined steering vector is thus given by

$$\mathbf{a}(f_d,\theta_0,\phi_0)=\mathbf{a}_D(f_d,\theta_0,\phi_0)\otimes\mathbf{a}_R(\theta_0,\phi_0)\otimes\mathbf{a}_T(\theta_0,\phi_0) \tag{4.6}$$

where ϕ_0 and θ_0 are the elevation angle and the azimuth angle of the target, respectively.

The matched filter output of the received radar echo signal $\mathbf{x}_r$ may contain target, clutter and noise under hypothesis H_1, or clutter and noise only under hypothesis H_0. Hence, it follows that

$$\begin{cases}\mathbf{x}_{r|H_0}=\mathbf{x}_{c,r}+\mathbf{x}_{n,r} & :H_0\\ \mathbf{x}_{r|H_1}=\mathbf{x}_{t,r}+\mathbf{x}_{c,r}+\mathbf{x}_{n,r} & :H_1\end{cases} \tag{4.7}$$

where $\mathbf{x}_{n,r}$ represents the noise vector, $\mathbf{x}_{c,r}$ is the space-time clutter snapshot, and $\mathbf{x}_{t,r}$ is the target vector given by

$$\mathbf{x}_{t,r}=\alpha\mathbf{a}(f_d,\theta_0,\phi_0) \tag{4.8}$$

where α is the unknown complex amplitude of the target signal due to scattering and propagation losses. The covariance matrix of the radar echo vector is given by

$$\mathbf{R}_r=E[\mathbf{x}_r\mathbf{x}_r^H]. \tag{4.9}$$

$\mathbf{R}_r$ can be further represented as

$$\mathbf{R}_r=\begin{cases}\mathbf{R}_{c,r}+\mathbf{R}_{n,r} & :H_0\\ \mathbf{R}_{c,r}+\mathbf{R}_{n,r}+\mathbf{R}_{t,r} & :H_1\end{cases} \tag{4.10}$$

where $\mathbf{R}_{c,r},\mathbf{R}_{n,r}$ and $\mathbf{R}_{t,r}$ are the covariance matrices of $\mathbf{x}_{c,r},\mathbf{x}_{n,r}$ and $\mathbf{x}_{t,r}$, respectively. The autocorrelation matrix of the target vector can be configured as:

$$\begin{aligned}\mathbf{R}_{t,r}&=E\{\mathbf{x}_{t,r}\mathbf{x}_{t,r}^H\}\\ &=E\{|\alpha|^2\}\begin{bmatrix}\mathbf{R}_{N_TN_R} & e^{j2\pi f_dT}\mathbf{R}_{N_TN_R} & \cdots & e^{j2\pi(M-1)f_dT}\mathbf{R}_{N_TN_R}\\ e^{-j2\pi f_dT}\mathbf{R}_{N_TN_R} & \mathbf{R}_{N_TN_R} & \cdots & e^{j2\pi(M-2)f_dT}\mathbf{R}_{N_TN_R}\\ \cdots & \cdots & \cdots & \cdots\\ e^{-j2\pi(M-1)f_dT}\mathbf{R}_{N_TN_R} & e^{-j2\pi(M-2)f_dT}\mathbf{R}_{N_TN_R} & \cdots & \mathbf{R}_{N_TN_R}\end{bmatrix}\end{aligned} \tag{4.11}$$

where $\mathbf{R}_{N_T N_R}$ is an $N_T N_R \times N_T N_R$ matrix given by

$$\mathbf{R}_{N_T N_R} = \begin{bmatrix} \mathbf{R}_{N_T} & e^{j2\pi \frac{d_R \sin\theta_0 \cos\phi_0}{\lambda}} \mathbf{R}_{N_T} & \cdots & e^{j2\pi (N_R-1)\frac{d_R \sin\theta_0 \cos\phi_0}{\lambda}} \mathbf{R}_{N_T} \\ e^{-j2\pi \frac{d_R \sin\theta_0 \cos\phi_0}{\lambda}} \mathbf{R}_{N_T} & \mathbf{R}_{N_T} & \cdots & e^{j2\pi (N_R-2)\frac{d_R \sin\theta_0 \cos\phi_0}{\lambda}} \mathbf{R}_{N_T} \\ \vdots & \vdots & \ddots & \vdots \\ e^{-j2\pi (N_R-1)\frac{d_R \sin\theta_0 \cos\phi_0}{\lambda}} \mathbf{R}_{N_T} & e^{-j2\pi (N_R-2)\frac{d_R \sin\theta_0 \cos\phi_0}{\lambda}} \mathbf{R}_{N_T} & \cdots & \mathbf{R}_{N_T} \end{bmatrix}$$

(4.12)

where the $N_T \times N_T$ sub-matrix $\mathbf{R}_{N_T}$ in $\mathbf{R}_{N_T N_R}$ is given by

$$\mathbf{R}_{N_T} = \begin{bmatrix} 1 & e^{j2\pi \frac{d_T \sin\theta_0 \cos\phi_0}{\lambda}} & \cdots & e^{j2\pi (N_T-1)\frac{d_T \sin\theta_0 \cos\phi_0}{\lambda}} \\ e^{-j2\pi \frac{d_T \sin\theta_0 \cos\phi_0}{\lambda}} & 1 & \cdots & e^{j2\pi (N_T-1)\frac{d_T \sin\theta_0 \cos\phi_0}{\lambda}} \\ \cdots & \cdots & \cdots & \cdots \\ e^{-j2\pi (N_T-1)\frac{d_T \sin\theta_0 \cos\phi_0}{\lambda}} & e^{-j2\pi (N_T-2)\frac{d_T \sin\theta_0 \cos\phi_0}{\lambda}} & \cdots & 1 \end{bmatrix}. \quad (4.13)$$

The autocorrelation matrix of the target vector can be rewritten as

$$\mathbf{R}_{t,r} = E\{|\alpha|^2\} \mathbf{a}(f_d, \theta_0, \phi_0) \mathbf{a}(f_d, \theta_0, \phi_0)^H \ . \quad (4.14)$$

Under the assumption that the clutters and the noise are mutually independent, the covariance matrix of the total interference for the *r*-th clutter ring is then given by

$$\mathbf{R}_{I,r} = \mathbf{R}_{c,r} + \mathbf{R}_{n,r} \quad (4.15)$$

Assume that the noise is white Gaussian noise with variance σ^2, $\mathbf{R}_{n,r}$ in (4.15) could be further written as

$$\mathbf{R}_{n,r} = E\left\{\mathbf{x}_{n,r} \mathbf{x}_{n,r}^H\right\} = \sigma^2 \mathbf{I}_{N_T N_R M} \quad (4.16)$$

where $\mathbf{I}_{N_T N_R M}$ is an $N_T N_R M \times N_T N_R M$ identity matrix. In the following, the clutter covariance matrix $\mathbf{R}_{c,r}$ in (4.15) is derived.

To simplify the problem, it is further assumed that $d_T = d_R = d_0$ and the velocity of the airborne radar platform is aligned with y-axis, i.e. $\mathbf{v}_a = [0\ v_a\ 0]^T$. The Doppler frequency of the *k*-th clutter patch on the *r*-th clutter ring are represented as $\vartheta_{r,k}$, which is given by

$$\vartheta_{r,k} = \frac{d_0}{\lambda} \sin\theta_{r,k} \cos\phi_r . \tag{4.17}$$

The steering vector for the *k*-th clutter patch is then expressed as

$$\mathbf{a}(\vartheta_{r,k}, \theta_{r,k}, \phi_r) = \mathbf{a}_D(\vartheta_{r,k}, \theta_{r,k}, \phi_r) \otimes \mathbf{a}_R(\theta_{r,k}, \phi_r) \otimes \mathbf{a}_T(\theta_{r,k}, \phi_r) . \tag{4.18}$$

Hence the clutter covariance matrix could be expressed as

$$\mathbf{R}_{c,r} = \sum_{k=1}^{Nc} \sigma_{r,k}^2(\theta_{r,k}, \phi_r)\left(\mathbf{A}_{c,r}(k) \circ \mathbf{R}_{s-t}(\vartheta_{r,k}, \theta_{r,k}, \phi_r)\right) \tag{4.19}$$

where $\circ$ represents the Hadamard product, $\sigma_{r,k}^2(\theta_{r,k}, \phi_r)$ and $\mathbf{A}_{c,r}(k)$ are the observed signal power and the voltage fluctuation between pulses for the *k*-th clutter patch on the *r*-th clutter ring, respectively. $\mathbf{R}_{s-t}(\vartheta_{r,k}, \theta_{r,k}, \phi_r)$ in (4.19) is an $N_T N_R M \times N_T N_R M$ matrix given by

$$\mathbf{R}_{s-t}(\vartheta_{r,k}, \theta_{r,k}, \phi_r) = \mathbf{a}(\vartheta_{r,k}, \theta_{r,k}, \phi_r)\mathbf{a}(\vartheta_{r,k}, \theta_{r,k}, \phi_r)^H . \tag{4.20}$$

$\mathbf{R}_{s-t}(\vartheta_{r,k}, \theta_{r,k}, \phi_r)$ in (4.20) could be further decomposed as

$$\mathbf{R}_{s-t} = \mathbf{R}_1(\vartheta_{r,k}) \otimes \mathbf{R}_2(\theta_{r,k}, \phi_r) \tag{4.21}$$

where $\mathbf{R}_1(\vartheta_{r,k})$ and $\mathbf{R}_2(\theta_{r,k}, \phi_r)$ are the temporal phase lags and spatial phase lags, respectively. It follows that

$$\mathbf{R}_1 = \mathbf{a}_D(\vartheta_{r,k}, \theta_{r,k}, \phi_r)\mathbf{a}_D(\vartheta_{r,k}, \theta_{r,k}, \phi_r)^H \tag{4.22}$$

$$\mathbf{R}_2 = \left(\mathbf{a}_R\left(\theta_{r,k},\phi_r\right)\otimes\mathbf{a}_T\left(\theta_{r,k},\phi_r\right)\right)\left(\mathbf{a}_R\left(\theta_{r,k},\phi_r\right)\otimes\mathbf{a}_T\left(\theta_{r,k},\phi_r\right)\right)^H \tag{4.23}$$

In the following, the clutter covariance matrix $\mathbf{R}_{c,r}$ in (4.19) is derived under the assumption of two types of clutter heterogeneity: spectral heterogeneity and amplitude heterogeneity.

4.1.1. Spectral heterogeneity

Spectral heterogeneity of clutter is caused by intrinsic clutter motion (ICM) due to soft scatterers such as trees, ocean waves and weather effects [24]. Since the null width for clutter suppression is set to fit the mean spectral spread, when ICM exists the null width would be too narrow for some range cells and too wide for others, which may lead to either residue clutter that degrades SINR and increases false alarm rate, or target signal cancellation (i.e. over-nulling).

When ICM is taken into consideration, according to [60], the temporal fluctuation could be modeled as a wide-sense stationary (WSS) random process. Assume that the Doppler spectrum is Gaussian-distributed, the temporal autocorrelation of the fluctuation between pulse *i* and pulse *j*, which is also Gaussian-distributed, is expressed as

$$\rho_I(i-j) = \sigma^2\xi_k e^{\frac{-8\pi^2\sigma_v^2(i-j)^2T^2}{\lambda^2}} \tag{4.24}$$

where ξ_k is the clutter-to-noise ratio (CNR) and σ_v is the velocity standard deviation. According to [60], when the spatial sampling is uniform, the pulse-to-pulse correlation matrix could be expressed as a symmetric Toeplitz matrix:

$$\tilde{\mathbf{A}}_{c,r}(k)=\begin{bmatrix} \rho_I(0) & \rho_I(1) & \rho_I(2) & \cdots & \rho_I(M-1) \\ \rho_I(1) & \rho_I(0) & \rho_I(1) & \cdots & \rho_I(M-2) \\ \rho_I(2) & \rho_I(1) & \rho_I(0) & \cdots & \rho_I(M-3) \\ \cdots & \cdots & \cdots & \cdots & \cdots \\ \rho_I(M-1) & \rho_I(M-2) & \rho_I(M-3) & \cdots & \rho_I(0) \end{bmatrix}. \tag{4.25}$$

Since $\mathbf{R}_{c,r}$ is an $N_T N_R M \times N_T N_R M$ matrix, and the decorrelation doesn't affect the spectral covariance matrix, $\mathbf{A}_{c,r}(k)$ in (4.19) is expressed as

$$\mathbf{A}_{c,r}(k)=\tilde{\mathbf{A}}_{c,r}(k)\otimes\begin{bmatrix}1 & 1 & \cdots & 1\end{bmatrix}_{1\times N_R N_T} \tag{4.26}$$

4.1.2. Amplitude heterogeneity

Amplitude heterogeneity is the most common type of clutter heterogeneity [24]. The possible causes of amplitude heterogeneity include shadowing and obscuration, range-dependent change in clutter reflectivity, and strong stationary discretes [24]. A brief analysis of the impact of amplitude heterogeneous clutter on improvement factor when adaptive Doppler filters are employed is given in [72].

When clutter reflectivity varies in over range and angle, $\sigma^2_{r,k}(\theta_{r,k},\phi_r)$ in (4.19) has to be changed to $\sigma^2_{r,k/s,m}$, $s=1,\cdots,N_T N_R, m=1,\cdots M$ to reflect the dependency. The single channel, single pulse CNR measured at the (*s*, *m*)-th spatial-time pair at the *r*-th range ring is expressed as

$$\sigma^2_{r,k;/s,m}=\kappa_1\left(\frac{G_t(\theta_{s,m},\phi_r)g_r(\theta_{s,m},\phi_r)\sin(\psi_{g/r})}{r_s^4}\right)\gamma_{r,k;/s,m} \tag{4.27}$$

where κ_1 is a constant, $G_t(\theta_{s,m},\phi_r)$ and $g_r(\theta_{s,m},\phi_r)$ are the transmit antenna gain and the receive antenna gain for the azimuth-elevation pair $(\theta_{s,m},\phi_r)$, respectively, $\psi_{g/k}$ is the grazing angle, r_s is the slant range, and $\gamma_{r,k;/s,m}$ represents the reflectivity measured at the

(*s*, *m*)-th spatial-time pair at the *r*-th range ring. For simplicity, $\gamma_{r,k;/s,m}$ is written as γ_c in the following. Assume that clutter power follows the Gamma probability distribution, it follows that [60]:

$$p(\gamma_c) = \frac{1}{\Gamma(\tilde{\alpha})\tilde{\beta}^{\tilde{\alpha}}} \gamma_c^{\tilde{\alpha}-1} e^{-\frac{\gamma_c}{\tilde{\beta}}} \tag{4.28}$$

where

$$\tilde{\alpha} = \frac{E\{\gamma_c\}^2}{\mathrm{var}\{\gamma_c\}}; \tilde{\beta} = \frac{\mathrm{var}\{\gamma_c\}}{E\{\gamma_c\}} \tag{4.29}$$

where $\tilde{\alpha}$ and $\tilde{\beta}$ are shape parameter and scale parameter, respectively. It could be seen in (4.28) and (4.29) that when $E\{\gamma_c\}$ is large compare to $\mathrm{var}\{\gamma_c\}$, the clutter is more homogeneous. Hence it is expected that the SINR loss will be less for larger $\tilde{\alpha}$ when $\tilde{\beta}$ is fixed.

4.2. Performance Limitation of Conventional STAP in Heterogeneous Clutter

When fully-adaptive S-STAP is used, the MIMO radar beamforming filter for target detection is obtained as

$$\mathbf{w}_r = \hat{a}\mathbf{R}_{I,r}^{-1}\mathbf{a}(f_d, \theta_0, \phi_0) \tag{4.30}$$

where $\hat{a}$ is an arbitrary constant. When the weight vector is applied to the space-time snapshot, the output is given by

$$y_r = \mathbf{w}_r^H \mathbf{x}_r . \tag{4.31}$$

And the output SINR is the given by

$$SINR = \frac{\mathbf{w}_r^H \mathbf{R}_{t,r} \mathbf{w}_r}{\mathbf{w}_r^H \mathbf{R}_{I,r} \mathbf{w}_r} . \tag{4.32}$$

The optimal MIMO radar beamforming weight vector is found by maximizing the output SINR in (4.32). Taking into consideration of (4.14), (4.32) is rewritten as

$$SINR = \frac{E\{|\alpha|^2\}\left|\mathbf{w}_r^H \mathbf{a}(f_d, \theta_0, \phi_0)\right|^2}{\mathbf{w}_r^H \mathbf{R}_{I,r} \mathbf{w}_r}. \tag{4.33}$$

The optimal weight vector can be obtained by maximizing (4.33), or equivalently, maintaining distortionless response to the desired signal and minimizing the output interference (i.e. clutter-plus-noise) power. And the optimization problem is expressed as

$$\begin{cases} \min\limits_{\mathbf{w}_r} \mathbf{w}_r^H \mathbf{R}_{I,r} \mathbf{w}_r \\ \text{s.t. } \mathbf{w}_r^H \mathbf{a}(f_d, \theta_0, \phi_0) = 1 \end{cases} \tag{4.34}$$

, which is commonly called the minimum variance distortionless response (MVDR) beamformer [38]. And it is well-known that the solution to (4.34) is given by:

$$\mathbf{w}_r = \hat{\alpha} \mathbf{R}_{I,r}^{-1} \mathbf{a}(f_d, \theta_0, \phi_0) \tag{4.35}$$

where

$$\hat{\alpha} = \frac{1}{\mathbf{a}(f_d, \theta_0, \phi_0)^H \mathbf{R}_{I,r}^{-1} \mathbf{a}(f_d, \theta_0, \phi_0)}. \tag{4.36}$$

Theoretically, the maximum output SINR could be achieved with the weighting vector in (4.35). However, it should be noted that $\mathbf{R}_{I,r}$ in (4.35) is not precisely known in practice and has to be estimated in real time. Several different approaches are available for the estimation of $\mathbf{R}_{I,r}$, and among them the maximum likelihood estimate (MLE) is the most popular [22], where the covariance matrix is estimated as

$$E\left\{\hat{\mathbf{R}}_{I,r}\right\} = \frac{1}{U} \sum_{\substack{i=1 \\ i \neq r}}^{U} \mathbf{x}_{I,i} \mathbf{x}_{I,i}^H = \sum_{\substack{i=1 \\ i \neq r}}^{U} \frac{\mathbf{R}_{I,i}^H}{U} = \mathbf{R}_{I,r} \tag{4.37}$$

where U is the number of interference samples and $\mathbf{x}_{I,i}$ is the i-th interference sample vector. Substituting $\hat{\mathbf{R}}_{I,r}$ for $\mathbf{R}_{I,r}$ in (4.35) is called sample matrix inverse (SMI) in literatures [73]. The validity of the SMI approach depends on the assumption that $E\{\hat{\mathbf{R}}_{I,r}\} = \mathbf{R}_{I,r}$. However, in heterogeneous clutter where $E\{\hat{\mathbf{R}}_r\} = \mathbf{R}_{I,h} \neq \mathbf{R}_{I,r}$, and the weight vector of the MIMO radar beamforming filter is given by

$$\hat{\mathbf{w}}_r = \hat{a}\frac{\mathbf{a}(f_d, \theta_0, \phi_0)}{\mathbf{R}_{I,h}^{-1}}. \tag{4.38}$$

Hence the covariance matrix estimation error is

$$\Delta\mathbf{R}_e = \mathbf{R}_{I,r}^{-1} - \mathbf{R}_{I,h}^{-1}. \tag{4.39}$$

According to [24], the output SINR in (4.32) could also expressed as

$$SINR = SNR \times L_1 \times L_2, \quad 0 \le L_1, L_2 \le 1 \tag{4.40}$$

where SNR is the input signal-to-noise ratio, and L_1 and L_2 represent the SINR loss due to colored noise and the SINR loss due to the error between optimal weight vector and adaptive weight vector, respectively. Assume that σ_s^2 is the single channel, single pulse target signal power, L_1 is expressed as

$$L_1 = \frac{SINR|_{\mathbf{w}_r}}{SNR} = \frac{\sigma^2}{MN_T N_R \sigma_s^2}\frac{\mathbf{w}_r^H \mathbf{R}_{t,r}\mathbf{w}_r}{\mathbf{w}_r^H \mathbf{R}_{I,r}\mathbf{w}_r} \tag{4.41}$$

L_2 is expressed as

$$L_2 = \frac{SINR|_{\mathbf{w}_r=\hat{\mathbf{w}}_r}}{SINR|_{\mathbf{w}_r=\mathbf{w}_{opt}}} = \frac{\hat{\mathbf{w}}_r^H \mathbf{R}_{t,r}\hat{\mathbf{w}}_r}{\hat{\mathbf{w}}_r^H \mathbf{R}_{I,r}\hat{\mathbf{w}}_r}\frac{\mathbf{w}_{opt}^H \mathbf{R}_{I,r}\mathbf{w}_{opt}}{\mathbf{w}_{opt}^H \mathbf{R}_{t,r}\mathbf{w}_{opt}} \tag{4.42}$$

where $\hat{\mathbf{w}}_r$ is the adaptive weight vector and $\mathbf{w}_{opt}$ is the optimal weight vector. According to (4.42), the SINR loss due to the covariance matrix estimation error is expressed as

$$
\begin{aligned}
L_s &= \frac{SINR|_{\mathbf{w}_r=\hat{\mathbf{w}}_r}}{SINR|_{\mathbf{w}_r=\mathbf{w}_{opt}}} \\
&= \frac{\mathbf{w}_{opt}\mathbf{R}_{t,r}\mathbf{w}_{opt}\left(\hat{\mathbf{w}}_r^H\mathbf{R}_{I,r}\hat{\mathbf{w}}_r\right)}{\mathbf{w}_{opt}^H\mathbf{R}_{I,r}\mathbf{w}_{opt}\left(\hat{\mathbf{w}}_r^H\mathbf{R}_{t,r}\hat{\mathbf{w}}_r\right)} \\
&= \frac{\sigma_s^2\left|\mathbf{a}(f_d,\theta_0,\phi_0)^H\mathbf{R}_{I,h}^{-1}\mathbf{a}(f_d,\theta_0,\phi_0)\right|^2\mathbf{a}(f_d,\theta_0,\phi_0)^H\mathbf{R}_{I,r}^{-1}\mathbf{a}(f_d,\theta_0,\phi_0)}{\mathbf{a}(f_d,\theta_0,\phi_0)^H\mathbf{R}_{I,h}^{-1}\mathbf{R}_{I,r}\mathbf{R}_{I,h}^{-1}\mathbf{a}(f_d,\theta_0,\phi_0)\sigma_s^2\left|\mathbf{a}(f_d,\theta_0,\phi_0)^H\mathbf{R}_{I,r}^{-1}\mathbf{a}(f_d,\theta_0,\phi_0)\right|^2} \\
&= \frac{\left|\mathbf{a}_0^H\mathbf{R}_{I,h}^{-1}\mathbf{a}_0\right|^2}{\mathbf{a}_0^H\mathbf{R}_{I,h}^{-1}\mathbf{R}_{I,r}\mathbf{R}_{I,h}^{-1}\mathbf{a}_0\left(\mathbf{a}_0^H\mathbf{R}_{I,r}^{-1}\mathbf{a}_0\right)}
\end{aligned}
\tag{4.43}
$$

By plugging (4.39) into (4.43), L_s could be expressed in terms of $\Delta\mathbf{R}_e$ as

$$
\begin{aligned}
L_s &= \frac{\left|\mathbf{a}_0^H(\mathbf{R}_{I,r}^{-1}+\Delta\mathbf{R}_e)\mathbf{a}_0\right|^2}{\mathbf{a}_0^H(\mathbf{R}_{I,r}^{-1}+\Delta\mathbf{R}_e)\mathbf{R}_{I,r}(\mathbf{R}_{I,r}^{-1}+\Delta\mathbf{R}_e)\mathbf{a}_0\left(\mathbf{a}_0^H\mathbf{R}_{I,r}^{-1}\mathbf{a}_0\right)} \\
&= \frac{\left|\mathbf{a}_0^H\left(\mathbf{R}_{I,r}^{-1}+\Delta\mathbf{R}_e\right)\mathbf{a}_0\right|^2}{\left(\mathbf{a}_0^H\mathbf{R}_{I,r}^{-1}\mathbf{a}_0+2\mathbf{a}_0^H\Delta\mathbf{R}_e\mathbf{a}_0+\mathbf{a}_0^H\Delta\mathbf{R}_e\mathbf{R}_{I,r}\Delta\mathbf{R}_e\mathbf{a}_0\right)\left(\mathbf{a}_0^H\mathbf{R}_{I,r}^{-1}\mathbf{a}_0\right)}
\end{aligned}
\tag{4.44}
$$

It should be noted that a different form of the SINR loss is obtained in [24] (Equation (10.32) on pp. 317) as

$$
L_{s2} = \frac{\left|\mathbf{a}_0^H\Delta\mathbf{R}_e\mathbf{a}_0\right|^2}{\mathbf{a}_0^H\mathbf{R}_{I,r}^{-1}\mathbf{a}_0\left(\mathbf{a}_0^H\Delta\mathbf{R}_e\mathbf{R}_{I,r}\Delta\mathbf{R}_e\mathbf{a}_0\right)} \tag{4.45}
$$

However, since $\mathbf{R}_{I,r}^{-1} << \Delta\mathbf{R}_e$, L_s is approximately equal to L_{s2}.

According to the RMB rule described in [23], in order to achieve an adaptive SINR loss of -3 dB, the number of IID samples has to be approximately twice the product of the number antenna elements and the number of pulses per CPI, i.e. $U \approx 2MN - 3$ for MIMO radar and $U \approx 2MN_TN_R - 3$ for phased-array radar. The expected SINR loss for SMI with different number of samples is plotted in Figure 4.2. It is assumed that $N = N_T = N_R = 8$, $M = 16$. It could be seen that for phased-array radar, the number of samples has to

be at least $2MN-3=253$ for a SINR loss of 3 dB. And when 128 samples are used to estimate the interference covariance matrix, the SINR loss is approximately -22 dB. As for MIMO radar, the number of samples required for an accurate estimation of the interference matrix is even higher. Worse still, in inhomogeneous clutter, it is often difficult to obtain the necessary amount of IID secondary data.

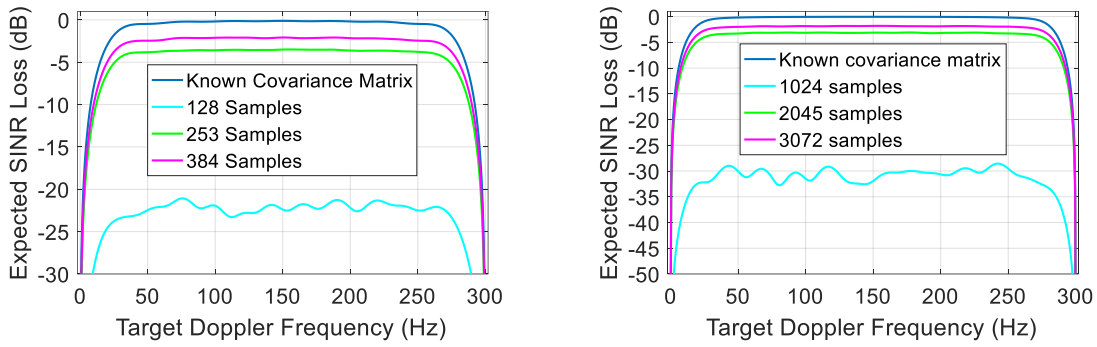

Figure 4.2 Expected SINR loss for SMI with different number of samples.
(a) Phased-array radar (b) MIMO radar

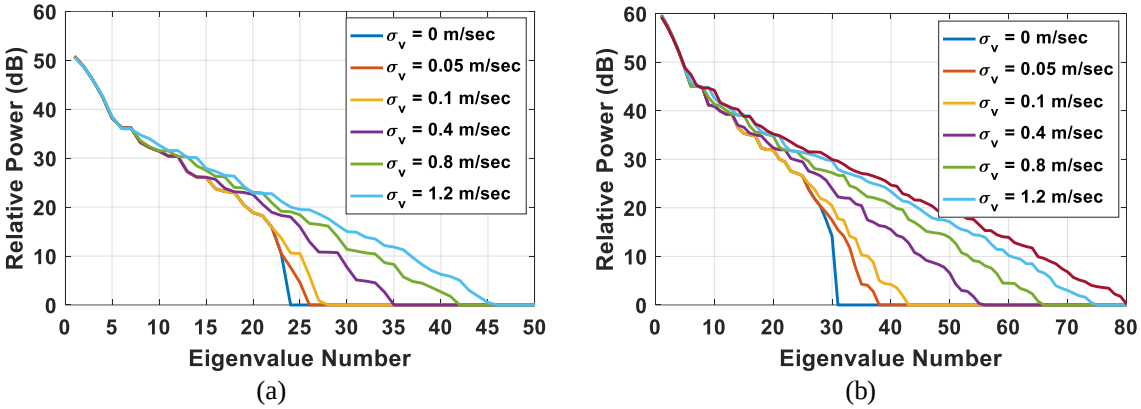

Figure 4.3 Eigenspectra for different spectral spread values.
(a) Phased-array radar (b) MIMO radar

The eigenspectra for different spectral spread values for phased-array radar and MIMO radar are plotted in Figure 4.3 (a) and (b), respectively. It is assumed that the integrated CNR is 50 dB, M = 16, $N_T = N_R$ = 8. The noise floor is arbitrarily set to zero decibel. Five cases of spectral heterogeneity are considered: $\sigma_v = 0.05$ m/s , $\sigma_v = 0.1$m/s ,

$\sigma_v = 0.4\,\text{m/s}$, $\sigma_v = 0.8\,\text{m/s}$ and $\sigma_v = 1.2\,\text{m/s}$, along with the no ICM case, i.e. $\sigma_v = 0\,\text{m/s}$. It could be seen in Figure 4.3 that with the increasing of the spectral spread, the largest eigenvalues remain unchanged, but the rank of the interference matrix increases. Meanwhile, comparing Figure 4.3 (a) and (b), it could also be seen that the rank of the interference matrix is higher when MIMO radar is used than the case where phased-array radar is used.

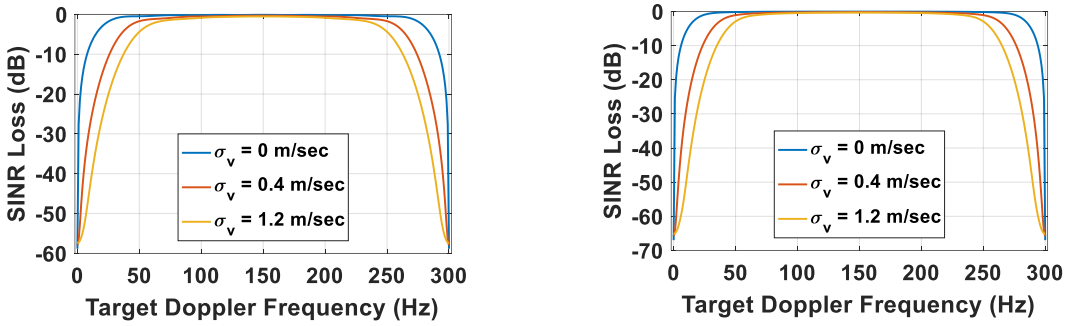

(a) (b)

Figure 4.4 SINR loss for different spectral spread values.
(a) Phased-array radar (b) MIMO radar

The SINR losses for different spectral spread values for phased-array radar and MIMO radar are plotted in Figure 4.4 (a) and (b), respectively. Three cases are considered: $\sigma_v = 0\,\text{m/s}$, $\sigma_v = 0.4\,\text{m/s}$ and $\sigma_v = 1.2\,\text{m/s}$. It could be seen in Figure 4.4 that the SINR losses increase with the spectral heterogeneity. It could also be seen that the SINR losses for MIMO radar are greater than those for phased-array radar in spectral heterogeneous clutter due to higher DOFs.

To further investigate the performance degradation for these target Doppler frequencies, 2D angle-Doppler responses of S-STAP in spectrally heterogeneous clutter for phased-array radar and MIMO radar are plotted in Figure 4.5 and Figure 4.6, respectivley, under the assumption $M = 16$, $N_T = N_R = 16$. Three cases are considered:

$\sigma_v = 0\,\text{m/s}$, $\sigma_v = 0.4\,\text{m/s}$ and $\sigma_v = 1.2\,\text{m/s}$. It could be seen in both Figure 4.5 and Figure 4.6 that with the increase of the clutter spectral heterogeneity, the null that spans the clutter ridge becomes wider. Compare Figure 4.6 with Figure 4.5, it could be seen that deeper nulls are formed for clutter suppression with MIMO radar due to the increased DOF.

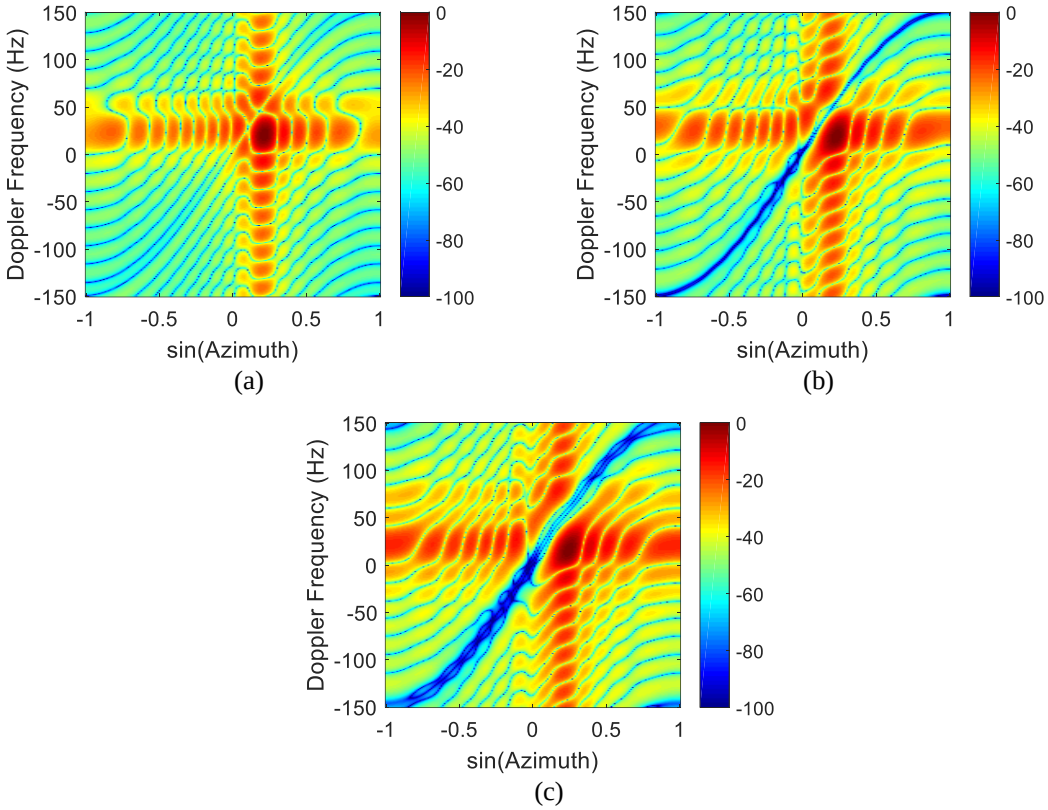

Figure 4.5 2D angle-Doppler responses for different spectral spread values when conventional STAP filter is used (phased-array radar).
(a) σ_v = 0 m/s. (b) σ_v = 0.4 m/s. (c) σ_v = 1.2 m/s.

The principle cuts of the angle-Doppler response at target azimuth and Doppler for different spectral spread values when S-STAP filter is used for phased-array radar and MIMO radar are plotted in Figure 4.7 (a) and (b), respectively. It could be seen that the maximum gain of the azimuth pattern at the expected target Doppler (above) and the Doppler resonse at the target azimuth (below) deviate more and more from the expected

target and Doppler with the increase of σ_v. Compare Figure 4.7 (b) with Figure 4.7 (a), it could be seen that deeper nulls are formed for clutter suppression with MIMO radar due to the increased DOF. However, similar "pattern deviation" phenomena are observed with the increase of σ_v. It means that for both phased-array radar and MIMO radar, the maximum antenna gain is not achieved at the expected target and Doppler in heterogeneous clutter, hence the detection probability of would suffer.

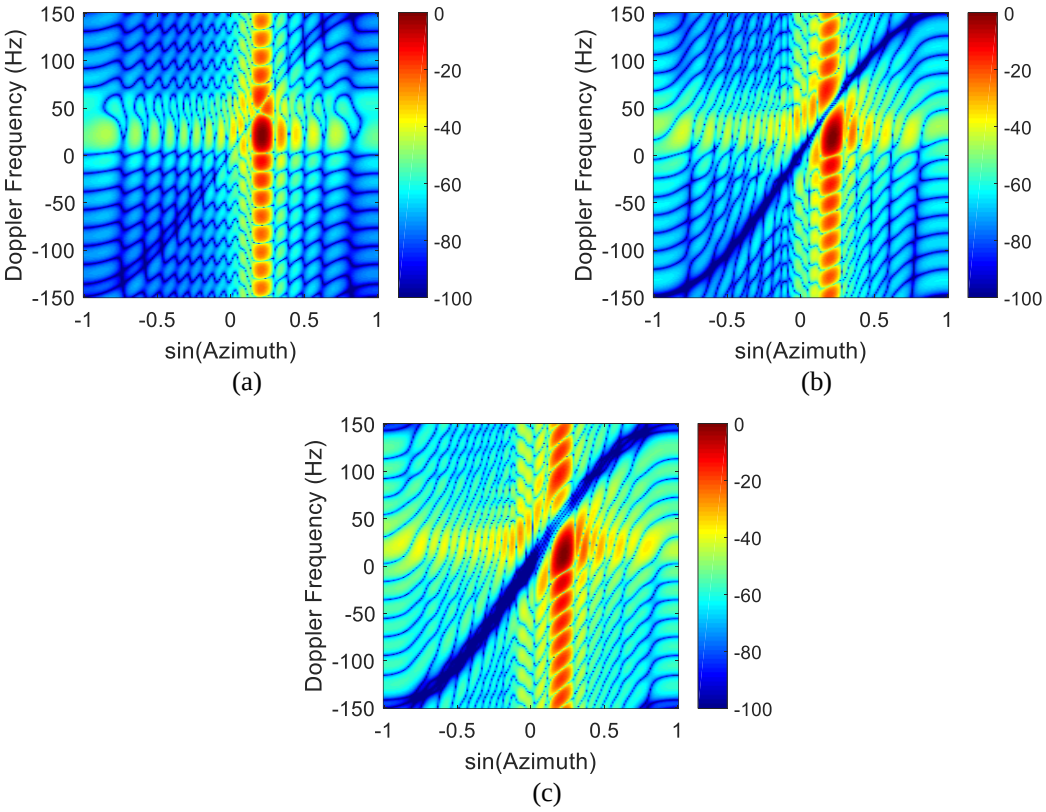

Figure 4.6 2D angle-Doppler responses for different spectral spread values when conventional STAP filter is used (MIMO radar).
(a) σ_v = 0 m/s. (b) σ_v = 0.4 m/s. (c) σ_v = 1.2 m/s.

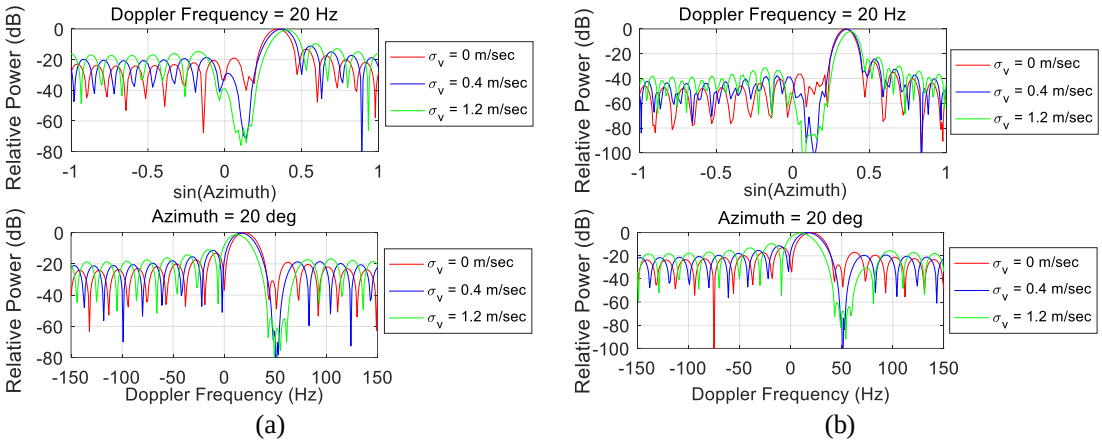

Figure 4.7 Principle cuts of angle-Doppler responses when conventional STAP filter is used. (a) Phased-array radar (b) MIMO radar

4.3. Reduced-dimensional STAP

In order to obtain an acceptable performance (i.e. -3 dB SINR loss according to the RMB rule [23]), the number of IID samples needed to estimate $\mathbf{R}_{I,r}$ should be $U \approx 2MN - 3$ for phased-array radar and $U \approx 2MN_T N_R - 3$ for MIMO radar, which is often not available in inhomogeneous clutter. Meanwhile, since the inversion of $\mathbf{R}_{I,r}$ involves a computational complexity of $O(M^3 N_T^3 N_R^3)$, instead of using (4.38) directly, a time-effective clutter suppression method termed as reduced-dimension space-time adaptive processing (RSTAP) is proposed in the following to reduce the computational complexity and lower the training samples requirement. The performance of the proposed method is evaluated in inhomogeneous clutter.

First, the received signal corresponding to the *m*-th pulse, *n*-th receive element and *v*-th transmit element is defined as $x_{n,v,m}$. The received signal vector corresponding to the *m*-th pulse is then expressed as

$$\mathbf{x}(m) = \left[x_{1,1,m} \cdots x_{1,N_T,m} \cdots x_{n,v,m} \cdots x_{N_R,1,m} \cdots x_{N_R,N_T,m}\right]^T. \tag{4.46}$$

And the received data matrix for M pulses during a CPI is

$$\mathbf{X} = \left[\mathbf{x}(1)\ \mathbf{x}(2)\ \cdots \mathbf{x}(M)\right]. \tag{4.47}$$

By stacking the column vector of $\mathbf{X}$, the following expression is obtained

$$\mathbf{x} = \mathrm{vec}(\mathbf{X}). \tag{4.48}$$

Next, $\bar{\mathbf{x}}$ is defined as

$$\bar{\mathbf{x}} = \left(\mathrm{vec}(\mathbf{X}^T)\right)^T. \tag{4.49}$$

It is easy to find a row vector $\bar{\mathbf{w}}_r$ that satisfies

$$\mathbf{w}_r^H \mathbf{x} = \bar{\mathbf{x}}\bar{\mathbf{w}}_r^H. \tag{4.50}$$

Hence the optimization problem in (4.35) could be rewritten as

$$\begin{cases} \min\limits_{\bar{\mathbf{w}}} \bar{\mathbf{w}}_r^H \bar{\mathbf{R}}_{I,r} \bar{\mathbf{w}}_r \\ \text{s.t. } \bar{\mathbf{a}}(f_d, \theta_0, \phi_0)\bar{\mathbf{w}}_r^H = 1 \end{cases} \tag{4.51}$$

where

$$\bar{\mathbf{a}}(f_d, \theta_0, \phi_0) = \mathbf{a}_R(\theta_0, \phi_0)^T \otimes \mathbf{a}_T(\theta_0, \phi_0)^T \otimes \mathbf{a}_D(f_d, \theta_0, \phi_0)^T \tag{4.52}$$

$\bar{\mathbf{R}}_{I,r}$ in (4.51) is the covariance matrix of $\bar{\mathbf{x}}_{c,r} + \bar{\mathbf{x}}_{n,r}$, which is expressed as

$$\begin{aligned} \bar{\mathbf{R}}_{I,r} &= E\left\{\left(\bar{\mathbf{x}}_{c,r} + \bar{\mathbf{x}}_{n,r}\right)^H \left(\bar{\mathbf{x}}_{c,r} + \bar{\mathbf{x}}_{n,r}\right)\right\} + \sigma^2 \mathbf{I}_{MN_TN_R} \\ &= \left[\sum_{k=1}^{N_c} \alpha_k \bar{\mathbf{a}}(\vartheta_{r,k}, \theta_{r,k}, \phi_r)\right]^H \left[\sum_{k=1}^{N_c} \alpha_k \bar{\mathbf{a}}(\vartheta_{r,k}, \theta_{r,k}, \phi_r)\right] + \sigma^2 \mathbf{I}_{MN_TN_R} \end{aligned} \tag{4.53}$$

where

$$\bar{\mathbf{a}}(\vartheta_{r,k}, \theta_{r,k}, \phi_r) = \mathbf{a}_R(\theta_{r,k}, \phi_r)^T \otimes \mathbf{a}_T(\theta_{r,k}, \phi_r)^T \otimes \mathbf{a}_D(\vartheta_{r,k}, \theta_{r,k}, \phi_r)^T. \tag{4.54}$$

In the following, the weight vector will be decomposed twice to lower the dimension. The first decomposition is termed as first-order reduced-dimension STAP

(1st-RSTAP), and the second decomposition is termed as second-order reduced-dimension STAP (2nd-RSTAP).

4.3.1. 1st-RSTAP

In this part, the 1st-RSTAP is carried out. Firstly, the weight vector $\mathbf{w}_r$ and the corresponding vector $\overline{\mathbf{w}}_r$ in (4.50) are decomposed, respectively, as

$$\mathbf{w}_r = \mathbf{v}^* \otimes \mathbf{u} \tag{4.55}$$

$$\overline{\mathbf{w}}_r = \left(\mathbf{u} \otimes \mathbf{v}^*\right)^T \tag{4.56}$$

where $\mathbf{v} = [v_1, v_2, \cdots, v_M]^T$ and $\mathbf{u} = [u_1, u_2, \cdots, u_{N_T N_R}]^T$. If $\mathbf{R}_{I,r}$ is partitioned into M^2 submatrices of dimension $N_T N_R \times N_T N_R$ and $\overline{\mathbf{R}}_{I,n}$ is partitioned into $N_T^2 N_R^2$ matrices of submatrices of dimension $M \times M$, it follows that

$$\mathbf{w}_r^H \mathbf{R}_{I,r} \mathbf{w}_r = \mathbf{u}^H \left[\sum_{\beta=1}^{M} \sum_{\gamma=1}^{M} v_\beta \mathbf{R}_{I,r}^{(\beta,\gamma)} v_\gamma^* \right] \mathbf{u} \tag{4.57}$$

and

$$\overline{\mathbf{w}}_r^H \overline{\mathbf{R}}_{I,r} \overline{\mathbf{w}}_r = \mathbf{v}^H \left[\sum_{\varepsilon=1}^{N_T N_R} \sum_{\eta=1}^{N_T N_R} u_\varepsilon \overline{\mathbf{R}}_{I,r}^{(\varepsilon,\eta)} u_\eta^* \right] \mathbf{v} \tag{4.58}$$

where $\mathbf{R}_{I,r}^{(\beta,\gamma)}$ is the (β, γ)-th submatrix of $\mathbf{R}_{I,r}$, and $\overline{\mathbf{R}}_{I,r}^{(\varepsilon,\eta)}$ is the (ε, η)-th submatrix of $\overline{\mathbf{R}}_{I,r}$. To simplify the expressions in (4.57) and (4.58), two new matrices are defined as

$$\mathbf{R}_v = \sum_{\beta=1}^{M} \sum_{\gamma=1}^{M} v_\beta \mathbf{R}_{I,r}^{(\beta,\gamma)} v_\gamma^* \tag{4.59}$$

$$\mathbf{R}_u = \sum_{\varepsilon=1}^{N_T N_R} \sum_{\eta=1}^{N_T N_R} u_\varepsilon \overline{\mathbf{R}}_{I,r}^{(\varepsilon,\eta)} u_\eta^* . \tag{4.60}$$

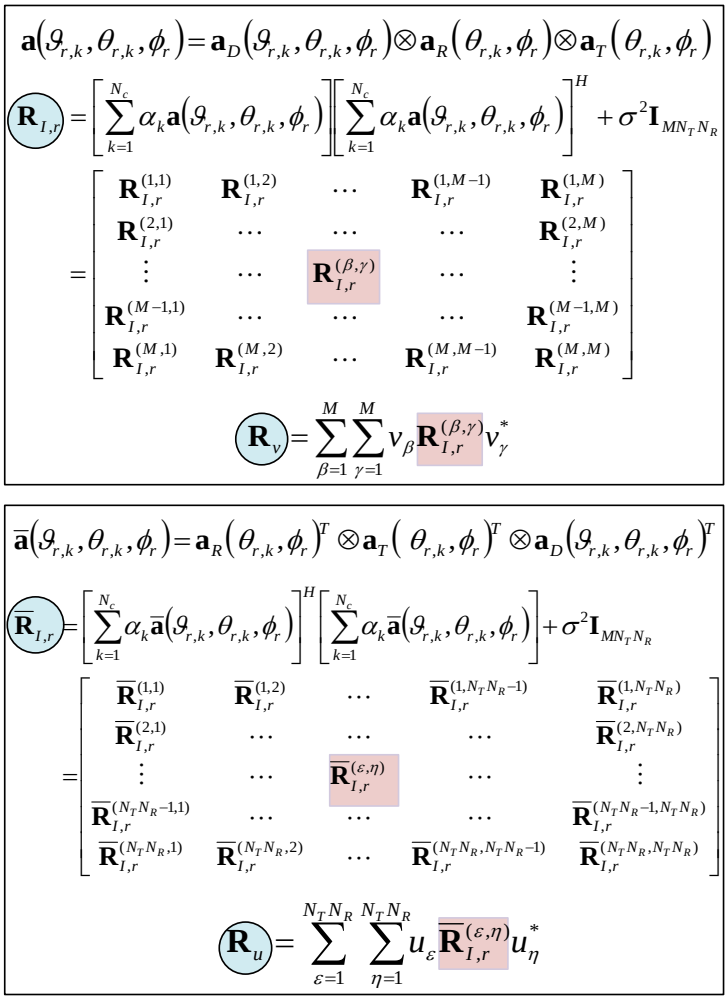

Figure 4.8 The relationship between the interference matrix and the sub-matrices in 1st-RSTAP.

The relationship between $\mathbf{R}_{I,r}$, $\overline{\mathbf{R}}_{I,r}$, $\mathbf{R}_v$ and $\mathbf{R}_u$ is shown in Figure 4.8. It should be noted that $\mathbf{R}_v$ is an $N_TN_R\times N_TN_R$ matrix, while $\mathbf{R}_u$ is an $M\times M$ matrix. Therefore, (4.34) could be rewritten as

$$\begin{cases}\min\limits_{\mathbf{u}}\ \mathbf{u}^H\mathbf{R}_v\mathbf{u}\\ \text{s.t.}\ \ \mathbf{u}^H\mathbf{A}\mathbf{v}=1\end{cases}. \tag{4.61}$$

And (4.51) could be rewritten as

$$\begin{cases}\min\limits_{\mathbf{v}}\ \mathbf{v}^H\mathbf{R}_u\mathbf{v}\\ \text{s.t.}\ \ \mathbf{v}^H\mathbf{A}^H\mathbf{u}=1\end{cases} \tag{4.62}$$

where the $N_T N_R \times M$ matrix $\mathbf{A}$ is expressed as

$$\mathbf{A} = \left[\mathbf{a}_R(\theta_0, \phi_0) \otimes \mathbf{a}_T(\theta_0, \phi_0)\right]\mathbf{a}_D(f_d, \theta_0, \phi_0)^T . \tag{4.63}$$

The solutions to (4.61) and (4.62) are, respectively,

$$\mathbf{u} = \alpha_u \mathbf{R}_v^{-1}\mathbf{A}\mathbf{v} \tag{4.64}$$

$$\mathbf{v} = \alpha_v \mathbf{R}_u^{-1}\mathbf{A}^H\mathbf{u} \tag{4.65}$$

where α_u and α_v are constants given by

$$\alpha_u = \frac{1}{(\mathbf{A}\mathbf{v})^H \mathbf{R}_v^{-1}(\mathbf{A}\mathbf{v})} \tag{4.66}$$

$$\alpha_v = \frac{1}{(\mathbf{A}^H\mathbf{u})^H \mathbf{R}_u^{-1}(\mathbf{A}^H\mathbf{u})} . \tag{4.67}$$

The weight vector calculation process with 1st-RSTAP is shown in Figure 4.9. It could be seen that for iteration step $i = 0$, the $M \times 1$ column vector $\mathbf{v}$ is randomly initialized. Then the $N_T N_R \times 1$ column vector $\mathbf{u}$ is obtained according to (4.64), and $\mathbf{v}$ is updated according to (4.65). It should be noted that the output SINR in (4.32) is maximized when $\alpha_u = 1$ and $\alpha_v = 1$. After three iterations (i.e. $i = 0, 1, 2$), $\mathbf{u}$ and $\mathbf{v}$ are stabilized, which are then used to calculate $\mathbf{w}_r$.

By far, the matrices to be calculated become the $N_T N_R \times N_T N_R$ matrix $\mathbf{R}_v$ and the $M \times M$ matrix $\mathbf{R}_u$, instead of the $MN_T N_R \times MN_T N_R$ matrix $\mathbf{R}_{I,r}$. However, the computational complexity is still high. For example, in a simple case where $M = N_T = N_R = 16$, $\mathbf{R}_v$ will be a 256×256 matrix. Meanwhile, it should also be noted that $2 \times \max(N_T N_R, M) - 3 = 509$ IID samples are needed to estimate $\mathbf{R}_v$ and $\mathbf{R}_u$. Therefore, in the following, 2nd-RSTAP is carried out to further reduce the computational complexity.

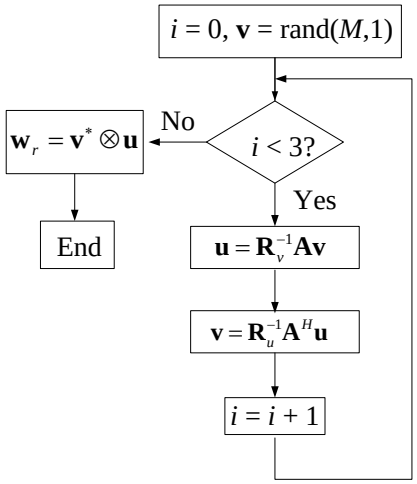

Figure 4.9 Flowchart of the weight vector calculation process (1st-RSTAP).

4.3.2. 2nd-RSTAP

1 In this part, the ranks of the covariance matrices to be estimated are further reduced through 2nd-RSTAP. The vector $\mathbf{u}$ in (4.55) is decomposed as

$$\mathbf{u} = \mathbf{q}^* \otimes \mathbf{p} \tag{4.68}$$

where $\mathbf{q}$ is an $N_R \times 1$ column vector expressed as $\mathbf{q} = \left[q_1, q_2, \cdots, q_{N_R}\right]^T$, and $\mathbf{p}$ is an $N_T \times 1$ column vector expressed as $\mathbf{p} = \left[p_1, p_2, \cdots, p_{N_T}\right]^T$. Hence (4.55) could be rewritten as

$$\mathbf{w}_r = \mathbf{v}^* \otimes \mathbf{q}^* \otimes \mathbf{p}\,. \tag{4.69}$$

If $\mathbf{R}_v$ is partitioned into N_R^2 submatrices of dimension $N_T \times N_T$, the optimization problem in (4.61) could be expressed as

$$\mathbf{u}^H \mathbf{R}_v \mathbf{u} = \mathbf{p}^H \left[\sum_{\kappa=1}^{N_R} \sum_{\lambda=1}^{N_R} q_\kappa \mathbf{R}_v^{(\kappa,\lambda)} q_\lambda^* \right] \mathbf{p} \tag{4.70}$$

where $\mathbf{R}_v^{(\kappa,\lambda)}$ is the (κ, λ)-th submatrix of $\mathbf{R}_v$. Next, $\overline{\mathbf{R}}_v$ is defined as

$$\overline{\mathbf{R}}_v\left((\mu-1)N_R+\kappa,(\rho-1)N_R+\lambda\right) = \mathbf{R}_v^*\left((\kappa-1)N_T+\mu,(\lambda-1)N_T+\rho\right) \quad \text{for } \mu,\rho = 1,2,...,N_T \text{ and } \kappa,\lambda = 1,2,...,N_R \,. \tag{4.71}$$

It means that if the $N_T N_R \times N_T N_R$ matrix $\mathbf{R}_v$ is expressed as

$$\mathbf{R}_v = \begin{bmatrix} \mathbf{R}_v^{(1,1)} & \mathbf{R}_v^{(1,2)} & \cdots & \mathbf{R}_v^{(1,N_R-1)} & \mathbf{R}_v^{(1,N_R)} \\ \mathbf{R}_v^{(2,1)} & \cdots & \cdots & \cdots & \mathbf{R}_v^{(2,N_R)} \\ \vdots & \cdots & \mathbf{R}_v^{(\kappa,\lambda)} & \cdots & \vdots \\ \mathbf{R}_v^{(N_R-1,1)} & \cdots & \cdots & \cdots & \mathbf{R}_v^{(N_R-1,N_R)} \\ \mathbf{R}_v^{(N_R,1)} & \mathbf{R}_v^{(N_R,2)} & \cdots & \mathbf{R}_v^{(N_R,N_R-1)} & \mathbf{R}_v^{(N_R,N_R)} \end{bmatrix} \tag{4.72}$$

where the submatrix $\mathbf{R}_v^{(\kappa,\lambda)}$ is an $N_T \times N_T$ matrix given by

$$\mathbf{R}_v^{(\kappa,\lambda)} = \begin{bmatrix} r_{(\kappa-1)N_T+1,(\lambda-1)N_T+1} & r_{(\kappa-1)N_T+1,(\lambda-1)N_T+2} & \cdots & r_{(\kappa-1)N_T+1,(\lambda-1)N_T+N_T} \\ r_{(\kappa-1)N_T+2,(\lambda-1)N_T+1} & r_{(\kappa-1)N_T+2,(\lambda-1)N_T+2} & \cdots & r_{(\kappa-1)N_T+2,(\lambda-1)N_T+N_T} \\ \cdots & \cdots & \cdots & \cdots \\ r_{(\kappa-1)N_T+N_T,(\lambda-1)N_T+2} & r_{(\kappa-1)N_T+N_T,(\lambda-1)N_T+2} & \cdots & r_{(\kappa-1)N_T+N_T,(\lambda-1)N_T+2} \end{bmatrix} \tag{4.73}$$

, then $\overline{\mathbf{R}}_v$ is expressed as

$$\overline{\mathbf{R}}_v = \begin{bmatrix} \overline{\mathbf{R}}_v^{(1,1)} & \overline{\mathbf{R}}_v^{(1,2)} & \cdots & \overline{\mathbf{R}}_v^{(1,N_T-1)} & \overline{\mathbf{R}}_v^{(1,N_T)} \\ \overline{\mathbf{R}}_v^{(2,1)} & \cdots & \cdots & \cdots & \overline{\mathbf{R}}_v^{(2,N_T)} \\ \vdots & \cdots & \overline{\mathbf{R}}_v^{(\mu,\rho)} & \cdots & \vdots \\ \overline{\mathbf{R}}_v^{(N_T-1,1)} & \cdots & \cdots & \cdots & \overline{\mathbf{R}}_v^{(N_T-1,N_T)} \\ \overline{\mathbf{R}}_v^{(N_T,1)} & \overline{\mathbf{R}}_v^{(N_T,2)} & \cdots & \overline{\mathbf{R}}_v^{(N_T,N_T-1)} & \overline{\mathbf{R}}_v^{(N_T,N_T)} \end{bmatrix} \tag{4.74}$$

where $\overline{\mathbf{R}}_v^{(\mu,\rho)}$ is an $N_T \times N_T$ matrix given by

$$\overline{\mathbf{R}}_v^{(\mu,\rho)} = \begin{bmatrix} r_{\mu,\rho} & r_{\mu,N_T+\rho} & \cdots & r_{\mu,(N_R-1)N_T+\rho} \\ r_{N_T+\mu,\rho} & r_{N_T+\mu,N_T+\rho} & \cdots & r_{N_T+\mu,(N_R-1)N_T+\rho} \\ \cdots & \cdots & \cdots & \cdots \\ r_{(N_R-1)N_T+\mu,\rho} & r_{(N_R-1)N_T+\mu,N_T+\rho} & \cdots & r_{(N_R-1)N_T+\mu,(N_R-1)N_T+\rho} \end{bmatrix}^* . \tag{4.75}$$

Therefore, the optimization problem in (4.61) could be expressed as

$$\overline{\mathbf{u}}^H \overline{\mathbf{R}}_v \overline{\mathbf{u}} = \mathbf{q}^H \left[\sum_{\mu=1}^{M} \sum_{\rho=1}^{M} p_\mu \overline{\mathbf{R}}_v^{(\mu,\rho)} p_\rho^* \right] \mathbf{q} \tag{4.76}$$

where $\overline{\mathbf{R}}_v^{(\mu,\rho)}$ is the (μ, ρ)-th submatrix of $\overline{\mathbf{R}}_v$. To simplify the expressions in (4.70) and (4.76), two new matrices are defined as

$$\mathbf{R}_q = \sum_{\kappa=1}^{N}\sum_{\lambda=1}^{N} q_\kappa \mathbf{R}_v^{(\kappa,\lambda)} q_\lambda^* \tag{4.77}$$

$$\mathbf{R}_p = \sum_{\mu=1}^{M}\sum_{\rho=1}^{M} p_\mu \overline{\mathbf{R}}_v^{(\mu,\rho)} p_\rho^* . \tag{4.78}$$

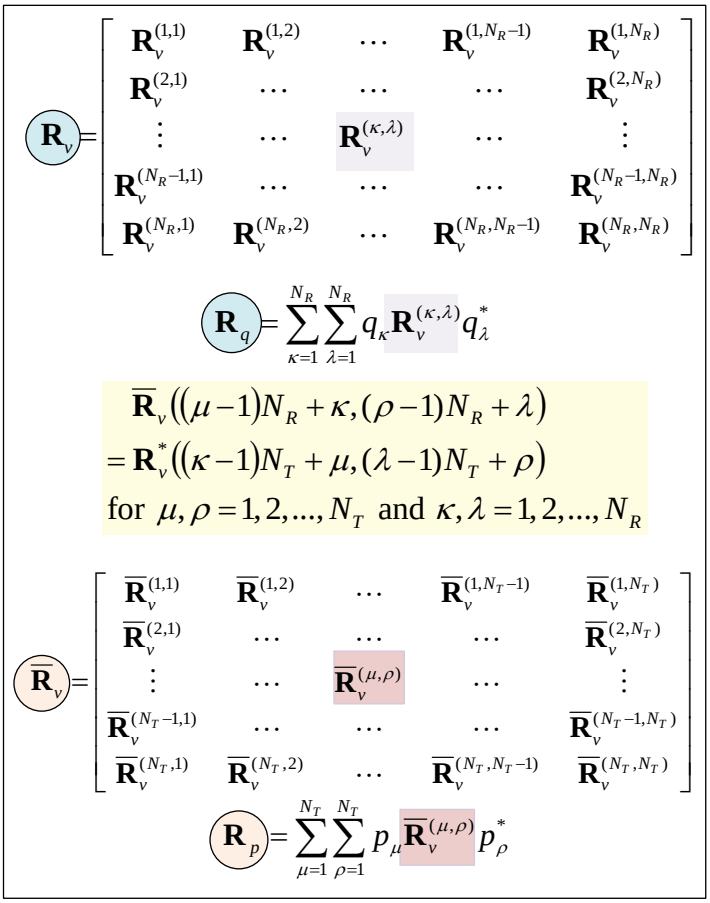

Figure 4.10 The relationship between submatrices.

The relationship between $\mathbf{R}_v$, $\overline{\mathbf{R}}_v$, $\mathbf{R}_q$ and $\mathbf{R}_p$ is depicted in Figure 4.10. The constraint of the optimization problem in (4.61) could be rewritten as

$$
\begin{aligned}
&\mathbf{u}^H \mathbf{A} \mathbf{v} \\
&= (\mathbf{q}^* \otimes \mathbf{p})^H \left[\mathbf{a}_R(\theta_0,\phi_0) \otimes \mathbf{a}_T(\theta_0,\phi_0)\right] \mathbf{a}_D(f_d,\theta_0,\phi_0)^T \mathbf{v} . \\
&= \left[\mathbf{q}^T \mathbf{a}_R(\theta_0,\phi_0)\right]\left[\mathbf{p}^H \mathbf{a}_T(\theta_0,\phi_0)\right] \mathbf{a}_D(f_d,\theta_0,\phi_0)^T \mathbf{v}
\end{aligned} \tag{4.79}
$$

Hence the optimization problem in (4.61) could be decomposed as

$$
\begin{cases}
\min\limits_{\mathbf{p}} \mathbf{p}^H \mathbf{R}_q \mathbf{p} \\
\text{s.t. } \mathbf{p}^H \mathbf{a}_T(\theta_0,\phi_0) = \dfrac{1}{\left[\mathbf{q}^T \mathbf{a}_R(\theta_0,\phi_0)\right]\left[\mathbf{a}_D(f_d,\theta_0,\phi_0)^T \mathbf{v}\right]}
\end{cases} \tag{4.80}
$$

$$
\begin{cases}
\min\limits_{\mathbf{q}} \mathbf{q}^H \mathbf{R}_p \mathbf{q} \\
\text{s.t. } \mathbf{q}^T \mathbf{a}_R(\theta_0,\phi_0) = \dfrac{1}{\left[\mathbf{p}^H \mathbf{a}_T(\theta_0,\phi_0)\right]\left[\mathbf{a}_D(f_d,\theta_0,\phi_0)^T \mathbf{v}\right]}
\end{cases} . \tag{4.81}
$$

The solutions to (4.80) and (4.81) are, respectively,

$$
\mathbf{p} = \alpha_p \mathbf{R}_q^{-1} \mathbf{a}_T(\theta_0,\phi_0) \tag{4.82}
$$

$$
\mathbf{q} = \alpha_q \mathbf{R}_p^{-1} \mathbf{a}_R(\theta_0,\phi_0)^* \tag{4.83}
$$

where constants α_p and α_q are given by

$$
\alpha_p = \frac{1}{\left[\mathbf{q}^T \mathbf{a}_R(\theta_0,\phi_0)\right]\left[\mathbf{a}_D(f_d,\theta_0,\phi_0)^T \mathbf{v}\right]} \tag{4.84}
$$

$$
\alpha_q = \frac{1}{\left[\mathbf{p}^H \mathbf{a}_T(\theta_0,\phi_0)\right]\left[\mathbf{a}_D(f_d,\theta_0,\phi_0)^T \mathbf{v}\right]}. \tag{4.85}
$$

Taking into consideration of (4.62), the weight vector is calculated iteratively as shown in Figure 4.11. Both α_p and α_q are set to be one to maximize the output SINR in (4.32). It could be seen that for iteration step $i = 0$, both the $N_T \times 1$ column vector $\mathbf{p}$ and the $N_R \times 1$ column vector $\mathbf{q}$ are randomly initialized. Then the $M \times 1$ column vector $\mathbf{v}$ is obtained according to (4.65) and (4.68), $\mathbf{p}$ is updated according to (4.82), and $\mathbf{q}$ is

updated according to (4.83). After three iterations (i.e. i = 0, 1, 2), $\mathbf{v}$, $\mathbf{p}$ and $\mathbf{q}$ become stabilized, which are then used to calculate $\mathbf{w}_r$. Since $\mathbf{R}_u$, $\mathbf{R}_p$ and $\mathbf{R}_q$ are $M \times M$, $N_T \times N_T$ and $N_R \times N_R$ matrices, respectively, the computational complexity is greatly reduced than using the $MN_TN_R \times MN_TN_R$ matrix $\mathbf{R}_{I,r}$ directly to calculate the weight vector $\mathbf{w}_r$.

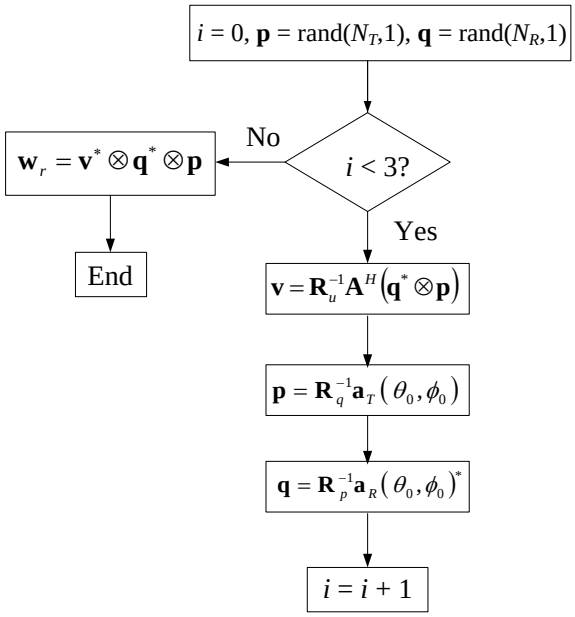

Figure 4.11 Flowchart of the weight vector calculation process (2nd-RSTAP).

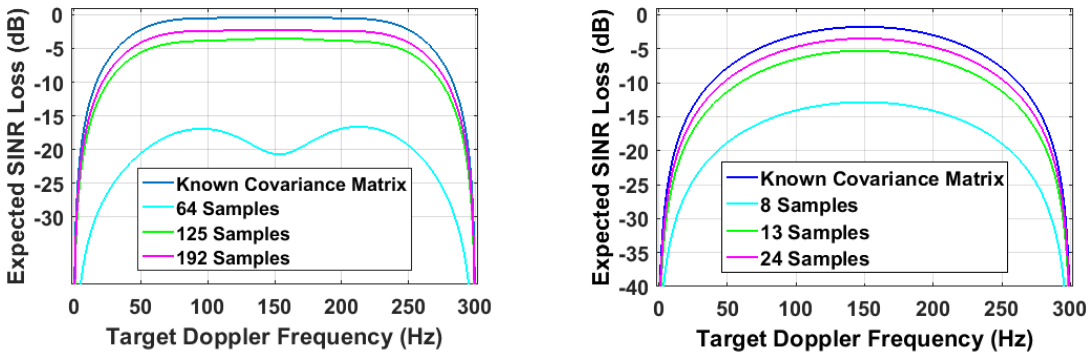

(a) (b)

Figure 4.12 Expected SINR loss for SMI with different number of samples.
(a) 1st-RSTAP; (b) 2nd-RSTAP

The expected SINR loss for SMI with different number of samples is plotted for phased-array radar with MIMO radar with 1st-RSTAP filter and 2nd-RSTAP filter in Figure 4.12 (a) and (b), respectively. It could be seen that a -3 dB loss could be achieved

with $2 \times \max(N_T N_R, M)$ IID samples if 1st-RSTAP filter is used, and that number is reduced to $2 \times \max(N_T, N_R, M)$ if 2nd-RSTAP filter is used.

4.3.3. Simulation results

Table 4.1 Parameters for the airborne radar system and the ground clutter

Symbol	Quantity	Value
f_0	Carrier frequency	450 MHz
d	Inter-element spacing	$\lambda/2$
f_r	Pulse repetition frequency	300 Hz
H	Platform height	9000 m
v_a	Platform speed	50 m/s
SNR	Signal-to-noise ratio	0 dB
CNR	Clutter-to-noise ratio	50 dB
R_{cp}	Clutter Range	130 km

In this section, simulations are carried out to demonstrate (i) the performance of RSTAP in homogeneous clutter; and (ii) the time-effectiveness of RSTAP in inhomogeneous clutter. The parameters for the airborne radar system and the ground clutter used in simulations are summarized in Table 4.1.

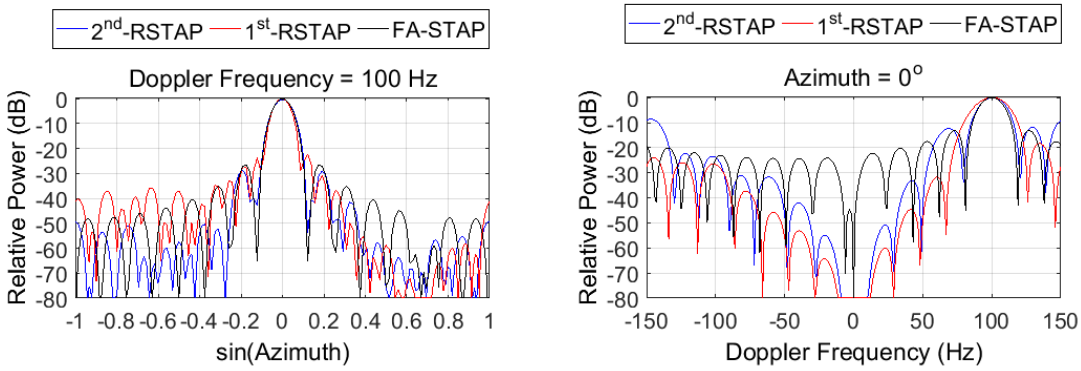

(a) (b)

Figure 4.13 Angle-Doppler response of the MIMO radar.
(a) Principle cut at target Doppler frequency. (b) Principle cut at target azimuth angle.

The principle cuts of the angle-Doppler responses at the target azimuth angle ($\theta_0 = 0^\circ$) and the target Doppler frequency (f_d = 100 Hz) for coherent MIMO radar employing FA-STAP, 1st-RSTAP and 2nd-RSTAP are plotted in Figure 4.13. It is

assumed that $M = N_T = N_R = 16$, and the ground clutter is homogeneous. It is shown in Figure 4.13 (a) and (b) that the gains of the patterns generated by all three STAP methods are maximized at the expected target angle and Doppler frequency, while the clutter signals received from other directions with other Doppler frequencies are suppressed. It means that all three STAP methods have excellent clutter suppression performance in homogeneous clutter when coherent MIMO radar is used. It is shown in Figure 4.13 (a) that the sidelobes of the beampattern generated with 2nd-RSTAP are much lower than those of the beampattern generated with the FA-STAP and 1st-RSTAP. It could also be seen in Figure 4.13 that deeper nulls are generated at zero Doppler with 1st-RSTAP and 2nd-RSTAP than with FA-STAP.

Table 4.2 Matlab execution time to calculate the weight vector with FA-STAP, 1st-RSTAP, and 2nd-RSTAP

Parameters			Matlab Execution Time		
N_T	N_R	M	FA-STAP	1st-RSTAP	2nd-RSTAP
8	8	8	0.087465 seconds	0.160202 seconds	0.144287 seconds
12	12	12	1.931237 seconds	1.146657 seconds	0.711487 seconds
12	12	16	4.151648 seconds	1.961224 seconds	0.933550 seconds
16	16	16	23.073601 seconds	4.035649 seconds	3.164785 seconds

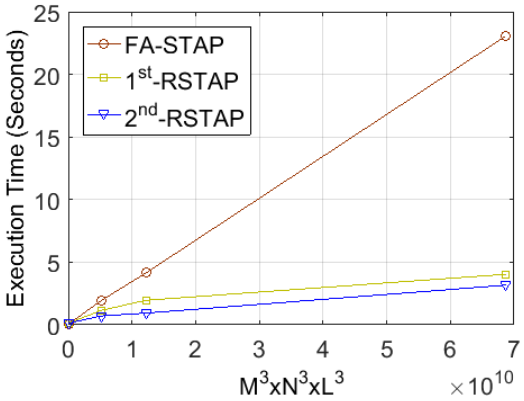

Figure 4.14 Matlab execution time to calculate the weight vector with FA-STAP, 1st-RSTAP and 2nd-RSTAP.

For MIMO radar, when M, N_T and N_R are relatively large, the computational complexity would be dramatically high (i.e. $O(M^3 N_T^3 N_R^3)$) if FA-STAP is used. The time

performances of the FA-STAP, 1st-RSTAP and 2nd-RSTAP for different M, N_T and N_R are summarized in Table 4.2. It is obviously that 1st-RSTAP and 2nd-RSTAP are much more time-efficient than FA-STAP. In order to get a deeper insight into the relationship between the Matlab execution time and the values of M, N_T and N_R, the Matlab execution time of FA-STAP, 1st-RSTAP and 2nd-RSTAP is plotted with respect to $M^3 N_T^3 N_R^3$ in Figure 4.14. It could be seen that the execution time of the FA-STAP is proportional to $M^3 N_T^3 N_R^3$, and both 1st-RSTAP and 2nd-RSTAP are much more time-efficient than FA-STAP.

The SINR performances of different clutter suppression methods for different clutter spectral spread values are plotted in Figure 4.15. It could be seen in Figure 4.15 in (a) and (b) that the output SINR decreases with the spectral heterogeneity when FA-STAP filter is used. It could also be seen that the output SINR for MIMO radar are greater than that for phased-array radar in spectral heterogeneous clutter due to higher DOFs. Comparing Figure 4.15 (c) (d) with (a) (b), it could be seen that although both 1st-RSTAP and 2nd-RSTAP underperform MIMO radar employing FA-STAP, they outperform phased-array radar employing FA-STAP method for most target Doppler frequencies (50 Hz-250 Hz for 1st-RSTAP and 75 Hz-225 Hz for 2nd-RSTAP) when $\sigma_v = 1.2\,\mathrm{m/s}$. It could also be seen in Figure 4.15 (c) and (d) that the SINR performance of 1st-RSTAP is better than that of 2nd-RSTAP, and both of them are quite robust in inhomogeneous clutter.

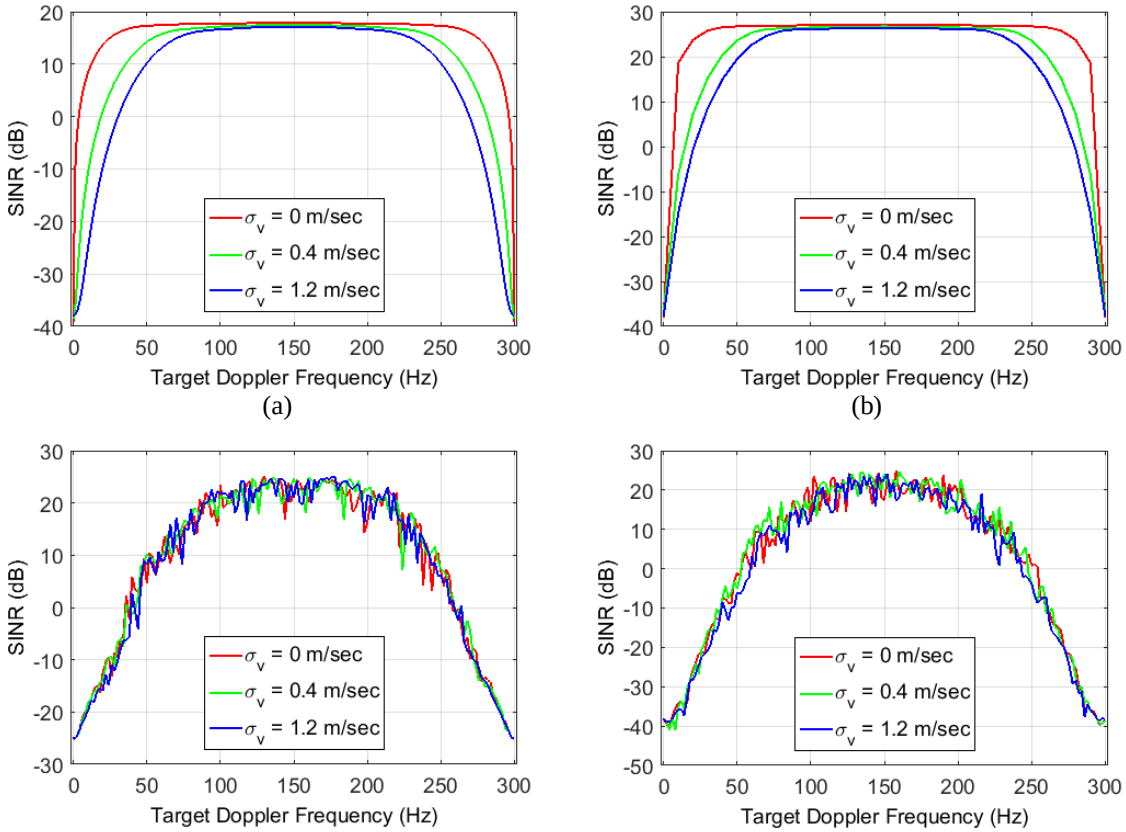

Figure 4.15 SINR performances for different spectral spread values.
(a) Phased-array radar with FA-STAP; (b) MIMO radar with FA-STAP; (c) MIMO radar with 1st-RSTAP
(d) MIMO radar with 2nd-RSTAP

It should be noted that three iterations are assumed for both 1st-RSTAP and 2nd-RSTAP in simulations. The reasons are as following. If fewer numbers of iterations are used, the clutter suppression performance would suffer. Meanwhile, using more than three iterations would not further improve the output SINR performance of the proposed RSTAP method. It could be seen from Figure 4.16 that the performance of the RSTAP method with five iterations is no better than that with three iterations. In addition, if more iterations are used, the time efficiency will suffer since the Matlab execution time is proportional to the number of iterations.

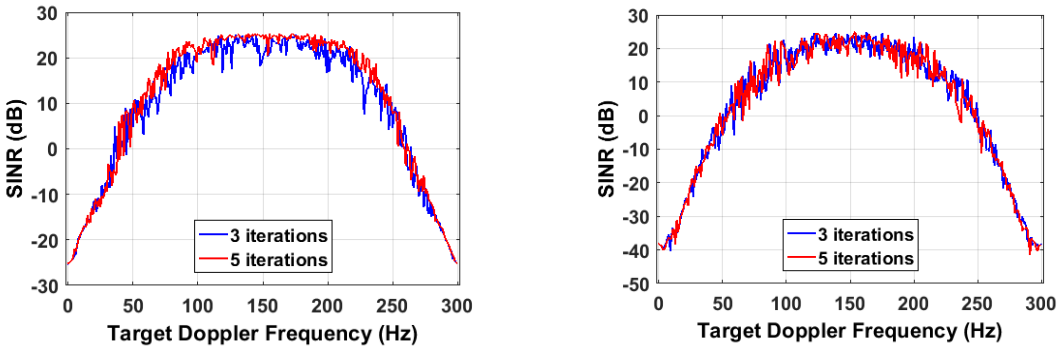

(a) (b)

Figure 4.16 SINR performances for different number of iterations.
(a) MIMO radar with 1st-RSTAP (b) MIMO radar with 2nd-RSTAP.

4.4. Deterministic STAP

This section presents an innovative deterministic STAP (D-STAP) approach for coherent MIMO radar. Unlike stochastic STAP (S-STAP) relying on the auxiliary training data to estimate the statistics of the interference and place nulls for interference suppression, D-STAP operates on a snapshot-by-snapshot basis to determine the adaptive weights. However, in order for traditional D-STAP (T-D-STAP) to achieve a satisfactory performance, the assumed target DOA has to match the real one perfectly. Therefore, a robust D-STAP approach termed as R-D-STAP is proposed in the following, which provides near-optimum target detection and clutter suppression performance when there is a mismatch between the assumed target DOA and the true target DOA.

4.4.1. R-D-STAP for MIMO radar

Assume that the signal received at the *n*-th antenna element transmitted from the *v* -th antenna element during the *m*-th pulse is expressed as $x_{n,v,m}$. The offsets for different pulses, transmit waveforms and receive antennas are expressed, respectively, as

$$z_M = e^{j2\pi f_d T} \tag{4.86}$$

$$z_T = e^{j2\pi \frac{d_T \sin\theta_0}{\lambda}} \tag{4.87}$$

$$z_R = e^{j2\pi \frac{d_R \sin\theta_0}{\lambda}} \quad . \tag{4.88}$$

Assume that $\left(K_{N_T} K_{N_R}\right)$ and K_M are the number of degrees of freedoms (DOFs) in spatial domain and temporal domain, respectively. By defining the deterministic data cube, $\mathbf{x}_{K_{N_R} K_{N_T} K_M}$, as the received radar signal of the first K_{N_R} antennas transmitted from the first K_{N_T} antennas during the first K_M pulses, seven row vectors ($\mathbf{y}_1$, $\mathbf{y}_2$, $\mathbf{y}_3$, $\mathbf{y}_4$, $\mathbf{y}_5$, $\mathbf{y}_6$ and $\mathbf{y}_7$) of dimension $K_{N_T} K_{N_R} K_M$ which contain only interference signals could be formulated as:

$$\mathbf{y}_1\left((m-1)K_{N_T} K_{N_R} + (n-1)K_{N_T} + \nu\right) = x_{n,\nu,m} - z_M^{-1} x_{n,\nu,m+1} \tag{4.89}$$

$$\mathbf{y}_2\left((m-1)K_{N_T} K_{N_R} + (n-1)K_{N_T} + \nu\right) = x_{n,\nu,m} - z_T^{-1} x_{n,\nu+1,m} \tag{4.90}$$

$$\mathbf{y}_3\left((m-1)K_{N_T} K_{N_R} + (n-1)K_{N_T} + \nu\right) = x_{n,\nu,m} - z_R^{-1} x_{n+1,\nu,m} \tag{4.91}$$

$$\mathbf{y}_4\left((m-1)K_{N_T} K_{N_R} + (n-1)K_{N_T} + \nu\right) = x_{n,\nu,m} - z_T^{-1} z_M^{-1} x_{n,\nu+1,m+1} \tag{4.92}$$

$$\mathbf{y}_5\left((m-1)K_{N_T} K_{N_R} + (n-1)K_{N_T} + \nu\right) = x_{n,\nu,m} - z_R^{-1} z_M^{-1} x_{n+1,\nu,m+1} \tag{4.93}$$

$$\mathbf{y}_6\left((m-1)K_{N_T} K_{N_R} + (n-1)K_{N_T} + \nu\right) = x_{n,\nu,m} - z_R^{-1} z_T^{-1} x_{n+1,\nu+1,m} \tag{4.94}$$

$$\mathbf{y}_7\left((m-1)K_{N_T} K_{N_R} + (n-1)K_{N_T} + \nu\right) = x_{n,\nu,m} - z_R^{-1} z_T^{-1} z_M^{-1} x_{n+1,\nu+1,m+1}\,. \tag{4.95}$$

where $n = 1, 2, \cdots, K_{N_R}; \nu = 1, 2, \cdots, K_{N_T}; m = 1, 2, \cdots, K_M$. These interference vectors can be arranged as rows in a $7 \times K_{N_T} K_{N_R} K_M$ linear system matrix $\mathbf{F}_2$, which is expressed as

$$\mathbf{F}_2 = \begin{bmatrix} \mathbf{y}_1^T & \mathbf{y}_2^T & \cdots & \mathbf{y}_7^T \end{bmatrix}^T. \tag{4.96}$$

In the following, a $K_{N_T}K_{N_R}K_M$ weighting vector of dimension is designed to null the interference vectors. In order to prevent the self-nulling (cancellation of the target signal), one extra row is added to the matrix $\mathbf{F}_2$, to play the role of the main beam look direction constraint vector. This row vector $\mathbf{y}_0$ is expressed as

$$\mathbf{y}_0 = \left[1\ z_M \cdots z_M^{K_M-1}\right] \otimes \left[1\ z_R \cdots z_R^{K_{N_R}-1}\right] \otimes \left[1\ z_T \cdots z_T^{K_{N_T}-1}\right]. \tag{4.97}$$

And the $8 \times K_{N_T}K_{N_R}K_M$ matrix $\mathbf{F}$ is obtained as

$$\mathbf{F} = \left[\mathbf{y}_0^T \quad \mathbf{y}_1^T \quad \cdots \quad \mathbf{y}_8^T\right]. \tag{4.98}$$

The weight vector of the deterministic STAP for MIMO radar could be obtained by solving the following linear system

$$\mathbf{F}\mathbf{w}_d = \mathbf{q} = \left[q_1\ q_2 \cdots q_8\right]^T \tag{4.99}$$

where $\mathbf{w}_d$ is the weight vector and q_1 stands for the main beam look direction constraint. In order to null the interferences while preserving the target signal, q_1 has to be as close to 1 as possible, and q_2, q_3 … q_8 have to be approximately zero. In conventional deterministic STAP, it is assumed that the nominal target parameters perfectly match the real ones, and (4.99) is simplified as

$$\mathbf{F}\mathbf{w}_d = \left[1 \quad 0 \quad 0 \quad 0 \quad 0 \quad 0 \quad 0 \quad 0\right]^T. \tag{4.100}$$

However, when there is a mismatch between the assumed target DOA and the real one, the interference vectors could contain contribution from the target, and target "self-nulling" could occur. Assume that θ_e and f_e are the errors in the prior knowledge of target DOA and target Doppler, respectively. The error vector $\mathbf{e}$ is defined as

$$\mathbf{e} = \left[1\ z_{e,M} \cdots z_{e,M}^{K_M-1}\right]^T \otimes \left[1\ z_{e,R} \cdots z_{e,R}^{K_{N_R}-1}\right]^T \otimes \left[1\ z_{e,T} \cdots z_{e,T}^{K_{N_T}-1}\right]^T \tag{4.101}$$

where $z_{e,M}$, $z_{e,R}$, and $z_{e,T}$ are, respectively, expressed as

$$z_{e,M} = e^{j2\pi f_e M} \tag{4.102}$$

$$z_{e,R} = e^{j2\pi \frac{d_R \sin\theta_e}{\lambda}} \tag{4.103}$$

$$z_{e,T} = e^{j2\pi \frac{d_T \sin\theta_e}{\lambda}}. \tag{4.104}$$

The main beam look direction constraint row vector is modified as

$$\mathbf{y}_{0,N} = \left\{z_{e,M}^{-1}\left[1\ z_M \cdots z_M^{K_M-1}\right]\right\} \otimes \left\{z_{e,R}^{-1}\left[1\ z_R \cdots z_R^{K_{N_R}-1}\right]\right\} \otimes \left\{z_{e,T}^{-1}\left[1\ z_T \cdots z_T^{K_{N_T}-1}\right]\right\}. \tag{4.105}$$

And the convex optimization problem is formulated as

$$\begin{cases} \min\limits_{\mathbf{w}} \left\|\mathbf{F}_2^* \mathbf{w}_d\right\| \\ \text{s.t.}\, \mathbf{w}_d^H \mathbf{y}_{0,N}^T = 1 \end{cases}. \tag{4.106}$$

where $\|\cdot\|$ represents the norm and * represents the conjugate. The convex optimization problem in (4.106) could be solved easily with the Matlab CVX toolbox provided in [74]. Finally, the target signal complex amplitude, α, is estimated as

$$\hat{\alpha} = \mathbf{w}_d^H \mathbf{x}_{K_M K_{N_T} K_{N_R}} \tag{4.107}$$

With deterministic STAP, the number of DOFs for interference suppression is $K_M K_{N_T} K_{N_R} - 1$, while in stochastic STAP, the number of DOFs for interference suppression is MN_TN_R. It is easy to obtain that

$$K_M K_{N_T} K_{N_R} - 1 < MN_T N_R \tag{4.108}$$

It could be seen that although deterministic STAP filter outperforms stochastic STAP filter in inhomogeneous clutter by operating on a snapshot-by-snapshot basis, the number of available DOFs is reduced as a trade-off.

4.4.2. R-D-STAP for phased-array radar

It should be noted that a robust deterministic STAP filter could also be derived for phased-array radar in a very similar way. Assume that the numbers of antenna elements and pulses per CPI are *N* and *M*, respectively, the number of DOFs in spatial and temporal domain is K_N and K_M, respectively, and the signal received at the *n*-th antenna element during the *m*-th pulse is expressed as $x_{n,m}$. In this case, three $1\times K_M K_N$ row vectors containing only the interference could be obtained:

$$\mathbf{y}_{p,1}\left((m-1)K_N+n\right)=x_{n,m}-z_M^{-1}x_{n,m+1} \tag{4.109}$$

$$\mathbf{y}_{p,2}\left((m-1)K_N+n\right)=x_{n,m}-z_N^{-1}x_{n+1,m} \tag{4.110}$$

$$\mathbf{y}_{p,3}\left((m-1)K_N+n\right)=x_{n,m}-z_M^{-1}z_N^{-1}x_{n+1,m+1} \tag{4.111}$$

where $z_{P,M}$ and $z_{P,N}$ are the offsets for different pulses and antennas, respectively, and $n=1,2,\cdots,K_N; m=1,\cdots,K_M$. Hence the interference matrix $\mathbf{F}_2$ only has three rows for phased-array radar while it has seven rows for MIMO radar. And a $K_N K_M\times 1$ weighting vector could be designed to null these interference vectors by solving the optimization problem in (4.106) after modifying the constraint vector accordingly.

4.4.3. Simulation results

In this section, simulations are carried out to demonstrate the performance of the proposed R-D-STAP filter in inhomogeneous clutter. Specifically, two different types of clutter heterogeneity are considered: spectral heterogeneity and amplitude heterogeneity. The performance of the R-D-STAP filter is compared with the S-STAP filter (Capon filter) and the T-D-STAP filter based on the output SINR and the angle-Doppler

responses. For all three types of filters, both phased-array radar and coherent MIMO radar are considered. The parameters for the airborne radar system and the ground clutter are the same as the ones shown in Table 4.1.

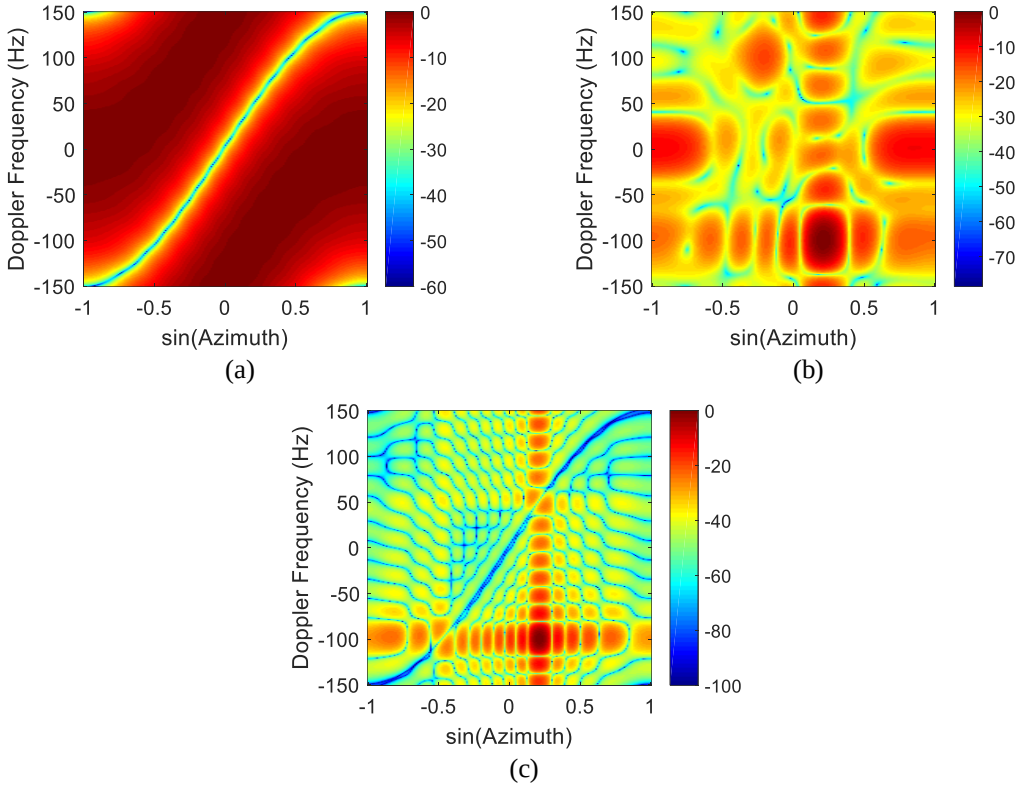

Figure 4.17 2D angle-Doppler responses of the space-time snapshot of radar data in homogeneous clutter.
(a) T-D-STAP (b) R-D-STAP (c) S-STAP

The 2D angle-Doppler responses of the space-time snapshot of radar data in homogeneous clutter when the S-STAP filter, the R-D-STAP filter and the S-STAP filter are applied to the receiver of phased-array radar are plotted in Figure 4.17 (a), (b) and (c), respectively. It could be seen in Figure 4.17 (a) that when T-D-STAP filter is used, deep nulls are formed at the clutter ridges to suppress clutter signals in both plots. However, these patterns are not suitable for noise processing since the noise signals at most angles and Doppler frequencies (except for the ones located at the clutter ridge) are strengthened

together with the target signal. Hence the performance of the T-D-STAP filter is unstable and highly dependent on the random noise signal.

When R-D-STAP filter is used, it could be seen in Figure 4.17 (b) that the gains of both patterns are maximized at the expected target angle and Doppler frequency. Meanwhile, the interferences in other angles and at other Doppler frequencies are suppressed. Comparing Figure 4.17 (b) and Figure 4.17 (c), it could be seen that the performance of the S-STAP filter is better than the R-D-STAP filter in homogeneous clutter. It is consistent with the fact that in this case more DOFs are available in S-STAP filter than in D-STAP filter. However, it should be noted that D-STAP operates on a snapshot-by-snapshot basis and it doesn't need covariance matrix estimation. Hence the R-D-STAP filter outperforms the S-STAP filter when the ground clutter is highly inhomogeneous.

The 2D angle-Doppler responses of the space-time snapshot of radar data in homogeneous clutter when the S-STAP filter, the R-D-STAP filter and the S-STAP filter are applied to the receiver of MIMO radar are plotted in are shown in Figure 4.18 (a), (b) and (c), respectively. 16 transmit/receive antenna elements and 16 pulses per CPI are assumed. It could be seen in Figure 4.18 (b) and Figure 4.18 (c) that when the R-D-STAP filter and the S-STAP filter are used in MIMO radar, deeper nulls are generated than the case when they are used in phased-array radar (refer to Figure 4.18 (b) and (c)). This is due to the fact that the MIMO radar has higher DOFs than phased-array radar. However, comparing Figure 4.18 (a) and Figure 4.17 (a), it could be seen that the performance of the T-D-STAP filter doesn't improve with the increased DOFs. This is another demonstration that the R-D-STAP filter outperforms the T-D-STAP filter.

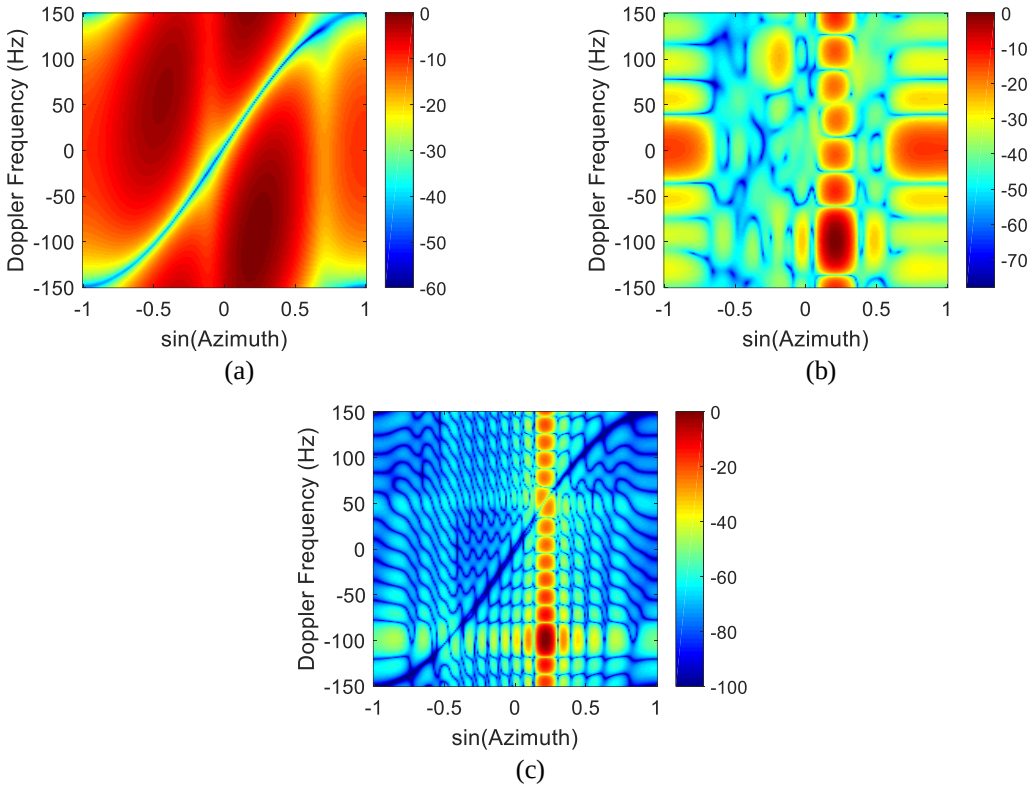

Figure 4.18 2D angle-Doppler responses of the space-time snapshot of radar data in homogeneous clutter when STAP filters are applied to the receiver of MIMO radar.
(a) T-D-STAP (b) R-D-STAP (c) S-STAP

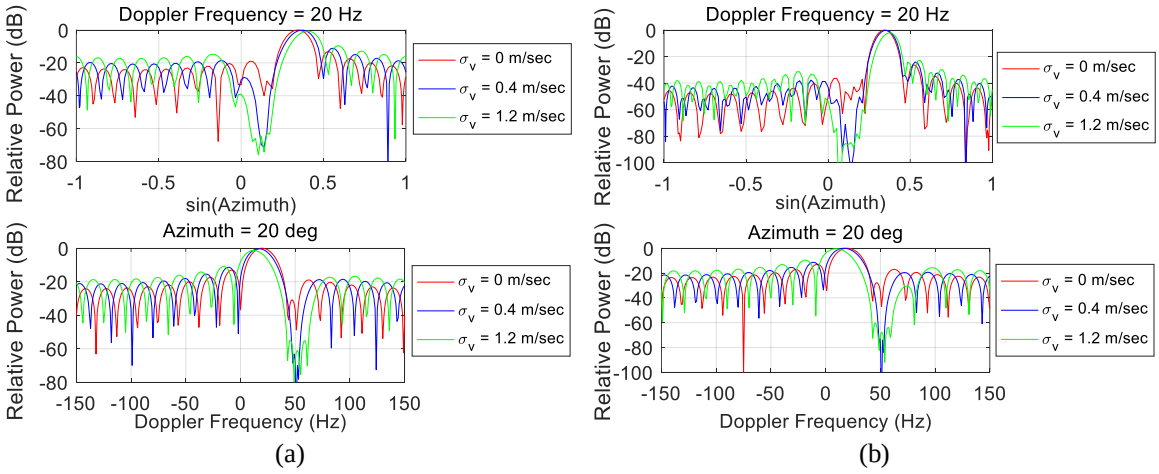

Figure 4.19 Angle-Doppler responses when S-STAP is used.
(a) phased-array radar; (b) MIMO radar

The principle cuts of the angle-Doppler response at target azimuth and Doppler for different spectral spread values when S-STAP filter is used for phased-array radar and

MIMO radar are plotted in Figure 4.19 (a) and (b), respectively, under the assumption of a target Doppler of 20 Hz and a target azimuth of 20°. It could be seen that the maximum gain of the azimuth pattern at the expected target Doppler (above) and the Doppler resonse at the target azimuth (below) deviate more and more from the expected target and Doppler with the increase of σ_v. Compare Figure 4.19 (b) with Figure 4.19 (a), it could be seen that deeper nulls are formed for clutter suppression with MIMO radar due to the increased DOF. However, similar "pattern deviation" phenomena are observed with the increase of σ_v. It means that for both phased-array radar and MIMO radar, the maximum antenna gain is not achieved at the expected target and Doppler in highly inhomogeneous clutter, hence the detection probability would suffer.

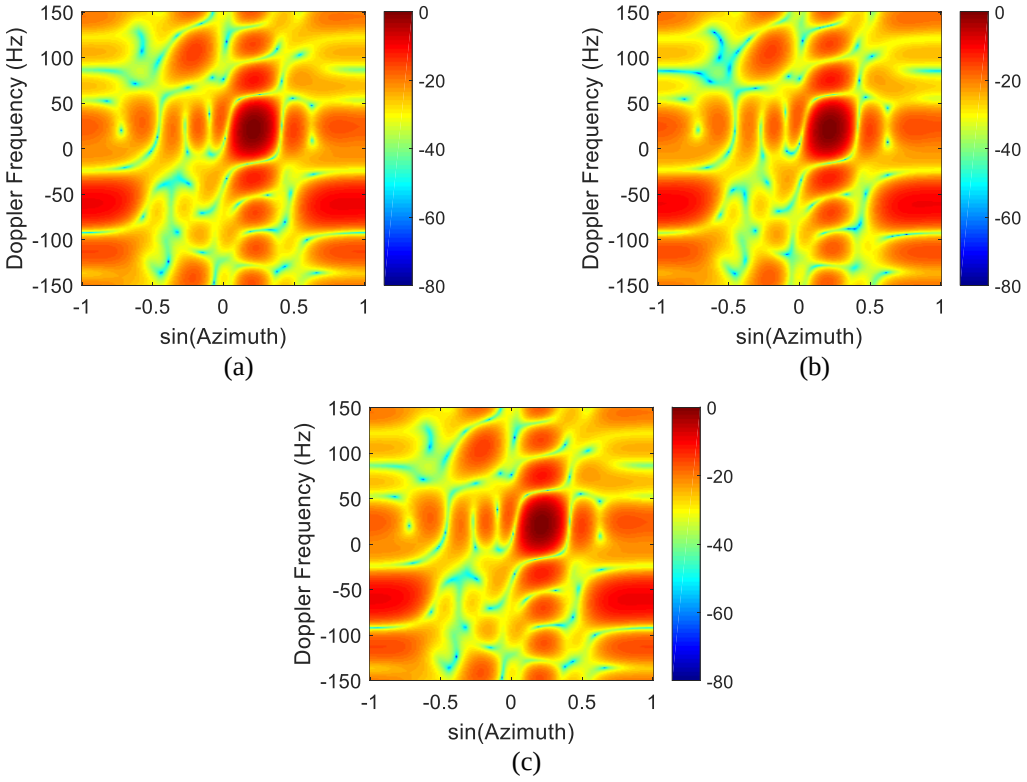

Figure 4.20 2D angle-Doppler responses of the space-time snapshot of radar data in spectrally heterogeneous clutter when R-D-STAP is applied to the receiver of phased-array radar. (a) σ_v = 0 m/s. (b) σ_v = 0.4 m/s. (c) σ_v = 1.2 m/s.

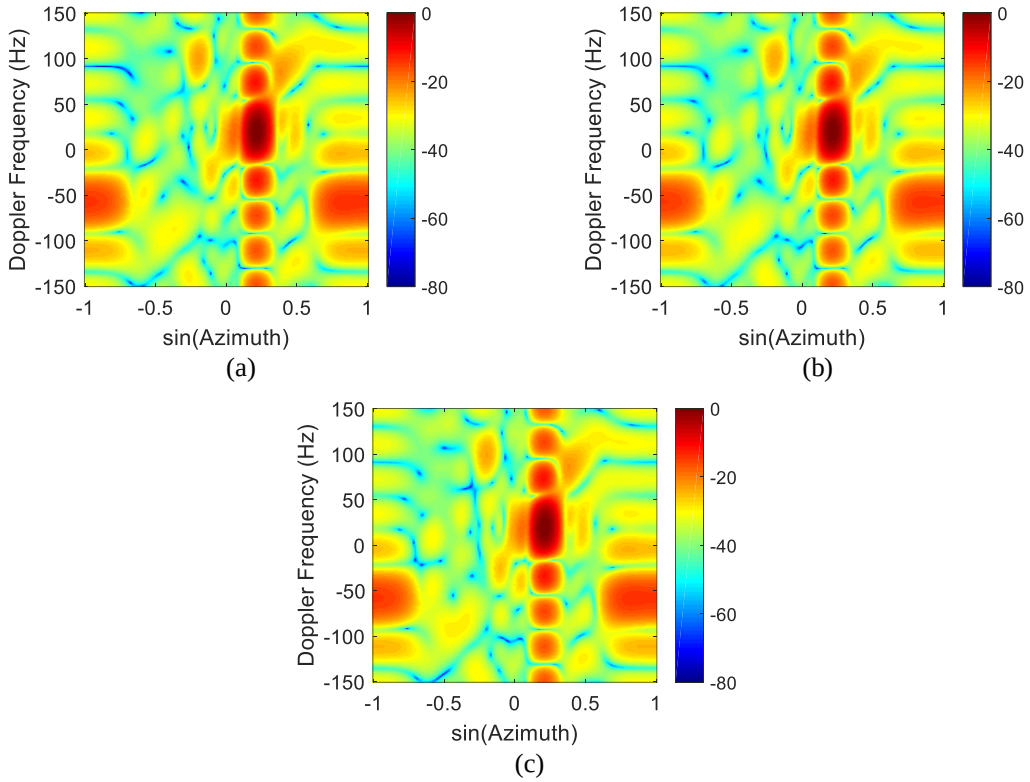

Figure 4.21 2D angle-Doppler responses of the space-time snapshot of radar data in spectrally heterogeneous clutter when R-D-STAP is applied to the receiver of MIMO radar. (a) σ_v = 0 m/s. (b) σ_v = 0.4 m/s. (c) σ_v = 1.2 m/s.

The 2D angle-Doppler responses of the space-time snapshot of radar data in spectrally heterogeneous clutter when R-D-STAP is applied to the receiver of phased-array radar are plotted for $\sigma_v = 0\,\text{m/s}$, $\sigma_v = 0.4\,\text{m/s}$ and $\sigma_v = 1.2\,\text{m/s}$ in Figure 4.20 (a), (b) and (c), respectively, under the assumption of a target Doppler of 20 Hz and a target azimuth of 20°. It is shown in Figure 4.20 that neither the azimuth patterns nor the Doppler frequency change with spectral heterogeneity and the maximum gain is always achieved at the expected target azimuth and Doppler. For the purpose of comparison, the 2D angle-Doppler responses of radar data when R-D-STAP is applied to the receiver of MIMO radar are plotted in Figure 4.21. Comparing Figure 4.21 and Figure 4.20, it could be seen that MIMO radar has better clutter suppression and target detection performance.

The principle cuts of angle-Doppler responses of the space-time snapshot of radar data in spectrally heterogeneous clutter when R-D-STAP is applied are plotted in Figure 4.22. It is assumed that the expected target azimuth and Doppler are 20° and 20 Hz, respectively. It could be seen in Figure 4.22 that neither the azimuth patterns nor the Doppler frequency change with spectral heterogeneity and the maximum gain is always achieved at the expected target azimuth and Doppler. Compare Figure 4.22 (b) and Figure 4.22 (a), it could be seen that the sidelobes are lower when MIMO radar is used due to the higher DOF.

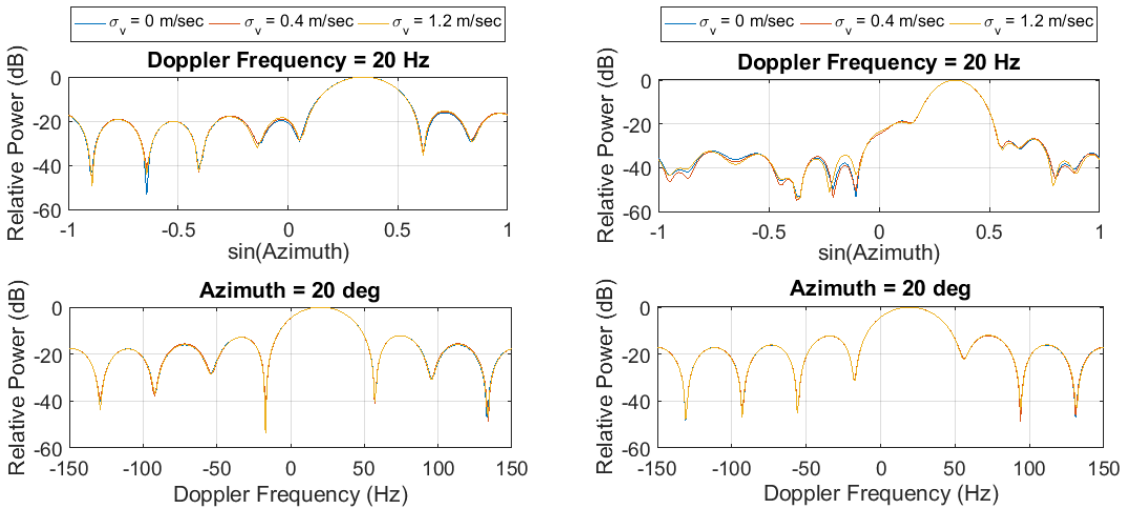

Figure 4.22 Principle cuts of angle-Doppler responses when R-D-STAP is applied.
(a) Phased-array radar (b) MIMO radar

Assume that SINR loss due to limited IID sample support is -3dB, the SINR losses due to varying degrees of clutter amplitude heterogeneity are summarized in Table 4.3. It is assumed that $\theta_0 = 20^\circ$, $f_d = 20$ Hz . The results are obtained with the following steps:

a. Randomly select the clutter reflectivity for each clutter patch from the gamma distribution with given parameters $\tilde{\alpha}$ and $\tilde{\beta}$. Compute and store the interference covariance matrix $\mathbf{R}_r$.

b. Set $M = N_T = N_R = 8$. For phased-array radar, compute $2MN_TN_R = 1024$ realizations by selecting the clutter reflectivity for each clutter patch from the same gamma distribution. For phased-array radar, compute $2MN = 128$ realizations. Estimate the interference covariance matrix $\hat{\mathbf{R}}_r$ using the MLE.

c. Compute two adaptive weight vectors $\mathbf{w}_r$ and $\hat{\mathbf{w}}_r$ using $\mathbf{R}_r$ and $\hat{\mathbf{R}}_r$, respectively.

d. Compute the SINR loss.

e. Carry out 50 Monte Carlo trials and calculate the average SINR loss.

It could be seen in Table 4.3 that since the expected target is far from the clutter ridge, the SINR losses are very small for both phased-array radar and MIMO radar and could be ignored.

Table 4.3 SINR loss due to range-angle variation of clutter reflectivity when S-STAP filter is used. ($M = N_T = N_R = 8$, $\tilde{\beta} = 10$)

	$\tilde{\alpha}$	0.005	0.01	0.03	0.5	0.1	0.5
SINR Loss (dB)	Phased-array Radar	-4.42	-3.76	-3.16	-3.00	-3.00	-3.00
	MIMO Radar	-3.62	-3.33	-3.02	-3.00	-3.00	-3.00

The SINR loss due to varying degrees of clutter amplitude heterogeneity with phased-array radar and MIMO radar is summarized in Table 4.4. It is assumed that the expected target azimuth and Doppler are 20° and 20 Hz, respectively. The average SINR losses in Table 4.4 are calculated based on 50 Monte Carlo trials. It could be seen that the

SINR losses are less than -3 dB for all cases of clutter amplitude heterogeneity when the nominal target DOA perfectly matches the actual target DOA.

Table 4.4 SINR loss due to range-angle variation of the clutter reflectivity when R-D-STAP filter is used

	$\widetilde{\alpha}$	0.005	0.01	0.03	0.5	0.1	0.5
SINR loss (dB)	Phased-array radar	-1.40	-2.04	-1.00	-0.97	-1.93	-2.36
	MIMO radar	-1.96	-2.89	-1.42	-1.88	-1.73	-1.95

In the following, the relationship between the SINR and the SCR will be analyzed and non-homogeneous clutter is assumed. The simulation result in [75] shown that the phased-MIMO radar outperforms MIMO radar in SINR-CNR plot, it is not convincing since there are problems with the definition of SINR. In [75], the SINR is defined as

$$SINR = 20\log\left|\frac{\alpha}{\alpha-\hat{\alpha}}\right| \tag{4.112}$$

where $\hat{\alpha}$ is the estimated target amplitude. Unfortunately, this expression doesn't have a proper upper bound, i.e. the maximum SINR is infinity. And it is well known that the maximum SINR improvement of phased-array radar and MIMO radar that could be achieved are $10\times\log10(MN)$ and $10\times\log10(MN_TN_R)$, respectively. To encounter this problem, in this section, the SINR for S-STAP is calculated as:

$$SINR = 10\log10\left(\frac{\left|\alpha\mathbf{w}^H\mathbf{a}\left(f_d,\theta_0,\phi_0\right)\right|^2}{\sum_{k=1}^{N_c}\left|\alpha_k\mathbf{w}_r^H\mathbf{a}\left(\vartheta_{r,k},\theta_{r,k},\phi_r\right)\right|^2+\left|\mathbf{w}_r^H\mathbf{x}_n\right|^2}\right) \tag{4.113}$$

The SINR for D-STAP is in similar form except for using the $K_M K_{N_T} K_{N_R}$ truncated version of $\mathbf{w}_r$, $\mathbf{a}\left(f_d,\theta_0,\phi_0\right)$ and $\mathbf{x}_n$ (recall that the deterministic data cube, $\mathbf{x}_{K_M K_{N_T} K_{N_R}}$, is defined as the received radar signal of the first K_{N_R} antennas transmitted from the first

K_{N_T} antennas during the first K_M pulses). Since $\left|\mathbf{w}_r^H \mathbf{x}_n\right|^2 \approx 1$, even if the clutter signals are nulled perfectly, i.e. $\sum_{k=1}^{N_c} \left|\alpha_k \mathbf{w}_r^H \mathbf{a}\left(\vartheta_{r,k}, \theta_{r,k}, \phi_r\right)\right|^2 \approx 0$, the SINR is still well bounded instead of approaching infinity.

The relationship between the SINR and the SCR is plotted in Figure 4.23. Four cases are considered: (i) phased-array radar ($M = N = 8$); (ii) phased-array radar ($M = N = 16$); (iii) MIMO radar ($M = N_T = N_R = 8$); (iv) MIMO radar ($M = N_T = N_R = 16$). All the SINR values are obtained by Monte-Carlo simulation with 100 trials and the average of the trials are recorded. It could be seen from Table 4.4 and Figure 4.23 that the output SINR performance of MIMO radar ($M = N_T = N_R = 8$) is basically the same as that of the phased-array radar ($M = N = 16$). It means that MIMO radar is capable of achieving much higher output SINR than phased-array radar with much smaller number of antenna elements and pulses per CPI.

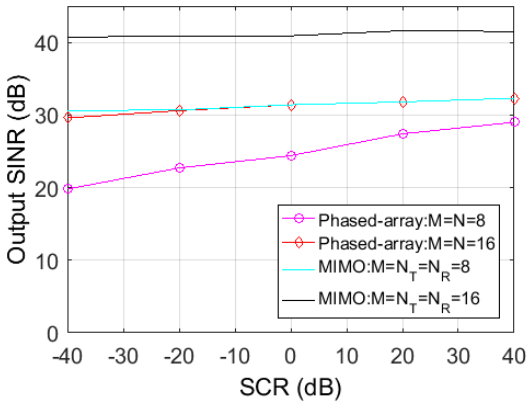

Figure 4.23 The relationship between the SINR and the SCR.

The following analysis is devoted to the relationship between the output SINR and the difference between the nominal and the true target DOA. Both phased-array radar

and MIMO radar are considered, and highly inhomogeneous clutter is assumed. The output SINR values for different mismatch angles between the nominal and the true target DOA when robust deterministic STAP filter is plotted in Figure 4.24. Four cases are considered: (i) phased-array radar with $M = N = 8$; (ii) phased-array radar with $M = N = 16$; (iii) MIMO radar with $M = N_T = N_R = 8$; (iv) MIMO radar with $M = N_T = N_R = 16$. It could be seen that for both phased-array radar and MIMO radar, when the target DOA mismatch is large, the output SINR is higher when smaller number of antenna elements and pulses per CPI are assumed. However, when the target DOA mismatch is relatively small, the radar system with more antenna elements and pulses per CPI has higher output SINR. It could be seen that although the phased-array radar is more robust to target DOA mismatches, the output SINR performance of MIMO radar is much better than that of the phased array radar when the mismatch angle is relatively small.

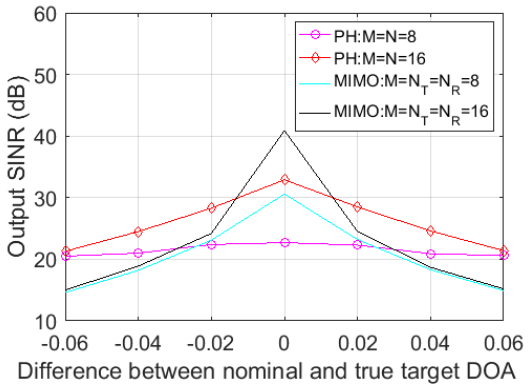

Figure 4.24 The SINR loss due to the difference between the nominal and true target DOA.

4.5. Summary of Chapter 4

In this chapter, two innovative ground clutter suppression approaches termed as RSTAP and R-D-STAP are proposed for airborne MIMO radar ground moving target detection in inhomogeneous clutter. In RSTAP, the high dimensional weight vector is

calculated iteratively with lower dimensional weight vectors, hence the computational complexity is reduced dramatically. In contrast, R-D-STAP operates on a snapshot-by-snapshot basis to determine the adaptive weights and can be readily implemented in real time. The performances of RSTAP and R-D-STAP in inhomogeneous clutter are compared with those of FA-STAP by plotting the angle-Doppler responses and output SINR. The following conclusions are drawn by observing the simulation results.

1) Even though FA-STAP has a slightly better output SINR performance, the proposed RSTAP method has an outstanding advantage in the processing time when the number of antenna elements and the number of pulses per CPI are relatively large. For example, when $M = N_T = N_R = 16$, it takes 23s to calculate the adaptive weight vector if FA-STAP used, while it takes only 4s if 1st RSTAP is used and 3s if 2nd RSTAP is used.

2) The performance of FA-STAP degrades dramatically with the increase of the clutter spectral heterogeneity, while the performance of RSTAP is quite robust.

3) R-D-STAP filter outperforms the FA-STAP when spectral clutter heterogeneity is present since it operates on snapshot-to-snapshot basis and the estimation of the clutter covariance matrix is unnecessary.

4) When amplitude heterogeneity due to range-angle variation of clutter reflectivity is the dominant problem, both the FA-STAP filter and the R-D-STAP filter have good performances given that the target is not on the clutter ridge.

5) When the R-D-STAP is applied to both types of radar systems, the performance of MIMO radar is much better than that of the phased array radar when the mismatch angle is relatively small.

5. MIMO RADAR ADAPTIVE BEAMFORMING FOR INTERFERENCE MITIGATION

Traditionally, certain licensed spectrum is intended to be used only by radars. Specifically, in USA, S-band (2 GHz – 4 GHz) radars have primary spectrum allocation status throughout 2310-2385 MHz, 2700-3100 MHz and 3100-3650 MHz [76]. Since typical radar operations only use these exclusively licensed spectrum occasionally, large portions of these frequency bands are underutilized for most of the time [77]. However, it is essential for radars to maintain access to these spectrum, and even gain secondary access to more spectrum currently licensed to other radio systems, in order to achieve mission success in the face of competition for spectrum access from adversaries [78]. On the other hand, wireless industry's demand for spectrum keeps increasing in pursuit of providing higher data rates to higher densities of users beyond the capability of current networks in the upcoming 5G communication era. Therefore, both radar and communication systems will benefit if they could operate in the same spectrum band simultaneously without compromising the performances of each other.

In order to achieve this goal, the Department of Defense and the Department of Commerce are partnering in a collaborative framework to make spectrum sharing possible through the Shared Spectrum Access for Radar and Communications (SSPARC) program of Defense Advanced Research Projects Agency (DARPA) [79]. However, making the spectrum sharing between radar and wireless commercial/military communications systems technically feasible without compromising both systems' performances is no easy task.

The first line of research has been focused on designing a joint radar-communication (JRC) system, which has both the radar sensing and the communication abilities. Joint orthogonal frequency division multiplexing (OFDM) radar-communication systems are proposed in [80-87], where the OFDM signals are used for both radar sensing and wireless communication. Amplitude Modulation (AM) based dual-function radar communications (DFRC) systems are proposed in [88-91], where multiple orthogonal waveforms are used to embed the information to be transmitted, and the power levels of the radar sidelobes towards the communication directions are used to embed communication symbols. Phase Modulation (PM) and Phase-Shift Keying (PSK) based DFRC system are proposed in [91-94], where communication symbols are embedded in the phase difference between orthogonal transmit waveform pairs.

Another line of research has been concentrating on interference mitigation for either radar or wireless communication system under the assumption of a spectrum sharing scenario. In [95-98], the radar waveforms are projected onto the null space of the interference channel between the MIMO radar and the communication system, constraining radar interference to the communication system while assuring minimum degradation in the radar detection performance. In [99] and [100], the spectrum sharing problem is formulated as a constrained optimization problem---the radar transmit waveform is designed to maximize the output SINR of radar system, while at the same time constraining the interfering energy on wireless systems from radar. In [101], a wireless communication network capable of mitigating interference form radar is proposed.

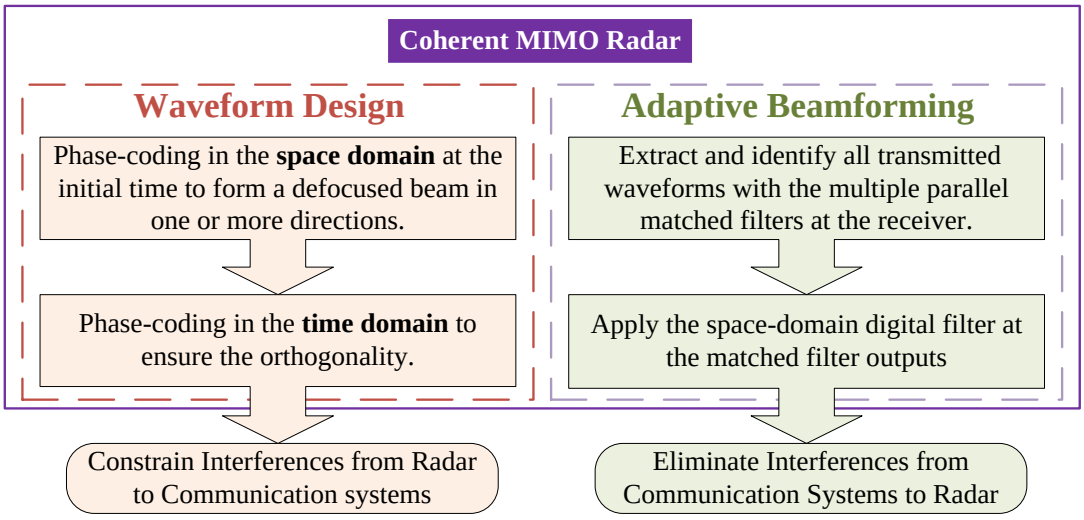

Figure 5.1 Flowchart of coherent MIMO radar waveform design and adaptive beamforming to enable spectrum sharing between radar and wireless communication systems.

In this chapter, the interference from radar to wireless systems is constrained via mutual information (MI) based cognitive radar transmit waveform design, and the interference from wireless systems to radar is mitigated via adaptive beamforming at radar receiver side. Coherent MIMO radar structure is assumed, and the process is depicted in Figure 5.1. Unlike traditional phased-array radar, MIMO radar doesn't need to transmit at the maximum power at the expect target direction since a virtual target detection beam could be formed at the receiver side. Therefore, the transmit beam could be designed with nulls in the directions of base stations (BSs) within the radar detection range to constrain interference from radar to BSs without affecting radar's performance. Due to the orthogonality of the transmitted waveforms, waveform transmitted by each antenna element could be identified and extracted from the received echo signal, and then used to eliminate interference received at both radar antenna mainlobe and sidelobes from BSs via adaptive beamforming processing.

The remainder of the chapter is organized as following. The process of MI-based cognitive radar waveform design is detailed in Section 5.1. The interference mitigation processing method based on MIMO radar beamforming is presented in Section 5.2. The required interference mitigation for radar and wireless system to operate normally in the presence of each other is derived in Section 5.3. Simulations are carried out by assuming a general spectrum sharing scenario between S-band MIMO radar and wireless systems, and the simulation results are given in Section 5.4. A brief summary of the chapter is provided in Section 5.5.

5.1. Cognitive Radar Transmit Waveform Design

Since radar could acquire information about BSs within radar detection range beforehand by using the Radio Environmental Map (REM) and the Electronic Support Measurement (ESM) system [102], a defocused transmit beam with nulls in the directions of BSs could be formed, so that BSs will not be affected by radar system. The radar system model and the waveform design process are detailed as following.

A coherent MIMO radar with uniform linear transmit antenna array of N_T elements and uniform linear receive antenna array of N_R elements operating in monostatic mode is assumed in this section. The orthogonal phase-coded vector designed for transmit antenna element v (v = 1, 2, …, N_T) is expressed as

$$\mathbf{u}_v = [e^{j\phi_v^1}\ e^{j\phi_v^2} \cdots e^{j\phi_v^i} \cdots\ e^{j\phi_v^\Gamma}]^T \tag{5.1}$$

where Γ is the number of waveform sub-pulses in the time domain and ϕ_v^i is the coding phase of sub-pulse i ($1 \le i \le \Gamma$) of the waveform transmitted at antenna element v.

Therefore, the phase coded waveform transmitted at the *v*-th antenna element at time *t* is expressed as

$$s_v(t) = \begin{cases} \mathbf{u}_v(i) & (i-1)\tau \le t < i\tau \\ 0 & \text{Otherwise} \end{cases} \tag{5.2}$$

where $\mathbf{u}_v(i)$ is the *i*-th element of $\mathbf{u}_v$ and τ is the waveform sub-pulse duration. The $\Gamma \times N_T$ phase matrix of the space-time coding for N_T antenna elements is defined as

$$\mathbf{\Phi} = \begin{bmatrix} \phi_1^1 & \phi_2^1 & \cdots & \phi_{N_T}^1 \\ \phi_1^2 & \phi_2^2 & \cdots & \phi_{N_T}^2 \\ \vdots & \vdots & \ddots & \vdots \\ \phi_1^\Gamma & \phi_2^\Gamma & \cdots & \phi_{N_T}^\Gamma \end{bmatrix} \tag{5.3}$$

where the column vector $\boldsymbol{\phi}_v = [\phi_v^1 \ \ \phi_v^2 \cdots \phi_v^\Gamma]^T, v = 1, 2, \cdots, N_T$, is the phase coded sequence for Γ sub-pulse periods in the time domain for waveform $\mathbf{u}_v(i)$ transmitted from element *v*, and row vector $\boldsymbol{\varphi}_i = [\phi_1^i \ \ \phi_2^i \cdots \phi_{N_T}^i]$, $i = 1, 2, \cdots, \Gamma$, is the phase coded sequence for N_T elements in the space domain during the period of sub-pulse *i*.

5.1.1. Waveform design in space domain

In order to design the desired space-time waveform, to start with, the phases for the first subpulse, i.e. $\boldsymbol{\varphi}_1$, are designed to form a defocused transmit beam pattern with the deepest possible nulls in the directions of LTE BSs $(\theta_1^{BS}, \theta_2^{BS}, \cdots, \theta_P^{BS})$ and the strongest possible peaks in the nominal target directions $(\varphi_1^{NT}, \varphi_2^{NT}, \cdots \varphi_Q^{NT})$. Specifically, $\boldsymbol{\varphi}_1$ will be determined by carrying out the following optimization

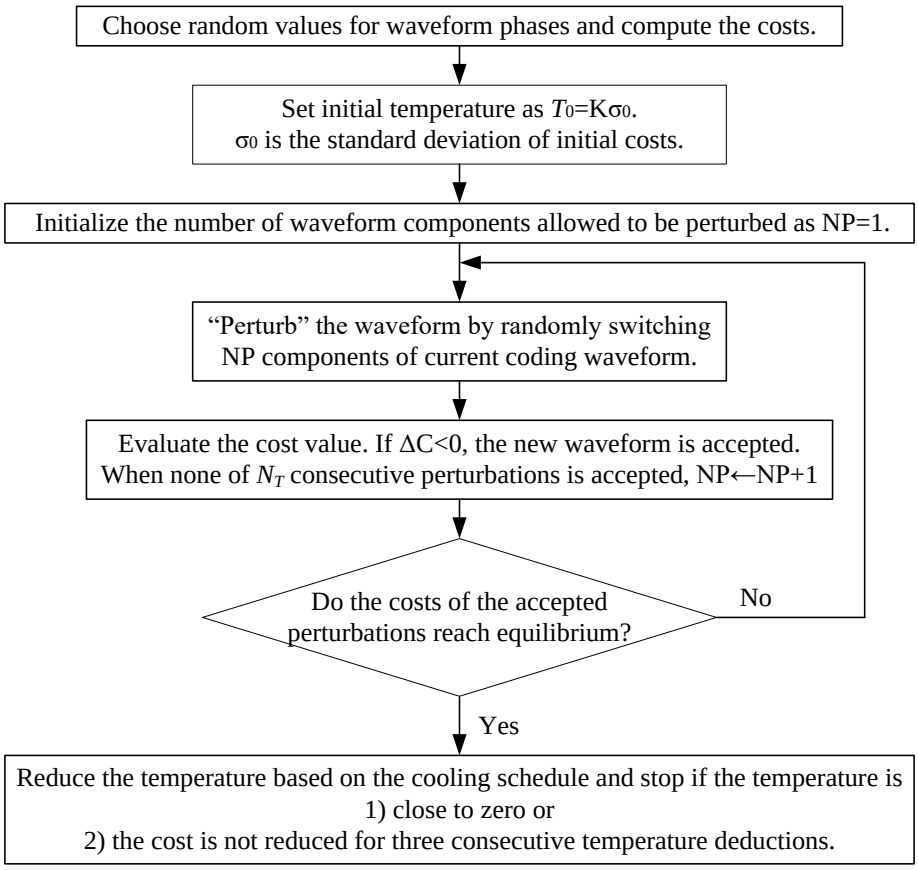

Figure 5.2 Flowchart of phase-coding waveform design in space domain using the Enhanced Simulated Annealing (ESA) algorithm.

$$\begin{cases} \boldsymbol{\varphi}_1 = \arg\min_{\boldsymbol{\varphi}_1} C(\boldsymbol{\varphi}_1) \\ C(\boldsymbol{\varphi}_1) = \mathbf{d}^H \mathbf{Q}\mathbf{d} - \mathbf{e}^H \mathbf{P}\mathbf{e} \end{cases} \tag{5.4}$$

where the vectors **d** and **e** denote the relative radiation intensities in the null $(\theta_1^{BS}, \theta_2^{BS}, \cdots, \theta_P^{BS})$ and in the peak $(\varphi_1^{NT}, \varphi_2^{NT}, \cdots \varphi_Q^{NT})$ directions, due to the waveform, respectively; **Q** and **P** are the diagonal matrices containing the real positive weight coefficients of the relative radiation intensities in the null and peak directions, respectively. Since the cost function in (5.4) is a non-linear function, the Enhanced Simulated Annealing (ESA) algorithm shown in Figure 5.2 is used to locate a good approximation to the global optimum [103].

5.1.2. Waveform design in time domain

After $\boldsymbol{\varphi}_1$ is determined, $\boldsymbol{\varphi}_{i+1}\,(i=1,2,...,\Gamma-1)$ will be derived iteratively from $\boldsymbol{\varphi}_i$. In the following, the process is demonstrated in by forming a defocused transmit beam with a null in the direction of the *p*-th BS, i.e. θ_p^{BS}. In order to ensure that the transmit beam is formed with a null in θ_p^{BS} throughout all waveform sub-pulse periods and the column vectors $\boldsymbol{\phi}_l$ and $\boldsymbol{\phi}_k$ are orthogonal for $l \neq k$, a random permutation of (1, 2, 3, …, N_T) is generated as $(I_1, I_2, \cdots, I_{N_T})$, and then apply the permutation to $\boldsymbol{\varphi}_i$ to generate a new phase sequence: $\{\phi_{I_1}^i, \phi_{I_2}^i, \cdots, \phi_{I_{N_T}}^i\}$. Hence the waveform phases $\{\phi_1^{i+1}, \phi_2^{i+1}, \cdots, \phi_{N_T}^{i+1}\}$ for the next row in the space-time phase matrix is:

$$\boldsymbol{\varphi}_i = \{\phi_{I_1}^i + 2\pi(1-I_1)d_0 \sin\theta_p^{BS}/\lambda,\ \cdots,\ \phi_{I_{N_T}}^i + 2\pi(N_{\mathrm{T}} - I_{N_T})d_0 \sin\theta_p^{BS}/\lambda\}. \tag{5.5}$$

It is easy to prove that the waveform thus generated has the same pattern shaping feature (i.e. a null in θ_p^{BS}) throughout all waveform sub-pulse periods since the transmit beam pattern generated from $\{\phi_1\ \phi_2 \cdots \phi_{N_T}\}$, which is expressed as,

$$\begin{aligned} V_1(\theta_p^{BS}) &= [e^{j\phi_1}\ \ e^{j\phi_2} \cdots e^{j\phi_{N_T}}]\left[1\ \ e^{-j2\pi d_0 \sin\theta_p^{BS}/\lambda} \cdots e^{-j2\pi(N_T-1)d_0 \sin\theta_p^{BS}/\lambda}\right]^T \\ &= \sum_{\nu=1}^{N_T} e^{j\left[\phi_\nu - 2\pi(\nu-1)d_0 \sin\theta_p^{BS}/\lambda\right]} \end{aligned} \tag{5.6}$$

is identical to the transmit beam generated from the waveform with coding phases in (5.5), which is given by

$$
\begin{aligned}
& V_2(\theta_p^{BS}) \\
&= \left[e^{j\left[\phi_{I_1} + 2\pi(1-I_1)d_0 \sin\theta_p^{BS}/\lambda\right]} \cdots e^{j\left[\phi_{I_{N_T}} + 2\pi(M-I_{N_T})d_0 \sin\theta_p^{BS}/\lambda\right]} \right] \left[1 \; e^{-j2\pi d_0 \sin\theta_p^{BS}/\lambda} \cdots e^{-j2\pi(N_T-1)d_0 \sin\theta_p^{BS}/\lambda} \right]^T . \quad (5.7) \\
&= \sum_{\nu=1}^{N_T} e^{j\left[\phi_{I_\nu} - 2\pi(I_\nu-1)d_0 \sin\theta_p^{BS}/\lambda\right]}
\end{aligned}
$$

The designed waveform also meets the orthogonality constraint for the following reason. Assume that ϕ_ν is randomly selected from one of the phases in $\{\phi_1 \; \phi_2 \cdots \phi_{N_T}\}$, which is uniformly distributed in [0, 2π), and I_ν is randomly selected from $\{1, 2, \cdots, N_T\}$. Due to the phase folding effect, the distribution of the phases in the phase sequence of $\{\phi_\nu + I_\nu 2\pi d_0 \sin\theta_p^{BS} / \lambda\}$ is the circular-convolution of two uniform distributions and hence, is still uniformly distributed in [0, 2π). Therefore, $\{e^{j(\varphi_\nu + I_\nu 2\pi d_0 \sin\theta_p^{BS}/\lambda)}\}$ is a complex pseudo-noise signal with its component phases uniformly and independently distributed. Furthermore, the autocorrelation of the sequence is a quasi-Dirac function and any two such sequences obtained similarly are quasi-orthogonal [103].

The transmit beam of MIMO radar doesn't have to transmit at the maximum power at the expect target direction since a virtual target detection beam could be formed at the receiver side. Therefore, the impact of MIMO radar on wireless systems is minimized even when the wireless systems are covered by radar mainlobe. In the extreme case where the BS is in the same direction with the target signal, a defocused transmit beam could be designed with a null in that direction to constrain the interference from radar to BS, and a virtual target detection beam with a peak in the expected target direction could be formed by refocusing the transmit-receive beam at radar receiver side via digital beamforming [103].

5.2. MIMO Radar Transmit-Receive Adaptive Beamforming

Since the waveform transmitted from each antenna element is designed to be orthogonal to each other, a coherent wave transmitted by an antenna element could be identified and extracted from the received echo signal through a matched filter correlated only to that waveform. After that, by applying a space-domain digital filter at the matched filter outputs, interference signals received at both antenna mainlobe and sidelobes from wireless systems would be canceled while target signals would be enhanced. The detailed process is as following.

The transmit steering vector $\mathbf{a}_T$ in the broadside direction of θ_T and receive steering vector $\mathbf{a}_R$ in the broadside direction of θ_R are, respectively,

$$\mathbf{a}_T(\theta_T) = \left[1 \; e^{-j2\pi\frac{d_0 \sin\theta_T}{\lambda}} \cdots e^{-j2\pi(N_T-1)\frac{d_0 \sin\theta_T}{\lambda}}\right]^T \tag{5.8}$$

$$\mathbf{a}(\theta_R) = \left[1 \; e^{-j2\pi\frac{d_0 \sin\theta_R}{\lambda}} \cdots e^{-j2\pi(N_R-1)\frac{d_0 \sin\theta_R}{\lambda}}\right]^T. \tag{5.9}$$

Taking into consideration of the initial transmit waveform coding, the transmit steering vector is modified as [104]

$$\mathbf{a}_m(\theta_T) = \mathbf{s}_{T0} \circ \mathbf{a}_T(\theta_T). \tag{5.10}$$

The ideal received target signal vector with unit amplitude is then expressed as

$$\mathbf{s}_r = \mathbf{v}_R(\theta_R) \otimes \mathbf{v}_m(\theta_T) \tag{5.11}$$

where $\otimes$ denotes the Kronecker product. Since collocated MIMO radar structure is assumed, in the following it is assumed that $\theta_T = \theta_R = \theta$ and the target is located at θ_0. Using the radar transmit waveform $\mathbf{s} = [\mathbf{s}_1, \mathbf{s}_2, \cdots, \mathbf{s}_M]$ designed according to (5.2), the

target signal vector $\boldsymbol{\chi}_t$ received at the receive array is

$$\boldsymbol{\chi}_t = \alpha[\mathbf{s}(t-\tau_t, f_D) \circ \mathbf{a}_T(\theta_0)] \otimes \mathbf{a}_R(\theta_0) \tag{5.12}$$

where α is the unknown complex amplitude of the target signal due to scattering and propagation losses, τ_t is the time delay, and f_D is the Doppler shift of the transmitted waveform **s**(*t*) caused by target scattering.

In the following, a case where *K* wireless interference source exist is considered. Assume that the η-th (η = 1, 2, …, *K*) wireless interference source is located at angle $\theta_{J\eta}$ and it is Gaussian distributed with variance $\sigma_{J\eta}^2$. The interference receive steering vector is given by

$$\mathbf{v}_J(\theta_{J\eta}) = [v_1 \quad v_2 \quad \cdots \quad v_{N_R}]^T = \left[1 \quad e^{-j2\pi\frac{d_0 \sin\theta_{J\eta}}{\lambda}} \quad \cdots \quad e^{-j2\pi\frac{(N_R-1)d_0 \sin\theta_{J\eta}}{\lambda}}\right]^T. \tag{5.13}$$

The received signals by N_R antenna elements due to the inference are expressed as

$$\mathbf{y} = [y_1 \quad y_2 \cdots y_{N_R}]^T = y(t)\mathbf{v}_J(\theta_{J\eta}). \tag{5.14}$$

And the $N_T \times N_R$ matched-filtered outputs are given by

$$\boldsymbol{\chi}_J = \left[\tilde{y}_{11} \quad \tilde{y}_{12} \quad \cdots \quad \tilde{y}_{1N_T} \quad \tilde{y}_{21} \quad \tilde{y}_{22} \quad \cdots \quad \tilde{y}_{2N_T} \quad \cdots \quad \tilde{y}_{N_R1} \quad \tilde{y}_{N_R2} \quad \cdots \quad \tilde{y}_{N_RN_T}\right]^T \tag{5.15}$$

where $\tilde{y}_{n\nu}$ is the matched-filtered outputs of the *n*-th antenna element matched to the waveform transmitted by the *v*-th antenna element. Here it is assumed that the interference signal time sequence out of antenna *n* to be $y_n(t)$, then $\tilde{y}_{n\nu}(t)$ is expressed as

$$\tilde{y}_{n\nu}(t) = \sum_{i=1}^{\Gamma} y_n(i+t-1)e^{-j\phi_i^{\nu}}. \tag{5.16}$$

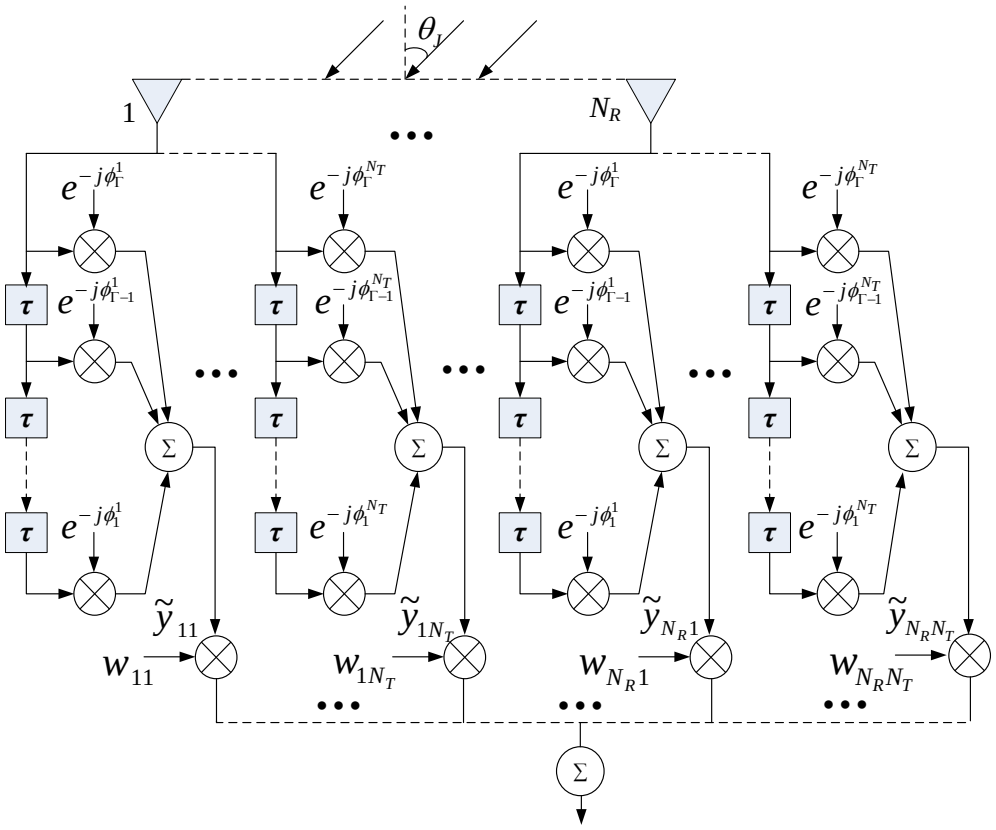

Figure 5.3 The interference-rejection receive beamforming for an interference signal.

The matched filtering processing of the η-th interference is shown in Figure 5.3.

The covariance matrix of the interference vector is given by [105]

$$\begin{aligned}\mathbf{R}_J(\theta_{J\eta},\sigma_{J\eta}^2) &= E\left[\boldsymbol{\chi}_J(\theta_{J\eta},\sigma_{J\eta}^2)\boldsymbol{\chi}_J^H(\theta_{J\eta},\sigma_{J\eta}^2)\right] \\ &= \begin{bmatrix} \mathbf{R}_{11}(\theta_{J\eta},\sigma_{J\eta}^2) & \mathbf{R}_{12}(\theta_{J\eta},\sigma_{J\eta}^2) & \cdots & \mathbf{R}_{1N_R}(\theta_{J\eta},\sigma_{J\eta}^2) \\ \mathbf{R}_{21}(\theta_{J\eta},\sigma_{J\eta}^2) & \mathbf{R}_{22}(\theta_{J\eta},\sigma_{J\eta}^2) & \cdots & \mathbf{R}_{2N_R}(\theta_{J\eta},\sigma_{J\eta}^2) \\ \vdots & \vdots & \mathbf{R}_{pq}(\theta_{J\eta},\sigma_{J\eta}^2) & \vdots \\ \mathbf{R}_{N_R1}(\theta_{J\eta},\sigma_{J\eta}^2) & \mathbf{R}_{N_R2}(\theta_{J\eta},\sigma_{J\eta}^2) & \cdots & \mathbf{R}_{N_RN_R}(\theta_{J\eta},\sigma_{J\eta}^2) \end{bmatrix}\end{aligned} \quad (5.17)$$

where $(\cdot)^H$ denotes Hermitian transpose. The $N_T \times N_T$ sub-matrix $\mathbf{R}_{pq}$ (p, q = 1, 2, …, N_T) in $\mathbf{R}_J(\theta_{J\eta},\sigma_{J\eta}^2)$ is given as

$$\mathbf{R}_{pq}(\theta_{J\eta},\sigma_{J\eta}^2)=\begin{bmatrix}\tilde{\sigma}_{J\eta}^2 v_p(\theta_{J\eta})v_q^*(\theta_{J\eta}) & 0 & \cdots & 0\\ 0 & \tilde{\sigma}_{J\eta}^2 v_p(\theta_{J\eta})v_q^*(\theta_{J\eta}) & \cdots & 0\\ \vdots & \vdots & \ddots & \vdots\\ 0 & 0 & \cdots & \tilde{\sigma}_{J\eta}^2 v_p(\theta_{J\eta})v_q^*(\theta_{J\eta})\end{bmatrix} \quad (5.18)$$

where $v_p(\theta_{J\eta})$ is the *p*-th component of $\mathbf{v}_J(\theta_{J\eta})$, and $\tilde{\sigma}_{J\eta}^2$ is given by

$$\tilde{\sigma}_{J\eta}^2=\Gamma\sigma_{J\eta}^2. \quad (5.19)$$

Assume that the *K* independent interfering sources are mutually independent, the covariance matrix of interference signals is given by

$$\mathbf{R}_{KJ}=\sum_{\eta=1}^{K}\mathbf{R}_J(\theta_{J\eta},\sigma_{J\eta}^2) \quad (5.20)$$

With the Generalized Likelihood Ratio Test (GLRT) algorithm applied, the optimal beamforming filter is obtained as [38]

$$\mathbf{w}=\hat{a}\left(\mathbf{R}_{KJ}+\sigma^2\mathbf{I}_{N_TN_R}\right)^{-1}\mathbf{s}_r \quad (5.21)$$

where σ^2 is the noise variance, $\mathbf{I}_{N_TN_R}$ is an $N_TN_R\times N_TN_R$ identity matrix, and $\mathbf{s}_r$ is the ideal received target signal vector with unit amplitude. The output of the adaptive beamforming filter is

$$z=\boldsymbol{\chi}_t^H\mathbf{w}+\boldsymbol{\chi}_J^H\mathbf{w}+\mathbf{n}^H\mathbf{w} \quad (5.22)$$

where $\boldsymbol{\chi}_t$, $\boldsymbol{\chi}_J$, and $\mathbf{n}$ are the target signal, interference and noise vectors at the output of the matched filters, respectively. To further analyze the interference mitigation results, two beamforming concepts for coherent MIMO radar are defined in the following.

***Definition* 1:** *Virtual antenna beam* (VAB) is defined as the output of the optimized MIMO radar filter with the two-way target signal as the input [105]. With the

optimal filter defined in this chapter, the normalized VAB pattern formed in the expected target direction is given by

$$V^{\dagger}(\theta) = \frac{1}{N_T N_R} \mathbf{s}_r^H \mathbf{w} . \tag{5.23}$$

***Definition* 2:** *Actual receive beam* (ARB) is defined as the output of the MIMO radar matched filter with the wireless interference signal as the input. The normalized ARB pattern is given by

$$R^{\dagger}(\theta) = \frac{1}{N_T N_R} \boldsymbol{\chi}_J^H \mathbf{w} . \tag{5.24}$$

Assume that the target is located at azimuth angle θ_0 and there are K wireless interferences affecting the radar receiver, the theoretical normalized VAB pattern is expressed as

$$V^{\dagger}(\theta) = \frac{1}{N_T N_R} \mathbf{s}_r^H(\theta) \mathbf{R}^{-1} \mathbf{s}_r(\theta_0) \tag{5.25}$$

, and the theoretical normalized ARB pattern is expressed as

$$\begin{aligned} R^{\dagger}(\theta) &= \frac{1}{N_T N_R} \sqrt{\mathbf{w}^H \boldsymbol{\chi}_J \boldsymbol{\chi}_J^H \mathbf{w}} \\ &= \frac{1}{N_T N_R} \sqrt{\mathbf{s}_r^H(\theta) \left(\mathbf{R}^{-1}\right)^H \left[\sum_{\eta=1}^{K} \tilde{\sigma}_{J\eta}^2 \mathbf{v}_J(\theta_{J\eta}) \mathbf{v}_J^H(\theta_{J\eta}) \right] \mathbf{R}^{-1} \mathbf{s}_r(\theta_0)} . \end{aligned} \tag{5.26}$$

According to Woodbury's identity, $\mathbf{R}^{-1}$ in (5.25) and (5.26) could be further expressed as

$$\begin{aligned} \mathbf{R}^{-1} &= \left[\sum_{\eta=1}^{K} \tilde{\sigma}_{J\eta}^2 \mathbf{v}_J(\theta_{J\eta}) \mathbf{v}_J^H(\theta_{J\eta}) + \sigma_n^2 \mathbf{I}_{N_R} \right]^{-1} \\ &= \mathbf{I}_{N_T N_R} - \sum_{\eta=1}^{K} \left[\frac{\tilde{\sigma}_{J\eta}^2}{\sigma_n^2 + N_R \tilde{\sigma}_{J\eta}^2} \mathbf{v}_J(\theta_{J\eta}) \mathbf{v}_J^H(\theta_{J\eta}) \otimes \mathbf{I}_{N_T} \right] . \end{aligned} \tag{5.27}$$

Since VAB and ARB of the phase-coded MIMO radar are statistically independent, the space signal processing algorithm proposed in this chapter allows the VAB to be maximized in the target direction, while ARB is minimized in the interference direction at the same time. Therefore, through the proposed algorithm, the interference signals received by radar from wireless systems can be eliminated effectively even in the case where they are illuminated by the antenna mainlobe [105].

5.3. Interference Mitigation Required for Radar and Wireless System to Coexist

In the following, the interference mitigation required for radar and wireless system to operate normally in the presence of each other is derived. Either radar or wireless system could be the interferer or the victim depending on who is currently transmitting. The power of the interfering signals arriving at the victim receiver on a decibel scale is

$$P_{RI} = P_I + G_I(\theta_I) + G_R(\theta_R) + L_{\text{feeder}} - L_p(D, f_s, h_I, h_R) \tag{5.28}$$

where P_I is the transmit power of the interferer, $G_I(\theta_I)$ is the antenna gain of the interferer, $G_R(\theta_R)$ is the antenna gain of the victim receiver, L_{feeder} is the feeder loss, and $L_p(D, f, h_I, h_R)$ is the total signal propagation path loss from the interferer to the victim receiver, respectively. The path loss is the function of the distance (D) between the interferer and the victim, the operating frequency (f_s), the height of the transmitting antenna of the interferer (h_I), and the height of the receiving antenna of the victim (h_R).

In this chapter, ITU-R Recommendation P.452 is employed when dealing with path loss between radar station and BS [106, 107]. Based on the distance between the

interferer and the victim, line-of-sight propagation model and trans-horizon propagation model are used accordingly. The test for the trans-horizon path condition is [107]

$$\theta_{\max} = \max_{i=1}^{s-1}(\theta_i) > \theta_{td} \tag{5.29}$$

where $\theta_{\max}$ is the maximum elevation angle seen by the interfering antenna, θ_{td} is the elevation angle subtended by the victim receiver antenna, and $\max_{i=1}^{s}(\cdot)$ denotes maximum of *s* numbers, and θ_i is elevation angle to the *i*-th terrain point calculated as

$$\theta_i = \frac{h_i - h_I}{d} - \frac{10^3 d_i}{2a_e} \tag{5.30}$$

$$\theta_{td} = \frac{h_R - h_I}{D} - \frac{10^3 D}{2a_e} \tag{5.31}$$

where h_i is the height of the *i*-th terrain point, d_i is the distance from interferer to the *i*-th terrain element, and a_e is the median effective Earth's radius. The trans-horizon path of wireless-radar signal propagation is depicted in Figure 5.4. For trans-horizon path, the path loss is given by

$$L_p(D, f_s, h_I, h_R) = -5 \log\left(10^{-0.2L_{bs}} + 10^{-0.2L_{bd}} + 10^{-0.2L_{ba}}\right) + A_h \tag{5.32}$$

where L_{bs}, L_{bd} and L_{ba} are the basic transmission loss due to tropospheric scatter, diffraction loss, and transmission loss due to anomalous propagation, respectively, and A_h is the losses due to height-gain effects in local clutter. For the line-of-sight propagation, the path loss is $L_p(D, f_s, h_I, h_R)$ is represented as

$$L_p(D, f_s, h_I, h_R) = 92.5 + 20 \log f_s + 20 \log D + E_s + L_{ds} + A_g + A_h \tag{5.33}$$

where A_g is the total gaseous absorption, E_s is the correction factor for multipath and focusing effects, and L_{ds} is the excess diffraction loss.

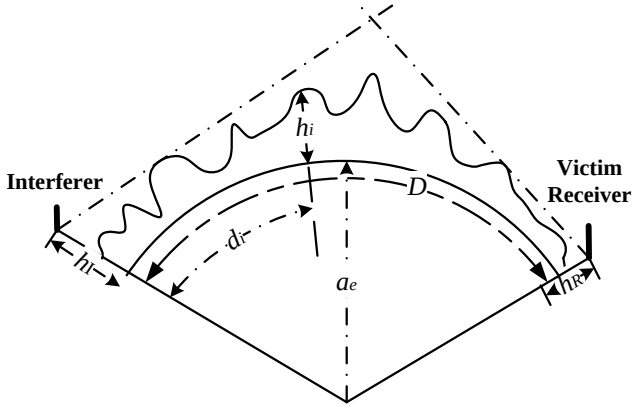

Figure 5.4 Trans-horizon signal propagation model.

Since the height of handset antenna in this chapter is assumed to be about 1.5m above the ground, the extended Hata model designed for mobile radio applications in non-LOS/cluttered environment is used for path loss analysis between radar and handset [108]. It is assumed that the probability of a handset is outdoor is equal to the probability that it is indoor. For propagation between radar and outdoor handset, the median path loss is given by

$$\begin{aligned} L_{outdoor} = {} & 46.3 + 33.9\log(2000) - (1.1\log(f_s) - 0.7)h_I - (1.56\log(f_s) - 0.8) \\ & - 20\log(h_R / 30) + 10\log(f_s / 2000) - 13.82\log(h_R) \\ & + \left[44.9 - 6.55\log(h_R)\right](\log(D)) \end{aligned} \quad . \qquad (5.34)$$

And the variation in path loss, $\sigma_{outdoor}$, is achieved by applying the log-normal distribution (slow fading). For propagation between radar and indoor handset, the median path loss is given by

$$L_{indoor} = L_{outdoor} + L_{wall} \qquad (5.35)$$

where L_{wall} is the attenuation due to external walls. The variation in path loss is given by

$$\sigma_{indoor} = \sqrt{\sigma_{outdoor}^2 + \sigma_{add}^2} \tag{5.36}$$

where σ_{add} is the increased standard deviation caused by the uncertainty on materials and relative location in the building.

For the victim receiver not to be affected by the interferer operating at the same frequency, the interference power must be less than the thermal noise floor of the victim receiver by a certain interference margin, i.e.

$$P_I \le P_{NF} - P_{\text{Margin}} \tag{5.37}$$

where P_{NF} is the receiver thermal noise floor of the victim receiver, and P_{Margin} is the interference margin. Thermal noise floor is defined as

$$P_{NF} = \kappa T_0 B \tag{5.38}$$

where κ is Boltzmann's constant, T_0 is the temperature in Kelvins, and B is the bandwidth of the victim receiver. If radar and wireless systems are physically close, the path loss in (5.28) is not large enough to satisfy the requirement in (5.37), additional mitigation is required for radar and wireless operate normally in the presence of each other, which is given by

$$P_{MITI} = P_I + P_{\text{Margin}} - kT_0 B\,. \tag{5.39}$$

The required additional mitigation in (5.39) could be achieved by using radar transmit waveform design in tandem with the adaptive beamforming processing method.

5.4. Simulation Results

In the simulation part, general spectrum sharing scenario is assumed, where BSs and handsets share the same frequency band with a coherent MIMO radar at operating at

2700 MHz. The radar antenna array consists of 16 half-wavelength spaced transmit/receive antenna elements, with each of them radiating in isotropic pattern. Sixteen orthogonal phase-coded transmitting waveforms with a coding length of 128 are employed by the radar. The radar antenna height is assumed to be 12 m.

5.4.1. Interference mitigation between radar and BSs

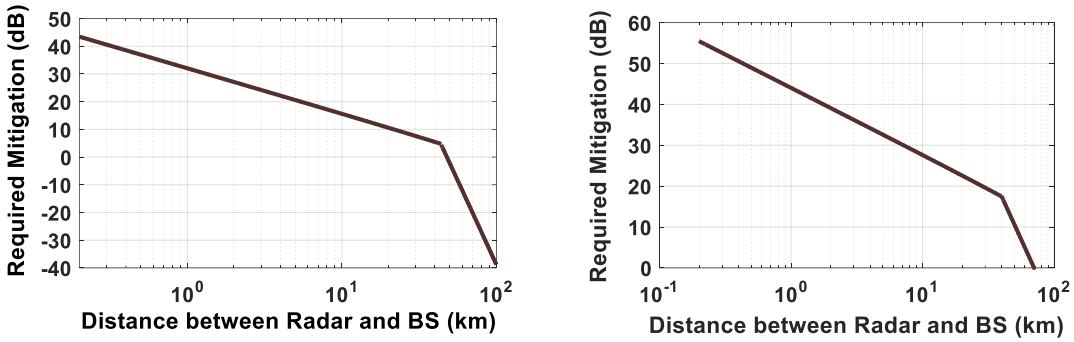

(a) (b)

Figure 5.5 The interference mitigations required for radar and BS.
(a) Mitigations required for radar to eliminate the interference from BS; (b) mitigations required for BS to eliminate interference from radar.

The BSs are assumed to use time division duplexing (TDD). The height of antennas of the BSs is assumed to be 45 meters, the maximum transmitter power of BSs is assumed to be 46 dBm, the antenna gain of BSs is assumed to be 18 dBi, and the feeder loss of BS is assumed to be 3 dB. The mitigations required for MIMO radar and BS to eliminate interferences from each other at various distances calculated according to (5.39) are plotted in Figure 5.5. It is shown in Figure 5.5 that due to path loss alone, the impact of BSs on radar could be ignored when they are more than 40 km away from each other, and the impact of radar on BSs could be ignored when they are more than 80 km away from each other. And when radar and BSs are close to each other 40-50 dB additional interference mitigation is required for the two systems to coexist in the same spectrum without affecting the performances of each other.

1) Constrain the interference from radar to BSs

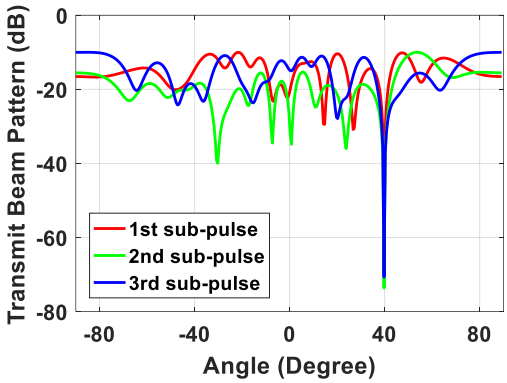

Figure 5.6 Defocused transmit beam pattern during the first three sub-pulses.

To start with, an extreme case where a BS is located in the same direction with the target at an azimuth angle of 40° is considered. The defocused transmit beam pattern during the first three sub-pulses is shown in Figure 5.6. The 1st sub-pulse is generated with ESA algorithm, and the other two sub-pulses are iteratively derived from the 1st sub-pulse. It could be seen that a null at 40° is formed throughout all three sub-pulse periods. Since the coding length is 128, a total number of 128 sub-pulses with null at 40° are generated.

Since the phase-coded waveforms transmitted from different antenna element are near-orthogonal in time domain, each transmit waveform could be identified and extracted from the received echo signal through a matched filter correlated only to that waveform, and then the transmit-receive beam could be refocused for optimal target detection via virtual beamforming. The transmit-receive beam pattern formed by using the designed phase-coded phases and the ideal refocused transmit-receive beam pattern formed by using ideal orthogonal waveforms are depicted in Figure 5.7, with the mainlobe of both beams pointing at 40°. It could be seen in Figure 5.7 that although the

designed coded waveforms are not perfectly orthogonal in time-domain, the performance of the actually formed transmit-receive beam at the radar receiver is very close to the ideal beamforming output.

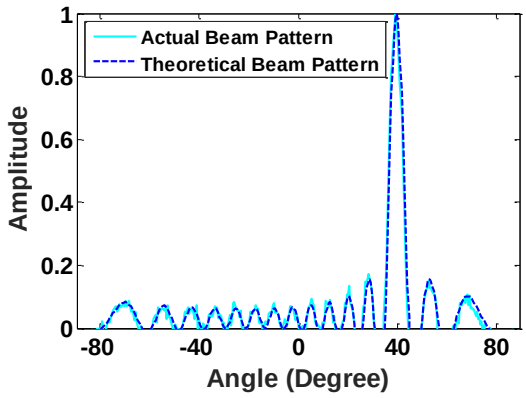

Figure 5.7 Refocused transmit-receive beam pattern with mainlobe pointing in 40°.

Since the radar transmit beam could form a virtual beam for target detection at the radar receiver instead of maximizing the transmit power in the expected target direction, the impact on BSs from radar is minimized. However, in the case where a large number of BSs located near radar system, the mitigation requirement has to be met by using Inter-Cell Interference Coordination (ICIC) techniques on the BSs' side. In current 4G LTE communication systems, ICIC allows neighboring BSs to coordinate their use of air-interface resources, which means BSs could use the resource towards the upper edge of the channel bandwidth, while its neighbor uses towards the lower edge of the channel bandwidth [109]. LTE ICIC options include interference cancellation (regenerate and subtract interfering signal from desired signal), opportunistic spectrum access (resources are assigned to sub-channels with low power spectral density) and organized beamforming (beams are pseudo-randomly hopped in quasi-orthogonal manner) [110].

2) Eliminate the interference from BSs to radar

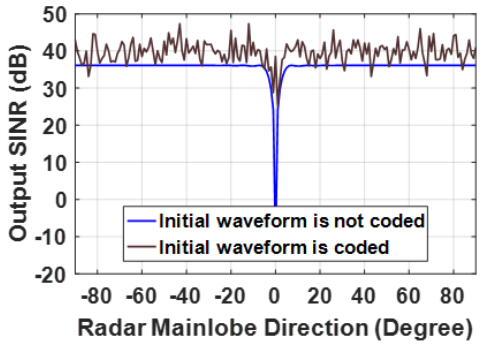

Figure 5.8 Output SINR in various mainbeam directions with the interference at 0°.

To begin with, the case where the wireless interference signal is in the same direction with the target signal is considered. Assume that the input interference-to-noise ratio (INR) is 64 dB and the signal-to-noise ratio (SNR) is 0 dB, the output SINR in various mainbeam directions with the interference at $\theta_J = 0°$ is shown in Figure 5.8. It could be seen that if the initial transmit waveform is not coded by random phases, the target signal is canceled together with the wireless interference signal if they are in the same direction, i.e. SINR = 0 dB when $\theta_0 = \theta_J = 0°$. However, if the initial transmit waveform is coded with random phases, the target signal is preserved while the interference signal is eliminated when $\theta_0 = \theta_J = 0°$.

In order to further demonstrate the performance of the proposed beamforming technique in eliminating the interference from a large number of BSs to radar, a more complicated scenario is assumed, where twenty-two BSs (marked as A-V) are covered by the mainlobe and sidelobes of a radar located at Miami International Airport, which is depicted in Figure 5.9. The location of the radar is set to be the origin of the Cartesian coordinate, with West/East direction as the *x*-axis, and North/South direction as the *y*-axis. The azimuth angle of each BS in degrees is calculated according to their location in the Cartesian coordinate. The locations of the BSs are summarized in Table 5.1, and it

could be seen that the interefrences received by radar from BSs are from 14 directions, i.e. $(\theta_{J1}, \theta_{J2}, \cdots, \theta_{J14})$ = (-78°, -70°, -29°, -21°, 2°, 9°, 16°, 32°, 37°, 42°, 45°, 51°, 64° and 68°). The target signal is expected in the broadside direction of $\theta_0 = 0^\circ$.

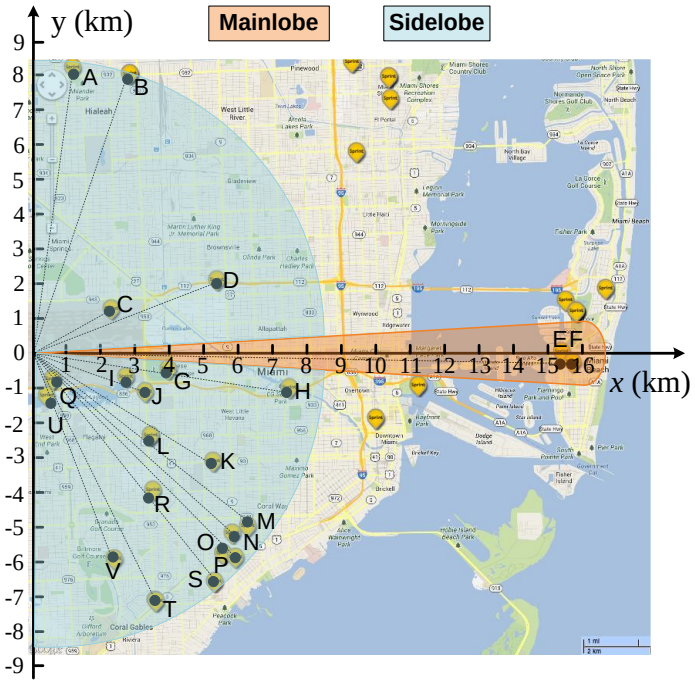

Figure 5.9 Base stations covered in radar mainlobe and sidelobes

Table 5.1 Base station locations

Base station	Location (x, y) Radar (0,0)	Azimuth angle (degrees)	Base station	Location (x, y) Radar (0,0)	Azimuth angle (degrees)
A	(1.7,8.0)	-78	L	(3.4,-2.6)	37
B	(2.8,7.8)	-70	M	(6.6,-4.9)	
C	(2.2,1.2)	-29	N	(5.8,-5.3)	42
D	(5.2,2.0)	-21	O	(5.6,-5.5)	45
E	(15.4,-0.42)	2	P	(6.0,-6.0)	
F	(15.7,-0.43)		Q	(0.71,-0.83)	
G	(3.9,-0.62)	9	R	(3.4, -4.2)	51
H	(7.4,-1.2)		S	(5.3,-6.6)	
I	(2.8,-0.80)	16	T	(3.5, -7.2)	64
J	(3.3,-0.95)		U	(0.61,-1.5)	68
K	(5.2,-3.2)	32	V	(2.4,-5.8)	

The VAB pattern for target detection with initial transmit waveform coding is plotted in Figure 5.10 (a). It could be seen that the interferences, which are marked as red

dash-dotted lines in the figure, do not affect the VAB patterns. The ARB pattern for interference mitigation is depicted in Figure 5.10 (b). In the ARB pattern, fourteen nulls can be seen formed in the exact directions of the BS to remove the interference signals in the radar output. Since through space processing the power of the interference signal is reduced more than -100 dB, according to Figure 5.5 (a) it is sufficient to eliminate the interferences from BS.

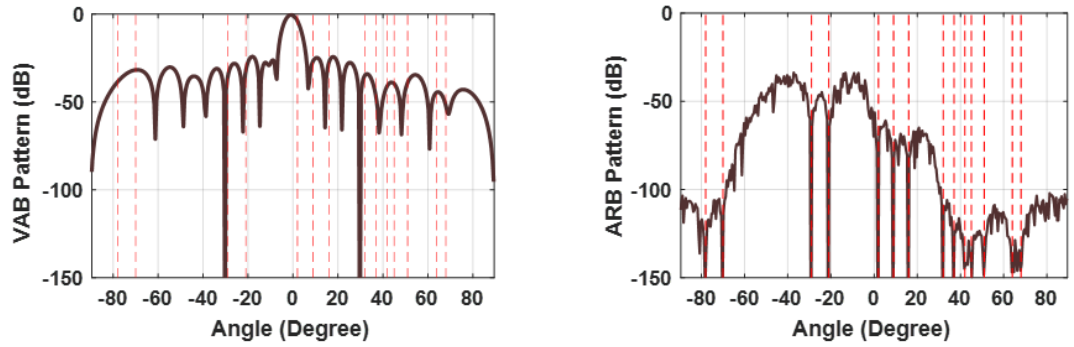

(a) (b)

Figure 5.10 MIMO radar beamforming output.
(a) virtual antenna beam (VAB) pattern for target detection; (b) actual receiving beam (ARB) pattern for interference mitigation (the red dash-dotted lines are the 14 directions of interferences)

5.4.2. Interference mitigation between radar and handsets

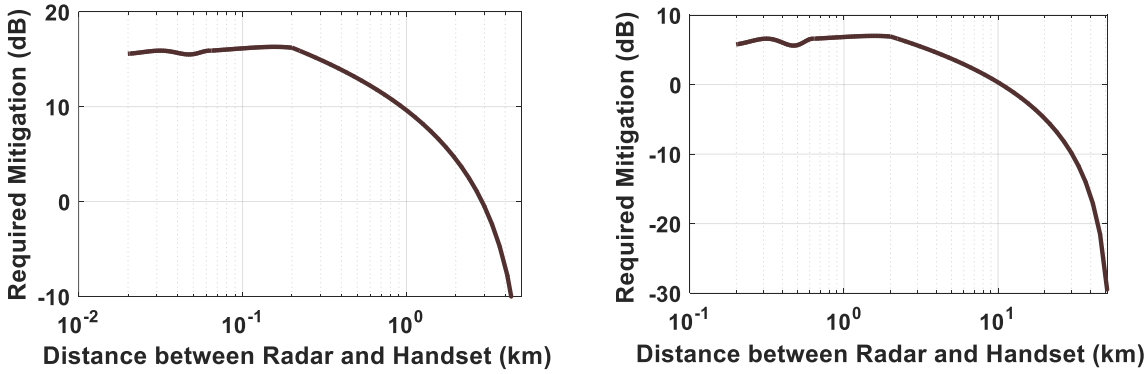

(a) (b)

Figure 5.11 Interference mitigations required for radar and handset.
(a) The mitigations required for radar to eliminate the interference from handset; (b) the mitigations required for handset to eliminate the interference MIMO radar.

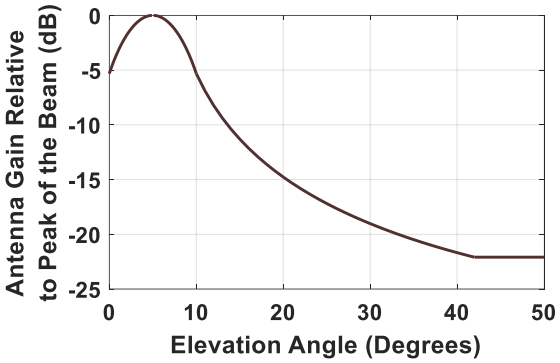

Figure 5.12 Antenna elevation pattern.

The maximum transmitter power, antenna gain and antenna height of the handsets are assumed to be 23 dBm, 0 dBi and 1.5 m, respectively. The number of simultaneously transmitting users per cell with maximum power is assumed to be one. The mitigation required for radar and handsets to eliminate the interferences from each other is plotted in Figure 5.11. It is shown in Figure 5.11 that due to path loss alone, the impact on radar from handsets located more than 3 km away could be ignored, and the impact on handsets from radar located more than 10 km away could be ignored. Meanwhile, since the antenna elevation pattern is assumed to be cosecant-squared pattern, which is plotted in Figure 5.12, the radar antenna gain is reduced for small elevation angles (i. e. when handset is near to radar).

For any other random directions in which the handsets may be located, the ARB pattern shows that there are at least 30 dB of mitigation, which is adequate to eliminate any possible interferences from handsets to radar system. The additional mitigation required for handset to operate normally in presence of radar could be obtained with ICIC techniques for heterogeneous macro-cellular networks proposed in 3GPP release 10 [111]. In a particular heterogeneous macro-cellular network, the transmit power of Macrocell BS and Pico BS are 20-60 W and 0.25 W, respectively, thus Pico UE (handset)

has to mitigate inference from Macro BS when it receives signals from Pico BS, which is similar to the scenario where the handset has to mitigate the interference from radar [112].

5.5. Summary of Chapter 5

In this chapter, an effective radar waveform design and beamforming approach is proposed for possible spectrum sharing between coherent MIMO radar and wireless communication systems. Specifically, MI based cognitive radar waveform design is used to constrain radar's impact on wireless systems by forming a defocused transmit waveform with nulls at the directions of BS. Meanwhile, virtual beamforming on the receiver side is used to eliminate interferences from BSs while preserving optimum target detection performance. Simulations are carried out by assuming a general spectrum sharing scenario where BS and handset share the same frequency band with a coherent MIMO radar operating at 2700 MHz. The simulation results indicate that with the radar transmit beam designed to minimize the impact on the wireless system, BS and handset could meet the additional interference mitigation requirements with existing 4G LTE ICIC techniques. At the same time, with the proposed radar beamforming approach, the MIMO radar can eliminate interferences received at both radar antenna mainlobe and sidelobes and operate normally during the radar-wireless spectrum sharing process.

6. CONCLUSIONS AND FUTURE RESEARCH

6.1. Conclusions

In this dissertation, innovative interference suppression techniques are proposed for phased-array radar and MIMO radar, and the performances of the proposed

approaches are compared with those of the existing widely used interference mitigation approaches. Two types of interferences are considered, ground clutter and jamming. It is demonstrated both analytically and empirically that the proposed interference mitigation methods are advantageous over the existing signal processing techniques in suppressing inhomogeneous ground clutter and jamming signal entering radar receiver through the antenna mainlobe. The interference mitigation approaches proposed in this dissertation are summarized in the following.

In Chapter 2, the image-feature based target-interference recognition approach termed as BDIFR is developed as an alternative approach to STAP to detect ground moving target in highly inhomogeneous clutter. The received radar echo data in space-time domain are transformed from the space-time domain to the beam-Doppler domain via 2D-DFT or MV method depending on the number of space-time snapshots available. An innovative MDB-RG algorithm is used to generate feature blocks from the denoised beam-Doppler image. And target recognition is carried out by comparing the size of each feature block to a predetermined threshold. Through various simulations, it is demonstrated that BDIFR is effective even when the target's velocity is low or clutter Doppler ambiguity is present.

In Chapter 3, a new approach to suppressing ground clutter and detecting moving target is proposed for airborne radar. The essence of the approach is to estimate the nonzero clutter Doppler frequency in each beam due to moving platform and then compensate for it in the beam-time domain through digital beamforming. After Doppler compensation, conventional MTI filter designed for ground-based radar is used for clutter suppression and target detection. This new ground target detection method allows

airborne radar to effectively detect ground moving targets in clutter without second-order statistic information of clutter.

In Chapter 4, two innovative ground clutter suppression approaches termed as RSTAP and R-D-STAP are proposed for airborne MIMO radar ground moving target detection in heterogeneous clutter. In RSTAP, the high dimensional weight vector is calculated iteratively with lower dimensional weight vectors, hence the computational complexity is reduced dramatically. In contrast, R-D-STAP operates on a snapshot-by-snapshot basis to determine the adaptive weights and can be readily implemented in real time.

In Chapter 5, an effective radar waveform design and beamforming approach is proposed for possible spectrum sharing between coherent MIMO radar and wireless communication systems. Specifically, MI based cognitive radar waveform design is used to constrain radar's impact on wireless systems by forming a defocused transmit waveform with nulls at the directions of BSs. Meanwhile, virtual beamforming on the receiver side is used to eliminate interferences from BSs while preserving optimum target detection performance.

Although several effective interference suppression approaches are proposed in this dissertation, the limitations of the research can't be ignored. First of all, clutter could be from many sources, which include land, sea, weather, birds, insects, etc., while only ground clutter is considered in this research. Moreover, the presence of various kinds of radar errors in realistic scenarios, which include errors in the receiving instrument and perturbations of the flight speed/path due to atmospheric turbulence, is not considered in this dissertation.

6.2. Future Research

During my doctoral studies, I became interested in spectrum sharing between radar and communication systems. In future research, I'd like to design a joint radar-communication (JRC) systems having both wireless communication and radar sensing abilities to alleviate the "spectrum crunch" problem for wireless communication while increasing radar coverage at low cost.

6.2.1. Embed communication data into radar transmit waveforms

To realize this goal, one possible research plan is to embed communication data into radar transmit waveforms by radar waveform design. Amplitude Modulation (AM) and Phase-Shift Keying (PSK) based dual-function radar communications (DFRC) systems have been proposed in [91] and [93], respectively, where multiple orthogonal transmit waveforms are used to embed the information to be transmitted. However, the data transmission rate of DFRC systems in [91] and [93] is relatively low. Therefore, new waveform design and information embedding strategies will be proposed in future research to improve the data transmission rate of the joint radar-communication system.

6.2.2. LTE-based multistatic passive radar

Another possible research plan is to use broadcast communication systems as the illuminators for multistatic passive radar. Among the potential candidates for passive radar applications, the mobile phones base-station transmitters are the most promising candidate due to the massive deployments of base stations. Using LTE eNodeBs as illuminators for passive radar has been considered in [113-115]. It is demonstrated in these works that using partial matched filters with deterministic features of LTE signal is

more cost-effective than using the LTE full downlink signal. Since the existing LTE downlink signal features are more suitable for communication data transmission than target positioning, a new LTE feature will be designed exclusively for passive radar application in future research. The relationship between the placement of eNodeBs/receivers and the estimation accuracy of target position and Doppler will be investigated. To improve the target localization accuracy, weighting matrices will be derived to compensate for the bistatic measurement errors due to interferences.

REFERENCES

1. M. A. Richards, *Principles of Modern Radar: Basic Principles*, Raleigh, NC: SciTech Publishing, 2010, pp. 18-25.

2. M. A. Richards, *Fundamentals of Radar Signal Processing*, New York City, NY: McGraw-Hill Education, 2014, pp. 5-17.

3. A. J. Fenn, D. H. Temme, W. P. Delaney and W. E. Courtney, "The development of phased-array radar technology," *Lincoln Laboratory Journal*, vol. 12, no. 2, pp. 321-340, Feb. 2000.

4. E. Fishler and et al., "Spatial diversity in radars – models and detection performance," *IEEE Trans. Signal Processing*, vol. 54, pp. 823-838, no. 3, Mar. 2006.

5. Y. Yang and R.S. Blum, "Minimax robust MIMO radar waveform design*," IEEE Journal of Selected Topics in Signal Processing*, vol. 1, pp. 147-155, no.1, 2007.

6. C. Y. Chen and P. P. Vaidyanathan, "MIMO radar waveform optimization with prior information of the extended target and clutter," *IEEE Trans. on Signal Processing*, vol. 57, pp. 3533-3544, no. 9, 2009.

7. I. Bekkerman and J. Tabrikian, "Target detection and localization using MIMO radars and sonars," *IEEE Trans. Signal Processing*, vol. 54, pp. 3873-3883, no. 10, Oct. 2006.

8. J. Li and P. Stoica, "MIMO radar with collocated antenna," *IEEE Signal Processing Magazine*, vol. 24, pp. 106-114, no. 5, Sept. 2007.

9. J. Li and P. Stoica (ed.), *MIMO Radar Signal Processing*, Hokoken, NJ: John Wiley & Sons, 2009.

10. D. J. Rabideau, "Non-adaptive multiple-input multiple-output radar for reducing clutter," *IET Radar, Sonar & Navigation*, vol. 3, pp. 304-313, no. 4, 2009.

11. T. Liu, Y. Zhang, J. Luan, Z. Liu and H. Ma, "A ground clutter computation procedure for airborne pulse Doppler radars," *2009 IET International Radar Conference*, Guilin, 2009, pp. 1-6.

12. T. Zhang, G. Cui, L. Kong and X. Yang, "Adaptive Bayesian detection using MIMO radar in spatially heterogeneous clutter," in *IEEE Signal Processing Letters*, vol. 20, no. 6, pp. 547-550, June 2013.

13. X. M. Li, D. Z. Feng, H. W. Liu, M. D. Xing and D. Luo, "Two-dimensional pulse-to-pulse canceller of ground clutter in airborne radar," in *IET Radar, Sonar & Navigation*, vol. 3, no. 2, pp. 133-143, April 2009.

14. G. P. Kefalas, “Radar noise jamming calculations simplified,” in *IEEE Transactions on Aerospace and Electronic Systems*, vol. 17, no. 2, pp. 297-300, March 1981.

15. S. Khadka, M. S. Anuradha, and C. Padmasree, “Study of the effect of barrage and deception jamming on a radar system along with their mitigation technique”, *International Journal of Science and Research (IJSR)*, vol. 4, no. 9, pp. 98-104.

16. X. Ma, J. Qin and J. Li, “Pattern recognition-based method for radar anti-deceptive jamming,” in *Journal of Systems Engineering and Electronics*, vol. 16, no. 4, pp. 802-805, Dec. 2005.

17. H. Dai, X. Wang and Y. Li, “Novel discrimination method of digital deceptive jamming in mono-pulse radar,” in *Journal of Systems Engineering and Electronics*, vol. 22, no. 6, pp. 910-916, Dec. 2011.

18. J. Zhang, N. Liu, L. Zhang, S. Zhao and Y. Zhao, “Active jamming suppression based on transmitting array designation for colocated multiple-input multiple-output radar,” in *IET Radar, Sonar & Navigation*, vol. 10, no. 3, pp. 500-505, 3 2016.

19. R. Klemm, *Principles of Space-time Adaptive Processing* (*IET Radar, Sonar, Navigation and Avionics Series*), London, UK: Institution for Engineering and Technology, 2006.

20. J. Guerci, *Space-time Adaptive Processing for Radar* (2nd Edition), Boston, MA: Artech House Radar Library, 2003.

21. L. E. Brennan and L. S. Reed, “Theory of adaptive radar,” in *IEEE Transactions on Aerospace and Electronic Systems*, vol. 9, no. 2, pp. 237-252, March 1973.

22. I. S. Reed, J. D. Mallett and L. E. Brennan, “Rapid convergence rate in adaptive arrays,” in *IEEE Transactions on Aerospace and Electronic Systems*, vol. 10, no. 6, pp. 853-863, Nov. 1974.

23. W. L. Melvin, G. A. Showman and R. K. Hersey, “Adaptive radar: beyond the RMB rule,” *2008 IEEE Radar Conference proceedings*, Rome, 2008, pp. 1-8.

24. R. Klemm, *Applications of Space-Time Adaptive Processing*. London: Institution of Electrical Engineers, 2004, pp. 305-374.

25. D. J. Rabideau and A. O. Steinhardt, “Improved adaptive clutter cancellation through data-adaptive training,” in *IEEE Transactions on Aerospace and Electronic Systems*, vol. 35, no. 3, pp. 879-891, Jul 1999.

26. J. S. Bergin, P. M. Techau, W. L. Melvin and J. R. Guerci, “GMTI STAP in target-rich environments: site-specific analysis,” *Radar Conference, 2002. Proceedings of the IEEE*, 2002, pp. 391-396.

27. J. R. Guerci, J. S. Goldstein and I. S. Reed, "Optimal and adaptive reduced-rank STAP," in *IEEE Transactions on Aerospace and Electronic Systems*, vol. 36, no. 2, pp. 647-663, Apr. 2000.

28. J. R. Guerci, "Theory and application of covariance matrix tapers for robust adaptive beamforming," in *IEEE Transactions on Signal Processing*, vol. 47, no. 4, pp. 977-985, Apr 1999.

29. J. R. Guerci and J. S. Bergin, "Principal components, covariance matrix tapers, and the subspace leakage problem," in *IEEE Transactions on Aerospace and Electronic Systems*, vol. 38, no. 1, pp. 152-162, Jan 2002.

30. G. A. Andrews, "Airborne radar motion compensation techniques, evaluation of TACCAR," Naval Research Laboratory (NRL) Report 7404, Apr. 1972.

31. R. M. Cooper, "The impact of TACCAR on STAP algorithm convergence," *Proceedings of 2005 IEEE International Radar Conference*, pp. 447-452, May. 2005.

32. Y. Kwag, M. Choi, C. Jung "An adaptive compensation of moving clutter Doppler shift for helicopter MTD Radar," *Proceedings of 2006 International Conference on Radar*, pp. 1-4, Oct. 2006.

33. R. S. Blum, W. L. Melvin, and M. C. Wicks, "An analysis of adaptive DPCA," *Proceedings of the 1996 IEEE National Radar Conference*, pp.303-308, May 1996.

34. T. J. Nohara "Comparison of DPCA and STAP for space-based radar," *Record of the IEEE 1995 International Radar Conference*, pp.113-119, May 1995.

35. T. K. Sarkar, H.Wang, S. Park, R. Adve, J. Koh, K. Kim, Y. Zhang, M. C. Wicks, and R. D. Brown, "A deterministic least-squares approach to space-time adaptive processing (STAP)," *IEEE Trans. Antennas Propag.*, vol. 49, no. 1, pp. 91–103, Jan. 2001.

36. A. De Maio, A. Farina and F. Gini, "Performance analysis of the sidelobe blanking system for two fluctuating jammer models," in *IEEE Transactions on Aerospace and Electronic Systems*, vol. 41, no. 3, pp. 1082-1091, July 2005.

37. R. Nitzberg, *Adaptive Signal Processing for Radar*, Norwood, MA: Artech House, Inc., 1992.

38. M. H. Hayes, *Statistical Digital Signal Processing and Modeling*, New York: John Wiley & Sons, 1996.

39. W. L. Melvin, "Space-time adaptive radar performance in heterogeneous clutter," in *IEEE Transactions on Aerospace and Electronic Systems*, vol. 36, no. 2, pp. 621-633, Apr 2000.

40. R. Klemm, “Adaptive airborne radar: An auxiliary channel approach,” *IEE Proceedings*, vol. 134, Pt. *F*, No. 3, pp. 269-276, June. 1987.

41. R. Klemm, “Adaptive clutter suppression for airborne phased array radars. *IEE Proceedings*, Pt. *F* and *H*, no. 1, pp. 125-132, Feb. 1983.

42. B. R. Mahafza, *Introduction to Radar Analysis*, Boca Raton, FL: CRC Press, 1998, pp. 215-235.

43. J. R. Beveridge, J. Griffith, R.R. Kohler, A.R. Hanson, E. M. Riseman, “Segmenting images using localized histograms and region merging”, *International Journal of Computer Vision* 2 (3), pp. 311-347, 1989.

44. R. Adams and L. Bischof, “Seeded region growing,” *IEEE Transactions on Pattern Analysis and Machine Intelligence*, vol. 16, no. 6, pp. 641- 647, June 1994.

45. S. C. Zhu and A. Yuille, “Region competition: Unifying snakes, region growing, and Bayes/MDL for multiband image segmentation,” *IEEE Transactions on Pattern Analysis and Machine Intelligence*, vol. 18, no. 9, 884 - 900, Sep. 1996.

46. S. A. Hojjatoleslami and J. Kittler, “Region growing: A new approach,” *IEEE Transactions on Image Processing*, vol. 7, pp. 1079- 1084, July 1998.

47. J. Fan, D. K. Y. Yau, A. K. Elmagarmid, W. G. Aref, “Automatic image segmentation by integrating color-edge extraction and seeded region growing,” *IEEE Transactions on Image Processing*, vol. 10, no. 10, pp. 1454 - 1466, Oct. 2001.

48. S-Y. Wan and W. E. Higgins, “Symmetric region growing,” *IEEE Transactions on Image Processing*, Vol. 12, No. 9, pp. 1007-1015, Sep. 2003.

49. S. M. Kay, *Fundamentals of Statistical Signal Processing Volume II Detection Theory*, pp. 20-24, Upper Saddle River, New Jersey: Prentice Hall, 1998.

50. K. Fukunaga, *Statistical Pattern Recognition* (2nd Edition), pp. 63-65, San Diego, California: Academic Press, 1990.

51. B. R. Mahafza, *Radar Systems Analysis and Design Using MATLAB* (2nd Edition), London: Chapman and Hall/CRC, 2005.

52. W. L. Stutzman and G. A. Thiele, *Antenna Theory and Design*, 2nd ed., New York: John Wiley & Sons, 1998.

53. M. I. Skolnik, *Introduction to Radar Systems*, 3rd Ed., New York: McGraw-Hill, 2001.

54. A. Zverev, “Digital MTI radar filters,” in *IEEE Transactions on Audio and Electroacoustics*, vol. 16, no. 3, pp. 422-432, Sep. 1968.

55. A. Ludloff and M. Minker, “Reliability of velocity measurement by MTD radar,” *IEEE Trans. Aerospace and Electronics Systems*, vol. 21, no. 4, pp. 522–528, July 1985.

56. Y. K. Kwag, “An airborne radar system with adaptive MTD Doppler compensation scheme using DSP based real-time spectral estimation,” *2008 IEEE Radar Conference*, Rome, 2008, pp. 1-5.

57. M. I. Skolnik, *Radar Handbook*, 3rd Ed., New York: McGraw Hill. 2008.

58. L. Brennan, J. Mallett and I. Reed, “Adaptive arrays in airborne MTI radar,” *IEEE Transactions on Antennas and Propagation*, vol.24, no.5, pp. 607- 615, Sep 1976.

59. “IEEE standard radar definitions,” *IEEE Std. 686-2008 (Revision of IEEE Std. 686-1997)*, pp. 1-41, May 2008.

60. J. Ward, *Space-Time Adaptive Processing for Airborne Radar*, MIT Lincoln Laboratory Technical Report 1015, ESC-TR-94-109, 1994.

61. C. Y. Chen and P. P. Vaidyanathan, “MIMO radar space–time adaptive processing using prolate spheroidal wave functions,” in *IEEE Transactions on Signal Processing*, vol. 56, no. 2, pp. 623-635, Feb. 2008.

62. G. Wang and Y. Lu, “Clutter rank of STAP in MIMO Radar with waveform diversity,” in *IEEE Transactions on Signal Processing*, vol. 58, no. 2, pp. 938-943, Feb. 2010.

63. H. Jie, D. Feng and L. Ma, “Reduced-dimension clutter suppression method for airborne multiple-input multiple-output radar based on three iterations,” in *IET Radar, Sonar & Navigation*, vol. 9, no. 3, pp. 249-254, 2015.

64. W. Zhang, Z. He, J. Li and C. Li, “Beamspace reduced-dimension space–time adaptive processing for multiple-input multiple-output radar based on maximum cross-correlation energy,” in *IET Radar, Sonar & Navigation*, vol. 9, no. 7, pp. 772-777, 2015.

65. B. Tang and J. Tang, “Joint design of transmit waveforms and receive filters for MIMO radar space-time adaptive processing,” in *IEEE Transactions on Signal Processing*, vol. 64, no. 18, pp. 4707-4722, Sept.15, 2016.

66. W. Wang, Z. Chen, X. Li and B. Wang, "Space time adaptive processing algorithm for multiple-input–multiple-output radar based on Nyström method," in *IET Radar, Sonar & Navigation*, vol. 10, no. 3, pp. 459-467, 2016.

67. W. Liu, Y. Wang, J. Liu, W. Xie, H. Chen, and W. Gu, "Adaptive detection without training data in colocated MIMO radar", *IEEE Transactions on Aerospace and Electronic Systems*, vol. 51, no. 3, pp. 2469-2479, July 2015.

68. B. Jiu, H. Liu, X. Wang, L. Zhang, Y. Wang, and B. Chen, "Knowledge-based spatial-temporal hierarchical MIMO radar waveform design method for target detection in heterogeneous clutter zone," in *IEEE Transactions on Signal Processing*, vol. 63, no. 3, pp. 543-554, Feb. 2015.

69. Q. He, N. H. Lehmann, R. S. Blum, R. S., and A. M. Haimovich, "MIMO radar moving target detection in homogeneous clutter," *IEEE Transactions on Aerospace and Electronic Systems*, vol. 46, no. 3, pp. 1290–1301, Mar. 2010.

70. C. Y. Chong, F. Pascal, J. P. Ovarlez and M. Lesturgie, "MIMO Radar Detection in Non-Gaussian and Heterogeneous Clutter," in *IEEE Journal of Selected Topics in Signal Processing*, vol. 4, no. 1, pp. 115-126, Feb. 2010.

71. H. Deng, "Polyphase code design for Orthogonal Netted Radar systems," in *Signal Processing, IEEE Transactions on*, vol.52, no.11, pp.3126-3135, Nov. 2004.

72. R. Nitzberg, "An effect of range-heterogeneous clutter on adaptive Doppler filters," in *IEEE Transactions on Aerospace and Electronic Systems*, vol. 26, no. 3, pp. 475-480, May 1990.

73. W. L. Melvin, "Space-time adaptive radar performance in heterogeneous clutter," in *IEEE Transactions on Aerospace and Electronic Systems*, vol. 36, no. 2, pp. 621-633, Apr. 2000.

74. M. Grant and S. Boyd, *CVX: Matlab Software for Disciplined Convex Programming 2015* [Online]. Available: http://cvxr.com/cvx.

75. M. Ahmadi and K. Mohamed-pour, "Space-time adaptive processing for phased-multiple-input–multiple-output radar in the non-homogeneous clutter environment," in *IET Radar, Sonar & Navigation*, vol. 8, no. 6, pp. 585-596, July 2014.

76. U.S. Department of Commerce, "Federal radar spectrum requirements", May, 2000.

77. M. A. McHenry, "NSF spectrum occupancy measurements project summary", *Shared Spectrum Company Report*, Aug. 2005.

78. U. S. Department of Defense, "Electromagnetic spectrum strategy: a call to action", Sep. 2013.

79. J. B. Evans, "Shared spectrum access for radar and communications (SSPARC)", www.darpa.mil/program/shared-spectrum-access-for-radar-and-communications. Accessed 13 Sep. 2016.

80. B. Donnet and I. Longstaff, “Combining MIMO radar with OFDM communications,” in *2006 European Radar Conference*, 2006.

81. C. Sturm, T. Zwick and W. Wiesbeck, “An OFDM system concept for joint radar and communications operations,” in *2009 Vehicular Technology Conference*, 2009.

82. Y. L. Sit, C. Sturm, J. Baier, and T. Zwick, “Direction of arrival estimation using the MUSIC algorithm for a MIMO OFDM radar,” in *Radar Conference (RADAR), 2012 IEEE*, pp.0226-0229, 7-11 May 2012.

83. Y. L. Sit and T. Zwick, “MIMO OFDM radar networks: Inter- & intra-system interference handling,” in *Microwave Conference (APMC), 2014 Asia-Pacific*, pp.1318-1320, 4-7 Nov. 2014.

84. Y. L. Sit and T. Zwick, “MIMO OFDM radar with communication and interference cancellation features,” in *Radar Conference, 2014 IEEE*, pp.0265-0268, 19-23 May 2014.

85. T. Guo and R. Qiu, “OFDM waveform design compromising spectral nulling, side-lobe suppression and range resolution,” in *Radar Conference (RADAR), 2014 IEEE*, 2014.

86. X. Xia, T. Zhang, and L. Kong, “MIMO OFDM radar IRCI free range reconstruction with sufficient cyclic prefix,” in *Aerospace and Electronic Systems, IEEE Transactions on* , vol.51, no.3, pp.2276-2293, July 2015.

87. Z. Lin and Z. Wang, “Interleaved OFDM signals for MIMO radar,” in *Sensors Journal, IEEE* , vol.15, no.11, pp.6294-6305, Nov. 2015.

88. J. Euzière, R. Guinvarc'h, M. Lesturgie, B. Uguen and R. Gillard, "Dual function radar communication time-modulated array," *2014 International Radar Conference*, Lille, 2014, pp. 1-4.

89. J. Euzière, R. Guinvar'h, I. Hinostroza, B. Uguen and R. Gillard, "Time modulated array for dual function radar and communication," *2015 IEEE International Symposium on Antennas and Propagation & USNC/URSI National Radio Science Meeting*, Vancouver, BC, 2015, pp. 806-807.

90. A. Hassanien, M. G. Amin, Y. D. Zhang and F. Ahmad, "A dual function radar-communications system using sidelobe control and waveform diversity," *2015 IEEE Radar Conference (RadarCon)*, Arlington, VA, 2015, pp. 1260-1263.

91. A. Hassanien, M. G. Amin, Y. D. Zhang and F. Ahmad, "Dual-function radar-communications: information embedding using sidelobe control and waveform diversity," in *IEEE Transactions on Signal Processing*, vol. 64, no. 8, pp. 2168-2181, April 2016.

92. A. Hassanien, M. G. Amin, Y. D. Zhang and F. Ahmad, "Dual-function radar-communications using phase-rotational invariance," *2015 23rd European Signal Processing Conference (EUSIPCO)*, 2015, pp. 1346-1350.

93. A. Hassanien, M. G. Amin, Y. D. Zhang, F. Ahmad and B. Himed, "Non-coherent PSK-based dual-function radar-communication systems," *2016 IEEE Radar Conference (RadarCon)*, 2016.

94. A. Hassanien, M. G. Amin, Y. D. Zhang and F. Ahmad, "Signaling strategies for dual-function radar communications: an overview," *IEEE A&E Systems Magazine*, pp. 36-45, Oct. 2016.

95. A. Khawar, A. Abdel-Hadi and T. C. Clancy, "Spectrum sharing between S-band radar and LTE cellular system: a spatial approach," in *Proc. IEEE International Symposium on Dynamic Spectrum Access Networks*, 2014, pp. 7-14.

96. C. Shahriar, A. Abdelhadi and T. C. Clancy, "Overlapped-MIMO radar waveform design for coexistence with communication systems," *Proc. IEEE Wireless Communications and Networking Conference (WCNC)*, New Orleans, LA, 2015, pp. 223-228.

97. S. Sodagari, A. Khawar, T. C. Clancy and R. McGwier, "A projection based approach for radar and telecommunication systems coexistence," in *Proc. IEEE Global Communications Conference (GLOBECOM)*, 2012, pp. 5010-5014.

98. A. Khawar, A. Abdel-Hadi and T. C. Clancy, "Resource allocation with carrier aggregation in LTE advanced cellular system sharing spectrum with S-band radar," in *Proc. IEEE International Symposium on Dynamic Spectrum Access Networks (DYSPAN)*, 2014, pp. 34-37.

99. M. Piezzo, A. D. Maio, A. Aubry and A. Farina, "Cognitive radar waveform design for spectral coexistence," in *Proc. 2013 IEEE Radar Conference*, 2013, pp. 1-4.

100. A. Aubry, A. D. Maio, M. Piezzo, M. M. Naghsh, M. Soltanalian and P. Stoica, "Cognitive radar waveform design for spectral coexistence in signal-dependent interference," in *Proc. IEEE Radar Conference*, 2014, 474-478.

101. S. Kim, J. M. J. Park and K. Bian, "PSUN: An OFDM scheme for coexistence with pulsed radar," *2015 International Conference on Computing, Networking and Communications (ICNC)*, Garden Grove, CA, 2015, pp. 984-988.

102. A. Aubry, A. De Maio, M. Piezzo and A. Farina, "Radar waveform design in a spectrally crowded environment via nonconvex quadratic optimization," in *IEEE Transactions on Aerospace and Electronic Systems*, vol. 50, no. 2, pp. 1138-1152, April 2014.

103. H. Deng, Z. Geng and B. Himed, "MIMO radar waveform design for transmit beamforming and orthogonality," in *IEEE Transactions on Aerospace and Electronic Systems*, vol. 52, no. 3, pp. 1421-1433, June 2016.

104. Z. Geng, H. Deng and B. Himed, "Adaptive radar beamforming for interference mitigation in radar-wireless spectrum sharing," in *IEEE Signal Processing Letters*, vol. 22, no. 4, pp. 484-488, April 2015.

105. H. Deng and B. Himed, "Interference mitigation processing for spectrum-sharing between radar and wireless communications systems," in *IEEE Transactions on Aerospace and Electronic Systems*, vol. 49, no. 3, pp. 1911-1919, July 2013.

106. Electronic Communications Committee (ECC) Report 174, Mar. 2012.

107. *ITU-R Recommendation*, P.452-11, April 2003.

108. K. Koch, "Appropriate propagation models to be used for the assessment of the impact of high gain antennas". *European Conference of Postal and Telecommunications Administrations (CEPT)*. Jun. 2011.

109. C. Johnson, *Long Term Evolution IN BULLETS*, 2nd Edition, July. 2012.

110. G. Boudreau, J. Panicker, N. Guo, R. Chang, N. Wang, and S. Vrzic, "Interference coordination and cancellation for 4G networks", *IEEE Communications Magazine*, April 2009.

111. S. Sesia (Editor), I. Toufik (Editor) and M. Baker (Editor), *LTE, The UMTS Long Term Evolution: From Theory to Practice*, Wiley, 2nd Edition, Sept. 2011.

112. K. I. Pedersen, Y. Wang, S. Strzyz and F. Frederiksen, "Enhanced intercell interference coordination challenges in heterogeneous networks", *IEEE Wireless Communications*, vol. 18, no. 3, June 2013.

113. A. Evers, "Evaluation and application of LTE, DVB, and DAB signals of opportunity for passive bistatic SAR imaging", M.S. thesis, Wright State University, Dayton, OH, May 2014.

114. A. Evers and J. A. Jackson, "Analysis of an LTE waveform for radar applications," *2014 IEEE Radar Conference*, Cincinnati, OH, 2014, pp. 0200-0205.

115. A. Evers and J. A. Jackson, "Cross-ambiguity characterization of communication waveform features for passive radar," *IEEE Trans. on Aerospace and Electronic Systems*, vol. 51, no. 4, pp. 3440-3455, Oct. 2015.

VITA

ZHE GENG

Born, Shijiazhuang, Hebei, China

2008-2010	B.S. in Electrical Engineering (2+2 Dual Degree Program) Hebei University of Technology Tianjin, China
2010-2012	B.S. in Electrical Engineering (Magna Cum Laude) Florida International University Miami, Florida
2012-2018	Doctoral Student, Electrical Engineering Presidential Fellowship Florida International University Miami, Florida

PUBLICATIONS AND PRESENTATIONS

[1] Z. Geng, H. Deng, and B. Himed, "Fusion of radar sensing and wireless communications by embedding communication signals into the radar transmit waveform", *IET Radar, Sonar & Navigation*. Published on *IET Digital Library* as *E-First* on 12 Mar. 2018.

[2] Z. Geng, H. Deng, and B. Himed, "Ground moving target detection using beam-Doppler image feature recognition", *IEEE Transactions on Aerospace and Electronic Systems*. Published on *IEEE Xplore* as *Early Access* on 10 Mar. 2018.

[3] Z. Geng, S.M. Amin Motahari, H. Deng and B. Himed, "Ground moving target detection for airborne radar using clutter Doppler compensation and digital beamforming", *Microwave and Optical Technology Letters*, vol. 60, no. 1, pp. 101-110, Jan. 2018.

[4] R. Xu, L. Wang, Z. Geng, H. Deng, L. Peng and L. Zhang, "A unitary precoder for optimizing spectrum and PAPR characteristic of OFDMA signal", accepted for inclusion in a future issue of *IEEE Transactions on Broadcasting*. Published on *IEEE Xplore* as *Early Access* on 9 Aug. 2017.

[5] H. Deng, Z. Geng, B. Himed, "MIMO radar waveform design for transmit beamforming and orthogonality", *IEEE Transactions on Aerospace and Electronic Systems*, vol. 52, no. 3, pp. 1421-1433, June 2016.

[6] Z. Geng, H. Deng and B. Himed, “Adaptive radar beamforming for interference mitigation in radar-wireless spectrum sharing”, *IEEE Signal Processing Letters*, vol. 22, no. 4, pp. 484-488, April 2015.

[7] L. Guo, H. Deng, B. Himed, T. Ma and Z. Geng, "Waveform optimization for transmit beamforming with MIMO radar antenna arrays," in *IEEE Transactions on Antennas and Propagation*, vol. 63, no. 2, pp. 543-552, Feb. 2015.

[8] H. Deng, Z. Geng and B. Himed, “Radiation beam pattern synthesis for coherent MIMO radar antenna arrays”, *Microwave and Optical Technology Letters*, vol. 56, no. 11, pp. 2740–2745, Nov. 2014.

[9] Z. Geng, H. Deng and B. Himed, "Embedding communication signals into the radar transmit waveform”, *2017 International Conference on Radar Systems*, Oct. 2017.

[10] Z. Geng, H. Deng and B. Himed, "Interference mitigation for airborne MIMO radar”, *2017 International Conference on Radar Systems*, Oct. 2017.

[11] Z. Geng, H. Deng and B. Himed, "Radar clutter suppression with Beam-Doppler Image Feature Recognition (BDIFR) method", *2017 IEEE Radar Conference*, pp. 1109-1114, May 2017.

[12] Z. Geng, H. Deng and B. Himed, "Waveform design for coherent MIMO radar radiation management and transmit-receive beam refocusing", *2016 IEEE Radar Conference (RadarConf)*, pp. 1-5, May 2016.

[13] Z. Geng and H. Deng, "Beam-Doppler Image Feature Recognition (BDIFR) method for radar clutter management and target detection", *2016 IEEE APSURSI*, pp. 2053-2054, July 2016.

[14] Z. Geng and H. Deng, "Adaptive interference and clutter rejection processing for bistatic MIMO radar", *2016 IEEE APSURSI*, pp. 2055-2056, July 2016.

[15] Z. Geng and H. Deng, "Antenna beamforming for interference cancellation in radar-wireless spectrum sharing", *2015 IEEE APSURSI*, pp.133-134, July 2015.

[16] Z. Geng and H. Deng, “Transmit/receive beamforming for bistatic multiple-input multiple-output (MIMO) radar”, *2014 IEEE APSURSI*, pp. 147-148, 2014.

[17] Z. Geng and H. Deng, “Wireless signal propagation path loss estimation”, *2014 IEEE APSURSI*, pp. 953-954, 2014.

[18] Z. Geng and H. Deng, “Performance evaluation of image feature-based space-time processing (IFSTP) for moving target detection”, *2013 IEEE APSURSI*, pp. 1024-1025, 2013.